Summer 8-15-2018

Spin Alignment Generated in Inelastic Nuclear Reactions

Daniel Hoff
Washington University in St. Louis

WASHINGTON UNIVERSITY IN ST. LOUIS

Department of Chemistry

Dissertation Examination Committee:
Lee Sobotka, Chair
Robert Charity
Willem Dickhoff
Richard Mabbs
Demetrios Sarantites

Spin Alignment Generated in Inelastic Nuclear Reactions

by
Daniel Edward Macan Hoff

A dissertation presented to
The Graduate School
of Washington University in
partial fulfillment of the
requirements for the degree
of Doctor of Philosophy

August, 2018

Saint Louis, Missouri

Contents

List of Figures

List of Tables

Acknowledgements

I would like to thank my mother as well as my sister for always believing in me and supporting me. I would also like to thank Timothy Pawlow, who has been a constant positive influence my entire life, for keeping me sane through the ordeal that is graduate school.

I would like to thank Jason Burke for loaning us an S2 during our experimental run, and Romualdo deSouza for the mating CsI(Tl) array. Without these loans the experiment at Texas A&M would not have been possible. I would also like to thank Brian Roeder and Antti Saastamoinen for all of their help during the experiment.

I would like to thank my fellow graduate worker colleagues who helped me through many trying times: Cole Pruitt, Tyler Webb, and especially Kyle Brown, who provided a great deal of mentoring.

I would like to thank Gregory Potel for the many discussions and aid in understanding the phenomena presented in this work. Without his insight the presented phenomena might never have been explained.

Dr. Charity has been monumental in pushing forward the progress of this work and my research. I would like to thank him for his significant insight and patience with me.

Finally, I would like to thank Dr. Sobotka for pushing me to reach my full potential.

Daniel Hoff

Washington University in St. Louis

August 2018

ABSTRACT OF THE DISSERTATION

Spin Alignment Generated in Inelastic Nuclear Reactions

by

Daniel Edward Macan Hoff

Doctor of Philosophy in Chemistry

Washington University in St. Louis, 2018

Professor Lee Sobotka, Chairperson

The spin alignment of inelastically excited ^{7}Li projectiles, when the target remains in its ground state, was determined through angular-correlation measurements between the breakup fragments of ^{7}Li* $(\alpha + t)$. It was found that ^{7}Li* is largely aligned along the beam axis (longitudinal) in this type of inelastic reaction, regardless of the target. This longitudinal alignment is well described by DWBA calculations, which can be explained by an angular-momentum-excitation-energy mismatch condition. These calculations also explain the longitudinal spin alignment of excited nuclei in several other systems, showing the phenomenon is more general. The experiment involving ^{7}Li was performed at the Texas A&M Cyclotron Institute, and used a custom designed detector system consisting of two annular Si-CsI(Tl) telescope arrays.

Chapter 1

Introduction

"I was taught that the way of progress is neither swift nor easy."

—Marie Curie

The aim of this dissertation is to answer the question:

What inelastic nuclear reaction mechanism can generate large longitudinal spin alignment?

The answer turned out to be both simple and interesting. This dissertation will tell the story of getting to that answer, while also presenting the foundations for understanding the phenomenon as well as some interesting things found along the way. This journey includes: an experiment that shattered a hypothesis, quantum-mechanical calculations of a reaction, the realization of an appropriate mathematical formalism after many lengthy discussions, and the reduction of quantum-mechanical calculations into insight that can be readily applied to other reactions.

The generation and manipulation of nuclear spin is a useful tool for many different studies. In particular, g-factor measurements of nuclei, and individual nucleons, are able to provide insight into the complex (internal) many-body nature of these systems. For nuclear science, there are many more g-factors to be measured (e.g. the ground and excited states

of radioactive nuclei) and the spin alignment mechanism outlined in this dissertation can be applied to radioactive beam experiments. In fact, the mechanism may have already been used (unwittingly) for such studies [1].

The rest of the Introduction will discuss simple nuclear models while also highlighting the importance of g-factor measurements for elucidating the more complicated many-body (composite) structure of particles. The basic framework for understanding nuclear reactions is also presented, and some nuclear reactions where polarization phenomena have been observed before are identified, including the reactions that motivated the central thesis. Chapter 2 will give further details on nuclear structure, including a presentation on spin-orbit coupling. Chapter 3 will discuss nuclear reactions, and introduce the concepts of quantum-mechanical scattering theory that will be used in later chapters. Chapters 4 and 5 will detail the experiment that became the foundation of this dissertation, as well as the subsequent data analysis. Chapter 6 will further expand on polarization phenomena in the context of nuclear reactions, before providing a mechanism for generating spin alignment in inelastic nuclear reactions and the consequences of such a mechanism from the perspective of quantum-mechanical scattering theory. Chapter 7 will talk about a follow-up experiment to test the proposed spin alignment mechanism and conclude with a discussion of applications, that may even reach beyond nuclear reactions.

1.1 Mass and Structure of Nuclei

An empirical law for determining the ground-state masses of nuclei was found in the 1930s by Carl Friedrich von Weizsäcker, known as the liquid drop model (LDM). This model treats nuclei as a fluid of neutrons and protons, and attempts to describe nuclear masses across the chart of nuclides (shown in Figs. 1.1 and 1.2), which maps all of the known isotopes according to their number of protons (Z) and neutrons (N). The LDM can be written rather succinctly by an equation for the nuclear binding energy with $A = N + Z$,

$$BE_{\rm Nuc} = a_V A - a_S A^{2/3} - a_C \frac{Z(Z-1)}{A^{1/3}} - a_A \frac{(A-2Z)^2}{A} \pm \delta(A,Z). \tag{1.1}$$

The term with coefficient a_V refers to *volume* interactions, that depend on the number of nucleons. Nuclear density is almost constant, and sits around the "saturation density", $\rho_0 = 0.16$ Nucleons/fm^3, so the volume of a nucleus is approximately proportional to the number of nucleons. The remaining major terms reduce the binding energy. The term with coefficient a_S refers to *surface* corrections, as nuclei are ultimately finite and thus the nucleons on the surface have less interactions than nucleons embedded in the medium. The term with coefficient a_C incorporates the internal *Coulomb* forces, as higher Z reduces the binding energy due to the protons pushing each other apart. The term with coefficient a_A is an *asymmetry* term related to the fact that there are two potential wells being filled, since neutrons and protons are not identical fermions. As the number of nucleons in a particular well increases so does their Fermi energy (from the Pauli exclusion principle) and thus it may become energetically favorable for a proton to change into a neutron or vice versa (via β decay). The last term is a pairing term, which takes into account the fact that neutrons and protons prefer to come in pairs with total spin zero. The empirical LDM is surprisingly accurate for predicting nuclear binding energies and provides a starting point for understanding infinite nuclear matter (relevant for very dense matter, e.g. neutron stars).

The colors in Fig. 1.1 denote the different decay modes of the nuclei, with the black squares showing the stable isotopes. For the lower-mass nuclei, the line of stable isotopes is approximately along the $N = Z$ line, ultimately bending over to more neutron-rich stable isotopes at higher mass due to the increasing Coulomb forces. Away from this "valley of stability", moving along cross-diagonal isobar lines of constant $A = N + Z$, are radioactive isotopes, which can be accessed in experiments by different nuclear reactions. For most of the chart, the area around stability is dominated by β-decay modes (blue and pink squares), which is mediated by the weak interaction allowing protons and neutrons to be converted from one to the other, forcing these nuclei back to the valley of stability, a process driven

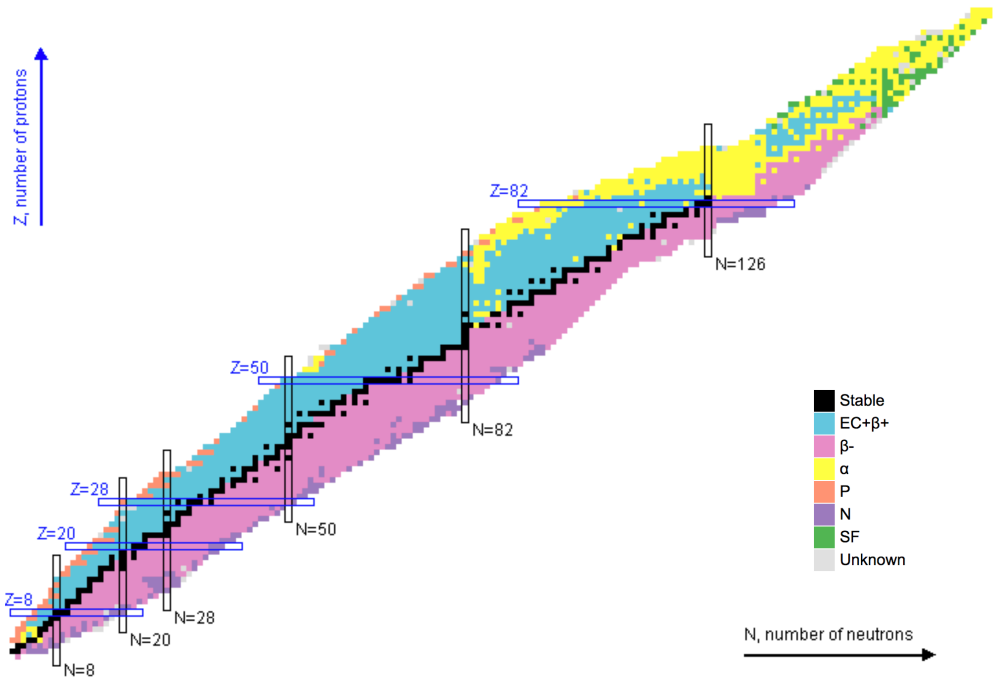

Figure 1.1: Chart of the nuclides, which shows all of the known isotopes. The colors represent the different decay modes of the respective nuclei, from no decay (black squares), to β decay (blue and pink squares), particle emission (orange and purple squares), as well as α decay and spontaneous fission (yellow and green squares).

by the reduction of the asymmetry energy. The ends of the chart are known as the "drip lines", beyond which adding additional nucleons does not result in a lower binding energy with respect to adding a free nucleon. Nuclei beyond the drip lines will only exist as resonances, which will quickly decay by particle emission (orange and purple squares). It is the aim of some newer facilities (specifically FRIB at Michigan State University) to access the more neutron and proton-rich isotopes. At very large mass, α-decay and fission become the predominate decay modes (yellow and green squares). The nuclei in the focus in this dissertation lie in the bottom left corner of the chart in the lower-mass region.

Figure 1.2 gives another perspective of the chart, which shows the vast unexplored territory on the neutron-rich side. It also highlights some of the processes which are thought to be responsible for nucleosynthesis. Of these the r-process, or rapid neutron-capture process, is one of the most notable as it explains the production of very heavy elements in our universe. The search for astrophysical sites of this process is ongoing, although, the recent

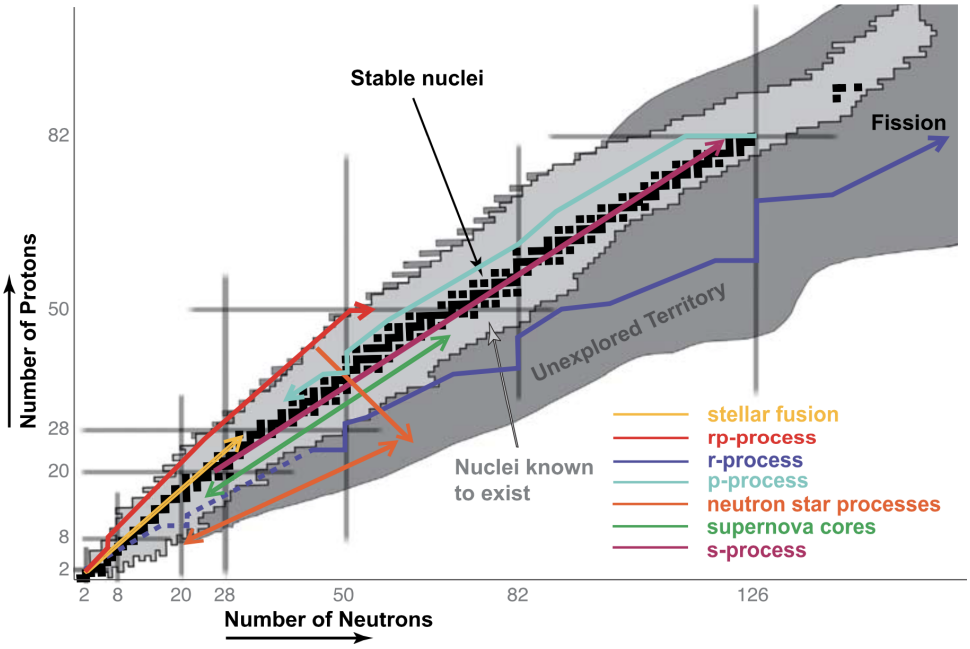

Figure 1.2: A chart of the nuclides which shows a range of predicted isotopes and the nucleosynthetic pathways for creating different nuclei. The large unexplored neutron-rich side is also highlighted.

direct detection of a binary neutron star merger event, and follow-up optical studies, suggest that such events are r-process sites [2].

1.1.1 Independent-Particle Model

The liquid-drop model provides a good scheme for predicting the ground-state masses of nuclei, however, it says little about their structure. The independent-particle model (IPM) is a simple quantum-mechanical model that can be used to start predicting the structure of nuclei[†], especially around closed shells.

Electronic orbitals are a result of Coulomb forces, the magnitude of which tend toward infinity at zero distance. Thus the energy of zero angular momentum states (s orbitals) is significantly lowered, as they have non-zero probability density at zero distance. Nuclear forces are represented by flat-bottomed potentials, which don't "penalize" higher angular

[†]However, the IPM, in and of itself, says little about the masses of nuclei. The incorporation of quantum-mechanical effects into LDM calculations (colloquially known as "macro+micro" calculations) was developed by Strutinsky in the late 1960s [3].

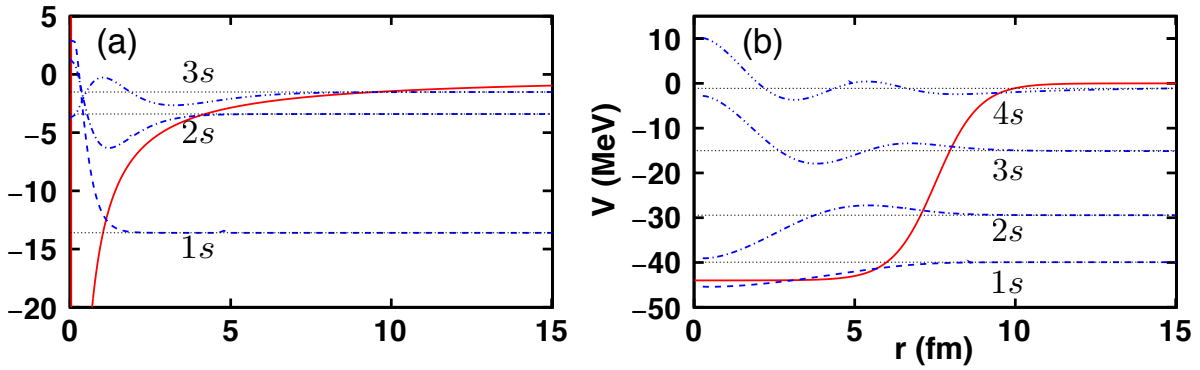

Figure 1.3: The radial wave functions (blue dashed and dashed-dotted lines) for the s electron states in the hydrogren atom (a) and the s neutron bound states in ^{208}Pb (b) are plotted at the energies found in numerically solving the radial Schrödinger equation by discretizing the Hamiltonian. The potentials used in the calculation are shown as the red solid lines. The small black dotted lines show the energy of the state.

momentum states for not having much, if any, probability density near the center of the potential, and thus the shell ordering of nuclei is different from that of atoms. A comparison between the s states of an electron in a hydrogren atom to the s states of a neutron in a ^{208}Pb nucleus is presented in Fig. 1.3. As expected, the nuclear wavefunctions have an increasing number of nodes corresponding to increases in energy, similar to electronic orbitals. However, the nuclear states are more evenly spaced in energy than the atomic case.

In the independent-particle model we treat each nucleon as if it is in a mean-field, i.e. one nucleon feels an *effective* force from the collection of all other nucleons. The effective potential must be short-range, so a Woods-Saxon potential (rounded square well) is often used to parameterize the mean-field potential. The nucleon-nucleus potential in the WS form is given by,

$$V(r) = \frac{-V_0}{1 + e^{(r-R)/a}}, \tag{1.2}$$

where $V_0 \sim 50$ MeV and $a \sim 0.7$ fm. R is typically given as $R = r_0 A^{1/3}$ with $r_0 = 1.2$ fm. The solid red line in Fig. 1.3(b) is of this form. The spherically symmetric Woods-Saxon potential works fairly well for closed-shell nuclei although other nuclei require a deformed potential.

For the proton levels, one also has to consider the Coulomb force with the residual nucleus. The main consequence of adding a Coulomb potential is the introduction of a "Coulomb barrier" that allows for quasi-bound nuclei with dramatically longer lifetimes beyond the proton drip-line and prevents nuclear reactions at low bombarding energies. In another departure from the typical atomic case, nuclear states are not fully specified by just their orbital angular momentum (s, p, d, f etc.), as the mean-field orbit also requires the total angular momentum $\mathbf{J} = \boldsymbol{\ell} + \mathbf{s}_{p,n}$ be specified due to strong spin-orbit coupling present in nuclear forces.

Nuclear levels are also characterized by their parity (whether the mirror image looks the same, +, or not, -), with the convention $\text{spin}^{\text{parity}}$, or J^{π}. Taking the *aufbau* principle from atomic physics and applying it to both neutrons and protons separately in the independent-particle model, we can begin to make structure determinations of nuclei. Fermion degeneracy is more complicated for nuclei than for atoms, as the proton carries charge; making it distinct from the neutron (a result of the internal quark structure). Thus, in the independent-particle model there are two potential wells to be filled and excited states of nuclei are then thought of as single/multiple-particle excitations to higher orbitals.

1.2 History of Intrinsic Spin and Magnetic Moments

A charged particle in a closed system with a well defined angular momentum will generate a magnetic field, i.e. a magnetic dipole moment. For a particle satisfying the Dirac equation (the relativistic Schrödinger equation for massive spin-1/2 particles), with charge e and mass m the magnitude of this magnetic moment is,

$$\mu = \frac{e\hbar}{2m}. \tag{1.3}$$

Equation (1.3) should hold for fundamental particles, and mostly does for the electron (interactions with virtual photons change the overall observed electron magnetic moment by

a small amount). However, Eq. (1.3) does provide the correct order of magnitude for the magnetic moment. Therefore, the magnetic moments of nucleons and nuclei are typically given in units of the nuclear magneton,

$$\mu_N = \frac{e\hbar}{2m_p}, \tag{1.4}$$

with m_p as the mass of the proton.

The magnetic moment, μ, of a particle is directly related to its intrinsic spin, S, by the formula,

$$\boldsymbol{\mu} = \left(\frac{g\mu_N}{\hbar}\right)\mathbf{S}, \tag{1.5}$$

where the g-factor has been introduced, which defines the response of a particle with intrinsic spin to an external magnetic field. In a classical picture, if the charge and mass distributions of a body are the same then $g = 1$. If quantum-mechanical effects are included, all fundamental spin-1/2 particles must have $g = 2$. Large deviations from these values hint at more complicated internal (composite) structure. This can be seen across the chart of nuclides, and even in their constituent nucleons.

1.2.1 Nucleon Magnetic Moments

The existence of quantized intrinsic spin was first shown by Stern and Gerlach in 1922 [4], where they observed a spatial splitting of silver ion beams into distinct groups after passing through magnetic field gradients. This could only be the case if the magnetic moments of silver nuclei were quantized, a result of quantized intrinsic spin. The magnetic field gradients separated the silver ions according to their different orientations of the intrinsic spin, or rather different magnetic substates. Only a few years later in 1926, Uhlenbeck and Goudsmit found that treating the electron with an intrinsic spin of $(1/2)\hbar$ could explain atomic spectra [5]†.

†In fact Kronig, of the Kramers-Kronig relations, had already formulated the effect of a "spinning electron" on atomic spectra but was told by Wolfgang Pauli not to publish the work!

The magnetic moments of the proton and deuteron were measured by Stern and his group [6, 7], and these experiments were the first to measure the magnetic moments of nuclei. To their surprise, they found that the magnetic moments of protons and deuterons were not integers of the nuclear magneton, μ_N, showing that the interactions between nucleons must be more complicated (i.e. they are not fundamental point-like particles). Not long after the discovery of the neutron by Chadwick in 1932 [8], an experiment was performed by Bloch and Alvarez to measure the magnetic moment of the neutron [9] (which is surprising in its own right since the neutron doesn't carry charge) and found the addition of the proton and neutron magnetic moment does not add up to that of the deuteron, hinting that the deuteron cannot be described by a simple non-interacting $n - p$ model.

For decades after the discovery of the neutron, it was thought that protons and neutrons were fundamental, even though measurements of their magnetic moments suggested otherwise. The confirmation of quarks in 1969 from deep inelastic $e - p$ scattering measurements [10, 11], that observed resonances corresponding to nucleon excitations, definitively showed that protons and neutrons are not fundamental. Up to this point, many different particles had been observed (mesons and baryons, e.g. pions and nucleons), and with the introduction of quarks into the Standard Model, these particles could be understood as different combinations of quarks. Quarks come in many "flavors", but the most relevant for this work are the up quark, u, and the down quark, d, which distinguish protons and neutrons

Because of the complicated internal quark structure of nucleons, it is not clear why the proton and neutron have spin $(1/2)\hbar$. This proton and neutron "spin crisis" is still an open question in quantum chromodynamics (QCD). Furthermore, it is not obvious how the quark dynamics couple to the absolute magnetic moment (as has been solved for the electron in quantum electrodynamics). Recent attempts to calculate the magnetic moment of protons and neutrons (as well as other baryons, i.e. three-flavor quark matter) through lattice QCD (LQCD) have given the correct magnetic moment but use unphysically large u and d quark masses (for technical reasons) [12, 13]. Just as calculations of nucleon magnetic moments

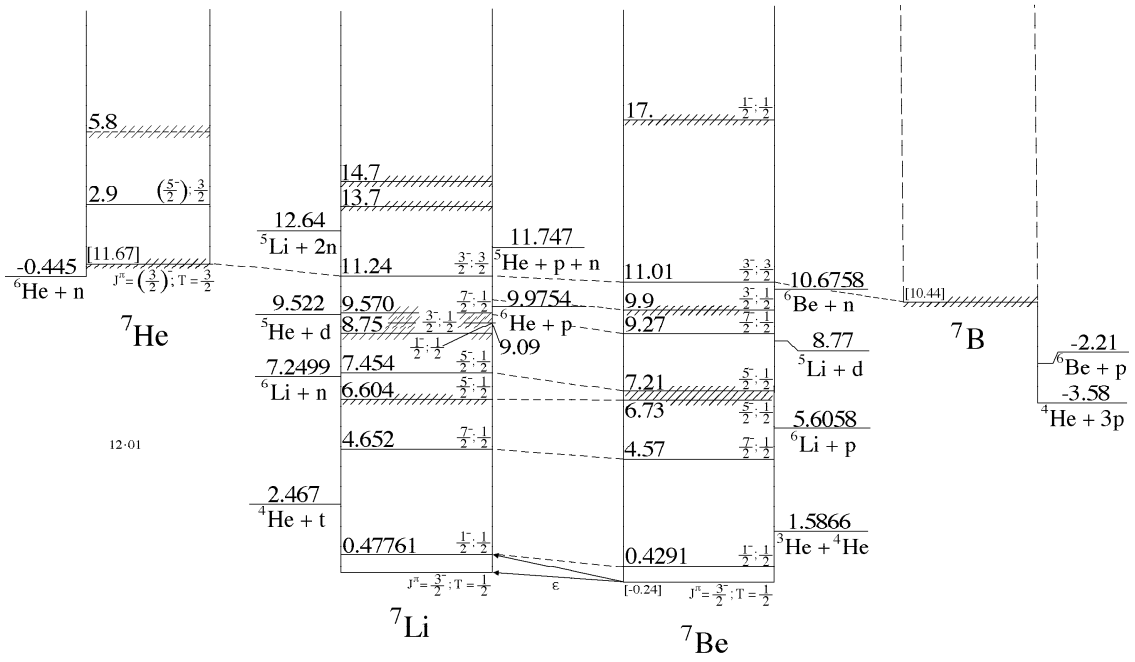

Figure 1.4: A=7 isobar diagram from TUNL, showing the different energy levels and spin/isospin assignments to the these states. Analog states are connected by the dashed lines.

are ongoing, determining the spin and magnetic moments of nuclei, along with their excited states, from first principles has only been achieved for the lightest nuclei.

An Aside on Isospin

Isospin (or isobaric spin) symmetry arises from the fact that the u and d quark have almost the exact same mass. Swapping a valence u quark to a d quark in a proton results in a neutron and vice versa. It is often useful to incorporate isospin symmetry into nuclear structure models. The isospin quantum number, t or T, is then defined. Nucleons are given an isospin number $t = 1/2$ with the projections $t_z = -1/2$ attributed to protons and $t_z = 1/2$ attributed to neutrons. The same formulism for angular momentum is then applied to isospin symmetry. The total isospin projection for a given nucleus is defined as,

$$T_Z = \frac{N - Z}{2}. \tag{1.6}$$

Most nuclear states are characterized by one isospin. By plotting adjacent nuclear masses along an isobar (total A is the same) one finds a connection between states in different nuclei. These corresponding states are called analogs, where all the nuclear quantum numbers are identical except for the projection of isospin[†]. An analog of the ground state is called an isobaric analog state. Figure 1.4 shows an isobar diagrams for the A=7 system. In Fig. 1.4 the similarity between ^{7}Li and ^{7}Be, from a nuclear perspective, is apparent. As such, most of the known states in ^{7}Li have direct analogs in ^{7}Be (connected by the dashed lines in Fig. 1.4), and the difference in energy of these states can be largely attributed to differing Coulomb forces and the mass difference of the neutron and a proton, plus an electron, (0.78 MeV/c^2). Isospin is not a perfect quantum number and so isospin mixing can and does occur. An example of such mixed states will be presented in Chapter 5.

1.2.2 Nuclear Magnetic Moments

Shortly after Stern and Gerlach's discovery of quantized intrinsic spin, methods for determining g-factors blossomed, with measurements of nuclear g-factors still ongoing. These g-factor measurements can give insight into the nuclear wavefunctions and hence nuclear structure. For example, the fact that the deuteron magnetic moment ($0.8574\mu_N$) is not the simple addition of the neutron and proton moments (-1.913μ_N and 2.793μ_N, respectively) suggest that the interaction between the neutron and proton has some d-wave component (i.e. internal angular momentum, $\ell = 2\hbar$). From parity, isospin, and spin symmetry arguments, the lowest-order contributions to the deuteron wavefunction are the s-wave ($\ell = 0\hbar$) and d-wave components. Early (late 1940's) estimates of these d-wave probabilities from measurements of the proton, neutron, and deuteron magnetic moments found that roughly $\sim 4\%$ of the deuteron wavefunction can be attributed to d-wave components [15], although

[†]Isospin generates a useful organizing principle, and was largely developed by Wigner and Feenberg [14].

it was found that the exact form of the nuclear potential would give rise to different d-wave probabilities. Decades later, when sophisticated microscopic nucleon-nucleon potentials had been developed, this result was confirmed, as different microscopic potentials resulted in different d-wave probabilities [16]. The widely used microscopic potentials from Argonne National Laboratory, which reproduce the measured values of the deuteron magnetic dipole moment and the electric quadrupole moment (0.2859 e·fm^2), found a d-wave component of 6%. Although this component cannot be exactly constrained due to the ambiguities associated with microscopic nuclear potentials, measurements of the deuteron magnetic moment tell us Nature is more complicated than one might have originally thought.

Simplistic independent-particle pictures can predict the magnetic moments of heavier nuclei (known as the Schmidt limits), and deviations from this model hint at internal structure more intricate than the IPM would suggest. The magnetic moment is defined in the independent-particle model as,

$$\mu = \langle Jm_J = J | \, \hat{\boldsymbol{\mu}}_z \, | Jm_J = J \rangle \, , \tag{1.7}$$

with the total magnetic moment operator for A nucleons given by,

$$\boldsymbol{\mu} = \sum_{i=1}^{A} g_\ell \boldsymbol{\ell}_i + g_s \mathbf{s}_i. \tag{1.8}$$

For a nucleus with a number of fully-paired nucleons (it has an even number of nucleons in each well, i.e. is even-even) the total magnetic moment should be near zero, since nucleons prefer being in spin-up and spin-down pairs that couple to zero angular momentum.

If one introduces an unpaired valence nucleon to a core nucleus then that nucleon will generate an overall magnetic moment. For a neutron $g_\ell = 0$, because it carries no charge its orbit will not induce a magnetic field. In the case of the proton, which does carry charge, $g_\ell = 1$. The g_s-factor for an isolated proton is $g_p = 5.586$, and $g_n = -3.826$ for a neutron. Working through the vector addition of angular momenta and assuming units of the nuclear

magneton, the coupled angular momenta solutions of Eq. (1.8) will give rise to a magnetic moment,

$$\mu_j = \begin{cases} g_\ell \ell + \frac{1}{2} g_s & \text{if } j = \ell + 1/2 \\ \frac{j}{j+1}\left(g_\ell(\ell+1) - \frac{1}{2} g_s \right) & \text{if } j = \ell - 1/2. \end{cases} \tag{1.9}$$

The bounds made by $j = \ell \pm 1/2$ give the Schmidt limits for magnetic moments in even-odd nuclei. Deviations from these bounds indicate a more complicated structure of the nucleus and require more sophisticated calculations of the internal structure beyond that of the independent-particle model. Several examples of applying these limits and their implications are given below.

^{15}N has 7 protons and 8 neutrons. The largest contribution to the magnetic moment will be from the unpaired proton. Unlike the atomic case, in nuclei the first p shell ($\ell = 1\hbar$) typically goes below the second s shell and thus the unpaired proton occupies this level. Furthermore, the strong spin-orbit coupling of the nuclear force splits the degeneracy of these shells into $p_{1/2}$ and $p_{3/2}$ sub-shells, with the energy of the $p_{3/2}$ shell lower than that from the $p_{1/2}$ shell (another quality different from atoms). For an unpaired proton in a $p_{1/2}$ shell, the predicted contribution to the magnetic moment is -0.264μ_N, close to the experimental value of -0.283μ_N.

^{19}F has 9 protons and 10 neutrons, and again the main contribution to the magnetic moment is the unpaired proton in an open shell (the first s and p shells are filled). The next open shell for the proton is the second $s_{1/2}$ shell, and thus the magnetic moment of ^{19}F should have a similar magnetic moment to that of the proton (since the $s_{1/2}$ state has zero orbital angular momentum a proton in this orbit will not generate a magnetic field), and in fact it does. The experimentally measured value is 2.629μ_N.

^{7}Li has 3 protons and 4 neutrons and the unpaired proton lies in the $p_{3/2}$ shell. The independent-particle model predicts the contribution of this proton to the magnetic moment to be 3.793μ_N, which is significantly larger than the experimentally measured value of

$3.256\mu_N$. This discrepancy indicates that more sophisticated models are needed to describe the magnetic moment of ^{7}Li. Although, instead of increasing the degrees of freedom, this anomalous magnetic moment can be described by reducing the degrees of freedom. ^{7}Li is well accepted to be an α-cluster nucleus, a phenomenon that arises in lighter nuclei due to the very large binding energy of α particles. In this picture, ^{7}Li is described by a cluster α + ^{3}H, and calculations with this model recover the magnetic moment while also explaining the very large electric quadrupole moment (4.06 e·fm^2) [17]. Thus, there are correlations amongst the seven nucleons in ^{7}Li that are better captured by an interacting 2-body cluster model than a non-interacting independent-particle model. Green's function Monte Carlo (GFMC) calculations, a more sophisticated method utilizing nucleon-nucleon interactions, also predict the properties of ^{7}Li very well [18], as well as predict α-clustering in nuclei (specifically ^{8}Be) [19]. The treatment of ^{7}Li as an α-cluster nucleus will have later implications, as the quantum-mechanical scattering calculations for the reaction of interest in this dissertation rely on the $\alpha - t$ model.

1.3 Techniques for Measuring g-factors of Radioactive Nuclei

The measurement of magnetic moments arising from intrinsic spin require the nucleus of interest to populate specified magnetic substates. A system of nuclei that only populate one magnetic substate is fully *polarized*, while a system that is equally populated by only $m_J = \pm J$ magnetic substates is fully *aligned* along a given quantization axis. In this dissertation, the quantization axis will always be defined along the beam axis, hence *longitudinal* alignment refers to spin alignment parallel to the beam axis. A comparison between polarization and alignment is present in Fig. 1.5, where the length of the arrows represent the normalized magnetic substate populations of aligned ^{7}Li$^*(J^\pi = 7/2^-)$ generated in inelastic collisions [Fig.1.5(a)], and ^{7}Li$^*(J^\pi = 7/2^-)$ polarized by the common "brute force" method of high magnetic field and very low temperature [Fig.1.5(b)]. The behavior of a spin polarized or aligned system in a magnetic field allows for the precise measurement of magnetic

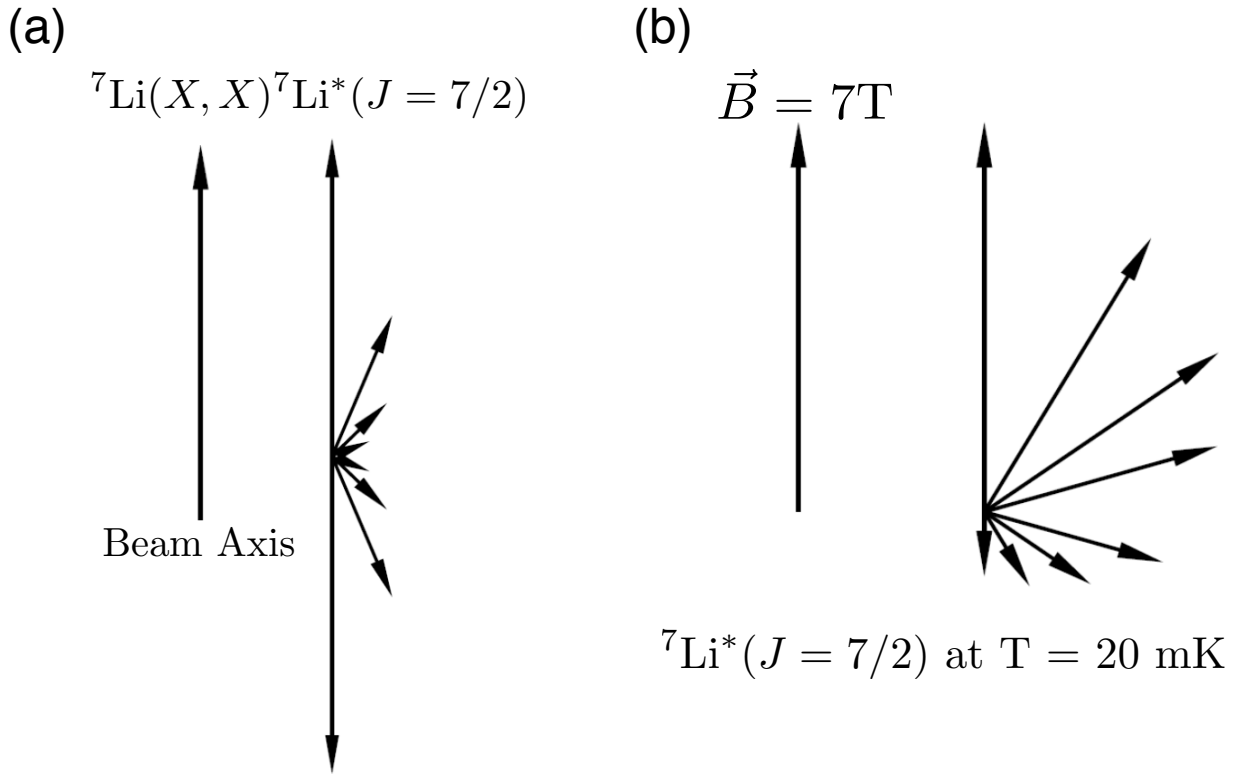

Figure 1.5: A comparison of the spin alignment generated in inelastic collisions of ^{7}Li* to the $7/2^-$ state (a) to polarization of the same state generated from low temperature and high magnetic field (b). The length of the arrows represent the normalized population of m_J states.

moments, i.e. g-factors. For example, when a particle possessing a magnetic moment is introduced to a static magnetic field, it will precess around this field at its Larmor frequency. By introducing a smaller oscillating magnetic field near this frequency, perpendicular to the static field, the spin orientation can be manipulated and resonant signal produced (in bulk materials). The relationship between the resonant frequency and the magnitude of the static magnetic field is defined by the particle's g-factor. Explaining small deviations in the resonant frequencies, arising from known g-factors of nuclei, due to atomic and molecular interactions is the basis of most NMR experiments.

Measuring the g-factors of short-lived radioactive nuclei is a bit more complicated, as these radioactive elements are typically only available via ion-beam experiments. Perhaps the simplest way to generate polarized ion beams is through the same method applied by

Stern and Gerlach. By passing the ions through a magnetic field gradient and only selecting one of the resulting populations, the beam will be, by definition, polarized. Maintaining the polarization can be difficult, although this technique was realized decades ago (1960s), and was used to generate proton and deuteron polarized beams [20, 21].

The "brute force" method has been used in nuclear experiments at the UNISOR nuclear orientation facility to determine the magnetic moments of hard-to-access nuclei [22, 23]. This method of spin control has also been used to generate polarized beams for analyzing-power measurements, which give insight into nucleon-nucleon interactions [24].

Techniques such as β-NMR and the transient-field method allow one to measure g-factors for radioactive nuclei. The former, uses the fact that β particles are emitted in the opposite direction to the spin orientation of the original nucleus (a peculiar feature of the weak interaction), thus the $\beta-$decay angular distribution from a system of polarized nuclei will be asymmetric with respect to the direction of polarization. Applying a frequency modulated radio-frequency (RF) signal over the resonance, known as the adiabatic fast passage method, will remove polarization provided the central frequency is the Larmor frequency of the nucleus and the modulation is much faster than the relaxation time. Utilizing the adiabatic fast passage method, the asymmetric β-particle angular distribution from a polarized source will be destroyed, providing a resonant signal with respect to measurements with the RF turned off.

A promising method for generating the initial polarization of radioactive nuclei is optical pumping, which takes advantage of the hyperfine interaction of electrons and nuclei (magnetic-dipole interactions). By shining right-handed circularly polarized laser light (at a specific frequency) onto a target nucleus, the nucleus is forced to populate a particular magnetic substate, generating polarization. Several β-NMR experiments that utilized optical pumping have been performed on radioactive ion beams [25, 26, 27].

The g-factor of ^{9}C was measured through β-NMR measurements by two different experiments [28, 29]. The ^{9}C nucleus is a good candidate for the independent-particle model as a

low-mass even-odd nucleus with one valence neutron in an open p sub-shell. Applying Eq. (1.9), one can treat ^{9}C as a ^{8}C core with a neutron added to the $p_{3/2}$ shell. Thus, $j = 1+1/2$, and one obtains,

$$\mu_{(^{9}C)} = (1/2)(-3.826) = -1.913\mu_N. \tag{1.10}$$

The predictions for the magnetic moment in this simple scheme vastly over predict the experimental value for the magnetic moment (-1.3915μ_N). The experimental value is fairly well reproduced by cluster-model calculations (asumming $\alpha-^{3}\mathrm{He}-p-p$ structure) that also reproduce the magnetic moment of the isobaric analog state in ^{9}Li [30]. Shell-model calculations also reproduce the anomalous magnetic moment, and indicate that pairing between protons is broken. Furthermore, introducing isospin non-conserving currents bring the calculations even closer to experiment. Once again, measurements of magnetic moments hint at a more complicated underlying structure.

An alternative, the transient field method used the fact that ions swiftly traversing a ferromagnetic material experience magnetic fields of order $\sim$500 Tesla, inducing Larmor precession. The dynamics of this precession is related to the magnitude of the transient magnetic field, the life-time of the state, and its g-factor. If the initial magnetic substate population of the ions is non-isotropic, then this precession causes a change in the decay angular correlations.

For example, Davies et al. measured the g-factor for the first 2^{+} excited state in ^{38}S via the transient-field method [1]. If one treats the excitation of ^{38}S as two valence neutrons being excited with a weakly interacting ^{36}S core (which should have zero magnetic moment since it is an even-even nucleus), then we expect the first 2^{+} state to have a negative g-factor, the same sign as the neutron's g-factor. Instead, they observed a g-factor of $g_{2^{+}} = 0.13(5)$. This indicated that the introduction of two neutrons changed the configuration space of the nucleus, i.e. the total structure of the nucleus was changed. A very interesting aspect of this experiment was that the requisite spin alignment for the measurement was generated

through a nuclear reaction, and the alignment generating mechanism will be exposed in this dissertation.

1.4 Spin Polarization/Alignment Generated in Nuclear Reactions

Nucleon-nucleon and nucleon-nucleus scattering are of considerable interest to nuclear science. For example, these processes are essential for the generation of the elements in the Big Bang nucleosynthesis and the nucleosynthetic processes that generate the elements in the periodic table. However, these types of reactions are only a small subset of all nuclear reactions. Reactions between nuclei heavier than an α particle are generally called heavy-ion collisions. Only for intermediate energies (well above the Coulomb barrier and below the regime of relativity) and high mass can nuclear collisions be understood semiclassically, leading to concrete pictures of the reaction mechanisms. To understand the generation of polarization and/or alignment of exit-channel fragments in nuclear reactions it is necessary to have a good grasp on these underlying reaction mechanisms.

One can characterize reactions by *impact parameters*, b. The impact parameter can be mapped semi-classically to the angular momentum generated in the reaction, $L = p_\infty b$, where p_∞ is the momentum of the incoming projectile at an infinite distance from the interaction (i.e. the momentum of the beam).

Classically for a nuclear reaction to occur, the projectile nucleus must have a bombarding energy above the Coulomb barrier. Below this barrier the projectile will be scattered by Coulomb forces, otherwise known as Rutherford scattering. Above this barrier, the two nuclei can get close enough for the strong nuclear force to come into play. The many different nuclear reactions are differentiated by their impact parameters, and thus by their L-space contribution to the total reaction cross section. Figure 1.6 gives a rough sketch for mapping the impact parameter to the available L-space for the total reaction cross section. The size of the colored circles represent the available phase space for a certain impact parameter. As the size of the impact parameter grows, the area of the phase space increases further

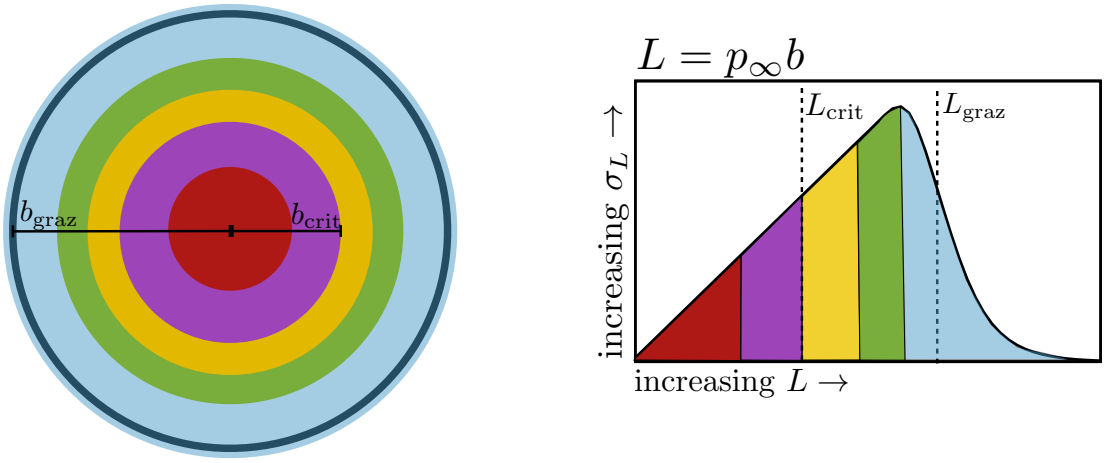

Figure 1.6: A sketch of how the different impact parameters between the projectile and target map to different angular momenta in the reaction, and the corresponding contribution to the total reaction cross section. The different colors/shades provide a rough mapping of the different impact parameters to the angular momentum generated in the reaction (collision). As the impact parameter is increased, there is more available area to interact with and thus cross section per L-wave increases. At sufficiently large impact parameter there are no nuclear reactions, i.e. only Coulomb scattering.

resulting in a larger probability of interaction and a "dart board" like pattern. The partial reaction cross section, the solid black line in Fig. 1.6, decomposes the total reaction cross section into the contributions from different angular momenta, corresponding to a given impact parameter (the mapping is sketched by the different colored/shaded regions). The integration of the solid black curve gives the total nuclear reaction cross section for a given system and bombarding energy.

Small impact parameters correspond to head-on and close collisions (the red and purple sections in Fig. 1.6) which can result in fusion, massive breakup, and fragmentation reactions, depending on the bombarding energies. Above a critical impact parameter, b_{crit}, corresponding to an L_{crit}, these processes will no longer contribute to the total reaction cross section and other processes become favourable.

Moving up in impact parameter, in very heavy ion collisions there is a region of the L-space (yellow and green in Fig. 1.6) where deep inelastic collisions occur. This designation refers to the large transfer of center-of-mass kinetic energy to the excitation energy in the

system[†]. As the two nuclei come together they are excited, and the longer they are in contact the more kinetic energy is converted to internal excitation of the reaction partners. If they are in contact for long enough that the projectile makes a full "orbit" around the target nucleus, then we move into the regime of compound-nucleus formation, so long as there is a barrier to trap the projectile. Some have called these "nuclear molecules" [31]. Interestingly, this mechanism was tested and largely confirmed through polarization measurements of the resulting fragments [32].

The largest impact parameters (light blue region in Fig. 1.6) represent peripheral, or grazing, collisions near the nuclear surfaces. The reactions in this region are typically called direct reactions, which include inelastic, and one/few nucleon transfer reactions with modest transfer of kinetic energy into internal excitation. It will be shown in later chapters that the studies of the reaction of interest (an inelastic process) are consistent with this categorization, and some examples of transfer reactions will also be presented in Chapter 5.

At even larger impact parameters, $b > b_{\mathrm{graz}}$, ions will follow Coulombic trajectories. Even in this regime nuclei can be excited via Coulomb forces, otherwise known as Coulomb excitation. However, this phenomena is not limited to nuclear excitations in ion-beam experiments, as it has also been observed for atomic transitions of high-Z helium-like and hydrogen-like atoms at intermediate energies [33].

In compound nucleus [34, 35, 36, 37], quasielastic [38], and deeply inelastic reactions [39, 40, 41, 42, 43, 44] of heavy ions, the reaction orbital angular momentum, L, dwarfs any intrinsic spin carried by the projectile or target. Since L is defined by the cross product of the radius of interaction and the momentum of the interaction, L is oriented transverse to the beam axis. The exit-channel fragments in these types of reactions acquire spin from the large reservoir of L and thus are characterized by spin alignments with small projections on the beam-axis. These spin alignments can be so strong that particles emitted from the spinning fragments exhibit a forward-backward preference as they cast off ejectiles perpendicular to

[†]These collisions are have similar observables to the deep-inelastic processes mentioned previously for the discovery of quarks, but are not very similar in the underlying mechanisms.

the spin direction, a fact that has been used for fragment-spin determination [39, 41, 44].

In reactions dominated by the strong interaction, the cases for spin alignment with large projections along the beam axis (longitudinal) are usually limited to modest modifications of the spin projections from a uniform distribution [45, 46]. Large longitudinal alignment has been seen in projectile fragmentation [47], though not at the magnitude shown in this dissertation and motivating work [48]. On the other hand, at intermediate to ultra-relativistic energies, Coulomb excitation will produce large longitudinal alignment [49, 50, 1].

The magnitude of spin alignment for a given magnetic substate population is quantified by the scalar, $\mathcal{A}$ (sometimes called P_{zz}),

$$\mathcal{A} = \sum_{m_f} \frac{3m_f^2 - J(J+1)}{J(2J+1)} \rho^J_{m_f,m_f} \tag{1.11}$$

where ρ is the density matrix of particle of interest, and the diagonal elements of the density matrix represent the population of the particular magnetic substate. $\mathcal{A} = 1$ corresponds to the largest possible alignment along the beam-axis (which we have chosen as our quantization axis) and $\mathcal{A} = -1$ is the largest possible alignment transverse to the beam-axis. For example, the largest reported alignment from projectile fragmentation reactions is $\mathcal{A} = 0.35$, which was generated in the population of a $J^\pi = 19/2^-$ high spin isomer in ^{43}Sc from fragmenting ^{46}Ti at 500 MeV/u. The magnitude of alignment for inelastically excited projectiles at intermediate energies is around $\mathcal{A} \sim 0.5$ [48, 51, 52]. This parameterization of alignment will be used in later chapters to quantify the magnitude of alignment generated in nuclear reactions.

1.5 Motivation and Hypothesis

The reactions explicitly studied in this dissertation are

$$^7\text{Li} + \text{C/Be/Al} \rightarrow ^7\text{Li}^* \text{ [4.6 MeV]} + \text{C/Be/Al[g.s.]}, \tag{1.12}$$

which were performed in August of 2015 at the Texas A&M Cyclotron Institute. The motivation for the experiment that would become the foundation of this dissertation, came from the observation of large longitudinal spin alignment of inelastically excited ^{7}Be projectiles, when the ^{9}Be target remained in its ground state [48]. The mechanism initially proposed stemmed from the unusual molecule-like structure of ^{9}Be, where the valence neutron is in a molecular orbital of the $\alpha-\alpha$ (^{8}Be) core. Since peripheral collisions dominate single inelastic excitations, it was thought that the valence neutron in ^{9}Be was "tickled" by the incoming ^{7}Be and the ^{9}Be subsequently spin flipped, transferring spin to the excited ^{7}Be. Due to the structure of ^{9}Be, certain orientations would result in breakup and the reaction channel of interest would not be populated by such events. To test this hypothesis, an experiment was scheduled using a ^{7}Li beam on three different targets, including ^{9}Be, with one of the targets having zero spin in its ground state (^{12}C). The excited state of interest, ^{7}Li* [4.63 MeV], is a direct analog to the 4.57 MeV state in ^{7}Be where large longitudinal spin alignment was initially observed [48]. This was one of the main motivations for using a ^{7}Li beam in the experiment, as the structure of the projectile would be analogous to the previously used ^{7}Be. Furthermore, in the production of ^{7}Be by projectile fragmentation it is possible that the ^{7}Be produced has some initial polarization or alignment. For a stable ^{7}Li beam no initial polarization or alignment is possible. If large longitudinal alignment of inelastically excited ^{7}Li projectiles was observed in scattering with a spin-zero target then the spin-flip hypothesis would be ruled out. Sure enough, that is exactly what was observed and the search for an alignment mechanism capable of generating large longitudinal spin alignment, independent of the target, began.

Chapter 2

Nuclear Structure

"The shell model, although proposed by theoreticians, really corresponds to the experimentalist's approach. It was born from a thorough study of the experimental data, plotting them in different ways, and looking for interconnections."

—Maria Goeppert-Mayer

To fully understand nuclear reactions, one needs a good grasp of nuclear structure. For objects the size and mass of nuclei (r$\sim$fm , m$\sim$1GeV/c^2), quantum mechanics plays a critical role. Just as for atoms, the first step is to solve Schrödinger's equation with the appropriate Hamiltonian. Whereas for atoms the interaction is well defined, this is not the case for nucleon-nucleon interactions. Potentials used to construct the nuclear Hamiltonian are often phenomenological potentials, much like the potentials used to describe van der Waals forces for molecules. These potentials can either be used in the mean-field approach, i.e. nucleon-nucleus interactions, or one can start from effective nucleon-nucleon (NN) interactions. There are many experimentally constrained NN potentials, such as Argonne-V18 and CDBonn. Efforts are ongoing to get a satisfactory first-principle description of NN forces from quantum chromodynamics, such is the aim of Chiral Effective theory and Lattice QCD. It should be noted, that because the NN forces are effective interactions, there are higher-

order interactions, e.g. 3 nucleon forces (3N), that also have to be accounted for. These 3N forces are analogous to those introduced for three-body calculations of atoms [53].

Even without sophisticated nucleon-nucleon potentials we can learn a great deal about nuclei from basic quantum-mechanical principles. A prime example is the observation and description of "magic numbers". Certain "magic numbers" of nucleons give the corresponding nuclei greater binding energy, and thus greater stability. These features are apparent in the large natural abundance of certain isotopes, and also in their separation energies (the energy required to remove a nucleon) and β-endpoint energies. It was eventually found that these numbers could be explained by a strong spin-orbit coupling in the nuclear Hamiltonian, much larger than in the atomic case. From the introduction of spin-orbit coupling it was determined that these "magic numbers" correspond to shell closures; The large separation energies (required for nucleon removal) of nuclei at shell closures is analogous to the large ionization energies of noble gases.

Although understanding nuclear structure is imperative for nuclear reactions, there is currently not much consistency between structure and reaction calculations. For instance, the phenomenological potentials used for nuclear scattering typically do not reproduce the correct nuclear structure. Consolidating these phenomena, and increasing the predictive power of nuclear reaction theory, is still being researched. One of the most notable theories attempting to do so is the Dispersive Optical Model (DOM), which uses dispersion relations to constrain, and mutually inform, the nuclear structure (real potentials) and reactions (imaginary potentials). Currently this model is only feasible near closed shell nuclei and requires substantial experimental input for fitting the phenomenological potentials. Even with the disconnect between structure and reactions, it is important to explore the foundations of understanding nuclear structure.

2.1 Spin-Orbit Coupling

In atomic spectra the splittings due to coupling of the electron spin to its orbital motion are measureable but are not that large, and thus this coupling is largely ignored for structure considerations (although it is necessary for atoms with large Z that require relativistic corrections). This is not the case for nuclei. In fact, spin-orbit coupling is so essential to understanding nuclear structure that Eugene Wigner, Maria Goeppert Mayer and J. Hans D. Jensen were awarded the 1963 Nobel Prize in Physics for their contributions to implementing spin-orbit coupling ($\mathbf{s} \cdot \boldsymbol{\ell}$) into the nuclear shell model. The introduction of this phenomenon explains the "Magic Numbers" that correspond to shell closures. These magic numbers are, 2, 8, 20, 28, 56, 82, and 126 (for neutrons), and are identified in Fig. 2.1, which uses a harmonic-oscillator potential for the calculations. Unlike the atomic case, the states with aligned spin and orbital angular momentum are lower in energy, i.e. $p_{3/2}$ is lower in energy than the $p_{1/2}$ and a qualitative argument for this will be presented below.

The simplest form for a spin-orbit potential that conserves parity is,

$$V_{LS} \propto \mathbf{s} \cdot (\mathbf{p} \times \nabla V). \tag{2.1}$$

Here the spin, $\mathbf{s}$, is a *pseudo*-vector meaning its direction doesn't change with respect to parity. The momentum, $\mathbf{p}$, is a polar vector, and its direction does change with parity, as does the vector ∇V which is the gradient of the mean-field potential. However, the cross product of two vectors is also a pseudo-vector. Thus V_{LS} behaves like a pseudo-vector and does not change with parity.

For a spherically symmetric potential the only contribution from the gradient, ∇, is along the radial component, i.e. $\nabla V = \hat{\mathbf{r}} dV/dr$. Thus classically we arrive at the formula,

$$V_{LS} \propto \mathbf{s} \cdot (\mathbf{p} \times \hat{\mathbf{r}} \frac{dV}{dr}) = \mathbf{s} \cdot (\mathbf{p} \times \frac{\mathbf{r}}{r} \frac{dV}{dr}) = -(\mathbf{s} \cdot \boldsymbol{\ell}) \frac{1}{r} \frac{dV}{dr}, \tag{2.2}$$

remembering that $\boldsymbol{\ell} = \mathbf{r} \times \mathbf{p}$. While this gives us the approximate form of the spin-orbit potential, this tells us nothing about the magnitude or sign. To understand why the sign for spin-orbit coupling is different for nuclei compared to atoms, it is useful to look at the effect of Thomas precession on the spin-orbit splitting on atomic spectra. Here, the formalism from Jackson is followed [54]. For an electron with intrinsic spin, $\mathbf{s}$, giving it a magnetic moment defined by Eq. (1.4) with $g = 2$, the spin-interaction energy with the electromagnetic field is given by,

$$U' = -\frac{e}{m_e c}\mathbf{s} \cdot \mathbf{B} + \frac{1}{m_e^2 c^2}(\mathbf{s} \cdot \boldsymbol{\ell})\frac{1}{r}\frac{dV}{dr}. \tag{2.3}$$

In this case, $V(r)$ is the regular Coulomb force. The first term in Eq. (2.3) generates Zeeman splitting, however, the second term over predicts the change in energy for spin-orbit interactions, also know as the fine structure. Thomas noticed that the rest frame of the electron rotates with respect to the induced magnetic field, thus one must modify the interaction energy by,

$$U = U' - \mathbf{s} \cdot \boldsymbol{\omega_T}, \tag{2.4}$$

where $\boldsymbol{\omega_T}$ is the precessional frequency in the rest frame of the electron with respect to the induced magnetic field and this is caused by the acceleration of its atomic orbit. After performing the relevant Lorentz transforms (see Jackson [54]) in the non-relativistic limit one finds,

$$\boldsymbol{\omega_T} \overset{\text{NR}}{=} \frac{1}{2c^2}\mathbf{v} \times \mathbf{a}, \tag{2.5}$$

where $\mathbf{v}$ and $\mathbf{a}$ are the usual velocity and acceleration. The Coulomb force is spherically symmetric, and from similar arguments to those used above, we find $\mathbf{a} = \frac{1}{m}\frac{\mathbf{r}}{r}\frac{dV}{dr}$. From here the Thomas precession is derived,

$$\boldsymbol{\omega_T} \overset{\text{NR}}{=} -\frac{1}{2c^2}\frac{\mathbf{v}\times\mathbf{r}}{m_e}\frac{1}{r}\frac{dV}{dr} = \frac{1}{2m_e^2c^2}\boldsymbol{\ell}\frac{1}{r}\frac{dV}{dr}. \tag{2.6}$$

Thus the Thomas precession reduces the spin-orbit coupling of the electromagnetic energy by $\frac{1}{2}$, giving an interaction energy,

$$U = -\frac{e}{m_e c}\mathbf{s}\cdot\mathbf{B} + \frac{1}{2m_e^2c^2}(\mathbf{s}\cdot\boldsymbol{\ell})\frac{1}{r}\frac{dV}{dr}, \tag{2.7}$$

and this results in the correct energy level splitting for atoms. However, for nuclei there is no term in the "nuclear" force field to cancel out the effect of Thomas precession and the overall interaction energy from the spin-orbit coupling for nuclei is qualitatively,

$$U_N \simeq -\mathbf{s}\cdot\boldsymbol{\omega_T} = -\frac{1}{2m_N^2c^2}(\mathbf{s}\cdot\boldsymbol{\ell})\frac{1}{r}\frac{dV}{dr}, \tag{2.8}$$

and thus the ordering of the spin-orbit splitting for nuclei will be opposite to the ordering for atomic levels. This argument, while it is qualitatively correct, is misleading. The magnitude of spin-orbit coupling from Thomas precession is too small to explain spin-orbit effects in nuclei. Research is still on-going to find the exact source of spin-orbit coupling in nuclei, but there are suggestions that it arises from more complicated nuclear interactions, i.e. 3N forces, tensor interactions, as well as meson exchange currents [55, 56].

Although the relative magnitude of Eq. (2.8) is too small, this form of the spin-orbit coupling will be used later when incorporating spin-orbit effects into nuclear scattering, however, instead of using the mass of a nucleon the mass of a charged pion is used ($m_{\pi^\pm} = 139.57$ MeV/c^2), which provides the correct magnitude for explaining scattering data.

2.2 Shell and Other Models

The shell model expands on the independent-particle model and introduces configuration mixing of the different nucleon orbits to take into account residual forces not accounted for

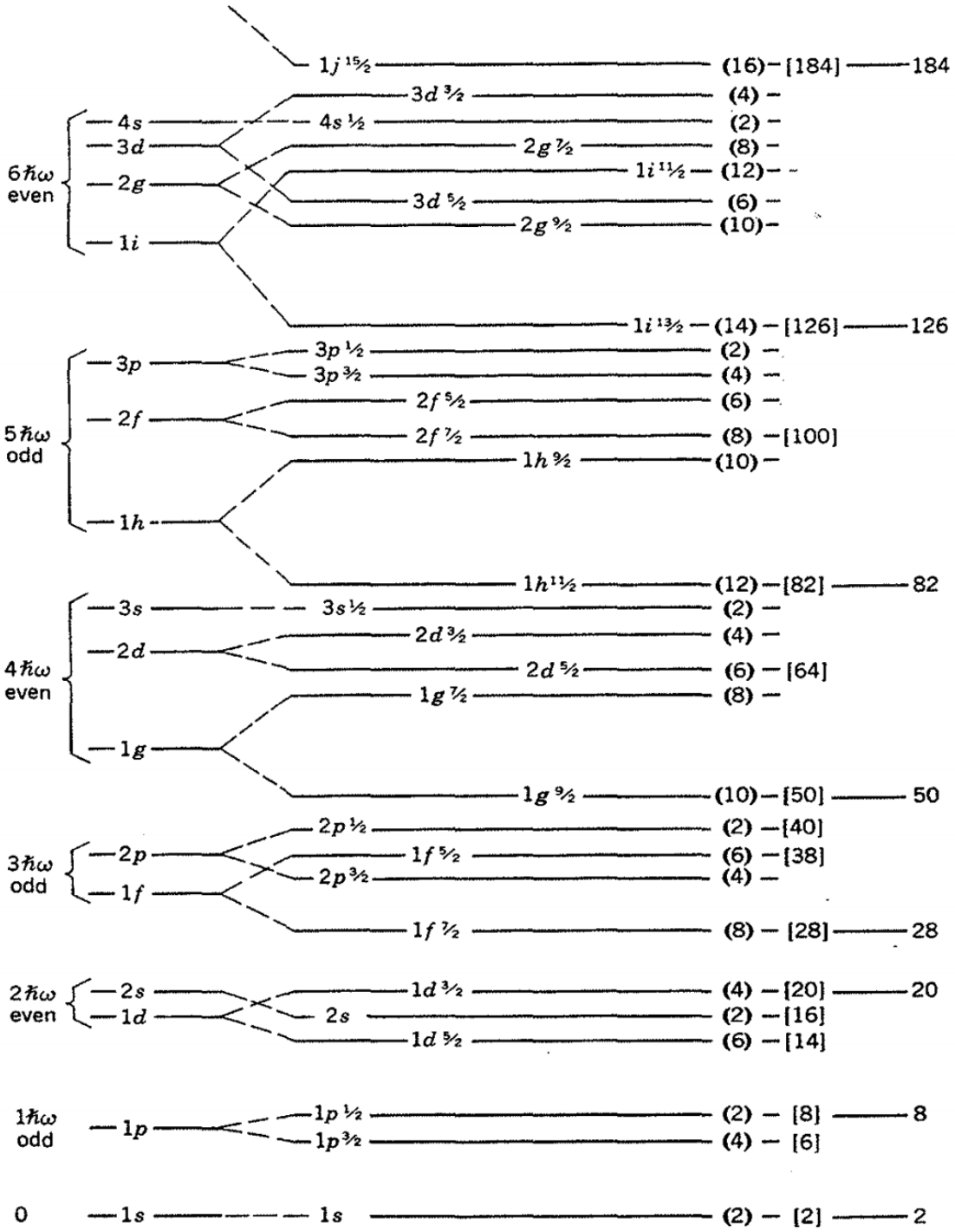

Figure 2.1: Diagram the energy levels in an isotropic 3D-harmonic oscillator potential after introducing spin-orbit coupling. Image from *Nuclear and Radiochemistry* by Friedlander, Kennedy, Macias, and Miller.

in the mean-field approach. Typically for these calculations a harmonic-oscillator potential is used for the mean-field, as there are analytic solutions for the wavefunctions. This is not a problem for the calculation bound states, but if one wants to calculate open decay channels, or scattering states, the harmonic oscillator potential will not suffice because the magnitude of the potential increases to infinity as the radius increases (i.e. there are no continuum solutions as the asymptotic forms will be incorrect).

Once a configuration basis has been chosen, a core nucleus can be defined that often has closed shells, or sub-shells, of neutrons and protons. The core is considered inert and the configuration based on the remaining valence nucleons are considered. Nuclei one nucleon off these shell closures typically take on a spin of the *valence* nucleon. For example, ^{16}O is a doubly magic nucleus with 8 protons and 8 neutrons. Because it has an even number of protons and neutrons it has $J^\pi = 0^+$ in its ground state . ^{17}O can then be described as a ^{16}O core with a valence neutron in the $d_{5/2}$ orbital and thus it's ground state is characterized by $J^\pi = 5/2^+$ in the independent-particle model. In the case of multiple valence nucleons each of their spin states will couple to give the resulting ground state. For nuclei with an odd number of nucleons in each well, the ground state will take on a mixture of the valence nucleon states. ^{14}N has a valence neutron and proton in the $p_{1/2}$ shell. In the shell model the valence neutron and proton couple to a "triplet" state, and the resulting groundstate has $J^\pi = 1^+$. The first excited state at 2.3 MeV can then be thought of as a "singlet" state with $J^\pi = 0^+$, analogous to level ordering of the deuteron. This is in contrast to the molecular case where singlet states are typically lower in energy. The preceding cases are extremely simple, and more typically the shell model produces nuclear states that have contributions from a number of different nucleon configurations.

There are even more complicated models utilizing the shell model such as the *No-Core* Shell model (NCSM). As the name implies, no core is specified and so all of the nucleons are included in the configuration mixing. While this does provide more accurate energy-levels and overall structure, it is computationally expensive to do calculations for heavy nuclei.

There have also been attempts to unify shell model calculations with reactions, such as the shell model embedded in the continuum (SMEC) [57, 58, 59]. This type of formalism is of necessity for nuclei around the drip lines [51].

A powerful technique for solving scattering problems (and many differential equations) is by Green's function methods. In this context the Green's function is typically called a *propagator*, which specifies the probability amplitude for going from one spatio-temporal state to another. By focusing on the propagator between states diagrams of processes can be drawn and calculated, otherwise known as Feynman diagrams. One such model that utilizes the propagator formalism is the Dispersive Optical Model (DOM), which calculates observables via propagator methods after specifing fitted optical potentials.

Another method that utilizes the propagator formalism is Green's function Monte Carlo (GFMC), which uses the Green's function in many body methods to perform variational calculations of operator expectation values. This method is very powerful and predicts many properties of nuclei up to $A = 12$, but suffers from similar computational problems to the NCSM for treating very heavy nuclei as it only involves microscopic nucleon-nucleon interactions [19].

Another method, that has had a resurgence in use for nuclear structure and reaction calculations, is the coupled-cluster (CC) method. This method has been applied to atoms and molecules for chemical reaction and molecular structure calculations for decades [60, 61, 62]. This method relies on Thouless' theorem[†] which allows one to make special groupings of particle-hole excitations in many-body perturbation theory to aid calculations [63]. This method is an *ab-initio* method that only depends on the microscopic nucleon-nucleon interactions (just like GFMC), and there have been recent attempts to construct nucleon-nucleus potentials using CC methods [64]. There are also efforts to integrate Monte Carlo methods into CC calculations, which greatly reduces the computational overhead allowing higher-order excitations to be incorporated (resulting in more accurate calculations) [65].

[†]In fact Thouless' work and CC theory were originally crafted for nuclear structure calculations.

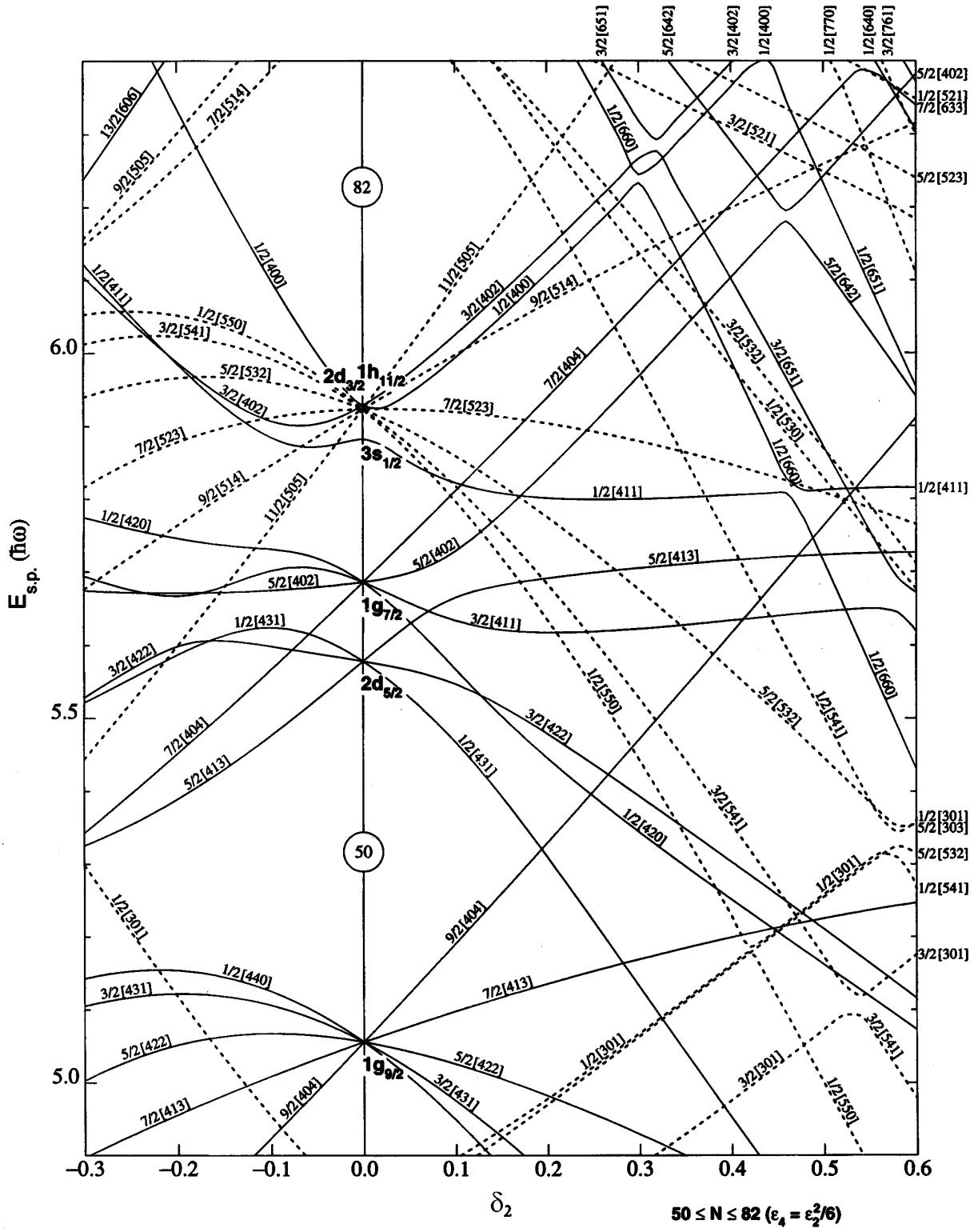

Figure 2.2: A Nilsson diagram for neutrons $50 < N < 82$, showing the change in single-particle energy levels as a function of deformation.

2.3 Deformed Nuclei

Singly or doubly magic nuclei (with a magic number of protons and neutrons) are typically spherically shaped in their ground state. This is confirmed by the small electric quadrupole moments of nuclei at shell closures. Nuclei typically become more deformed in their ground state as they move away from these shell closures. For such nuclei, some of the excited states can be thought of as dynamic motion of the deformed ground state, otherwise know as *collective* motion of nucleons. This collectivity of motion opens up many different excitation modes, most notably rotational modes. An attempt to understand these collective modes was first tackled by Nilsson, who introduced a deformation parameter in the modified oscillator potential in order to describe the deformed structure of nuclei [66]. When the nucleus is highly deformed, the ordering of levels will be substantially changed. An example of a Nilsson diagram, which displays a modified level ordering with deformation, is provided in Fig. 2.2. In the Nilsson scheme, negative values of the parameter δ_2 correspond to oblate deformation (similar in shape to a door knob), while positive values correspond to prolate deformation (similar in shape to an american football). If a shifted single-particle state has a much higher spin and opposite parity than its neighbor states, then the state is called an *intruder*. If this intruder state is located around the Fermi energy, then the intruder state can give rise to long-lived excited states called *isomers*.

2.3.1 Rotational Bands

A good indicator of deformation in nuclei is finding energy levels at a particular spacing. As an example, solving the Schrödinger equation for rotational modes of a deformed rigid-rotor system, we arrive at the energy levels,

$$E_J = \frac{\hbar^2}{2\mathcal{I}} J(J+1), \tag{2.9}$$

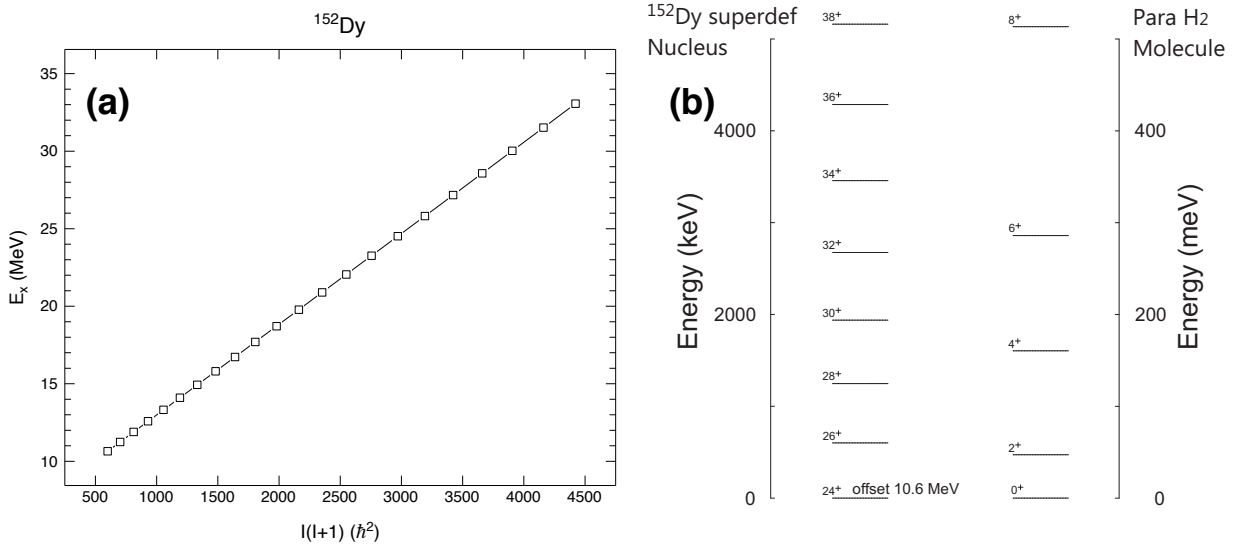

Figure 2.3: Panel (a) shows a plot of energy levels for ^{152}Dy as a function of $I(I+1)$. Panel (b) compares the rotational levels of ^{152}Dy to para-H_2. The $\Delta I = 2$ spacing between adjacent levels implies reflection symmetry in both cases. Courtesy Walter Reviol.

where $\mathcal{I}$ is the moment of intertia. A group of levels following this spacing are called a rotational band. For the diatomic case of H_2, the energy level spacings only approximate this form, and these states are presented in Fig. 2.3(b). An even better example of the this phenomenon arises in the nucleus ^{152}Dy, and a rotational band for this nucleus is shown in Fig. 2.3(a). In this figure, I represents the spin of the state. There are 22 energy levels that conform to the simple fixed moment of inertia rotation expectation, and by finding the slope of this curve information about the structure of the ^{152}Dy band head can be inferred. Finding such rotational bands are one clue to the deformed nature of mid-shell nuclei.

It is possible to have multiple rotation bands in heavier nuclei. These other rotational bands are typically headed by isomers, as they have significantly different structure (and thus moment of inertia) than the ground state. To confirm that the states are in fact a band head and to find their structure, one can measure the g-factors of the isomeric state and further excited states. Such measurements using the transient field method have been performed for isomers of lead isotopes [67, 68], as well as for isomers in other isotopes [69].

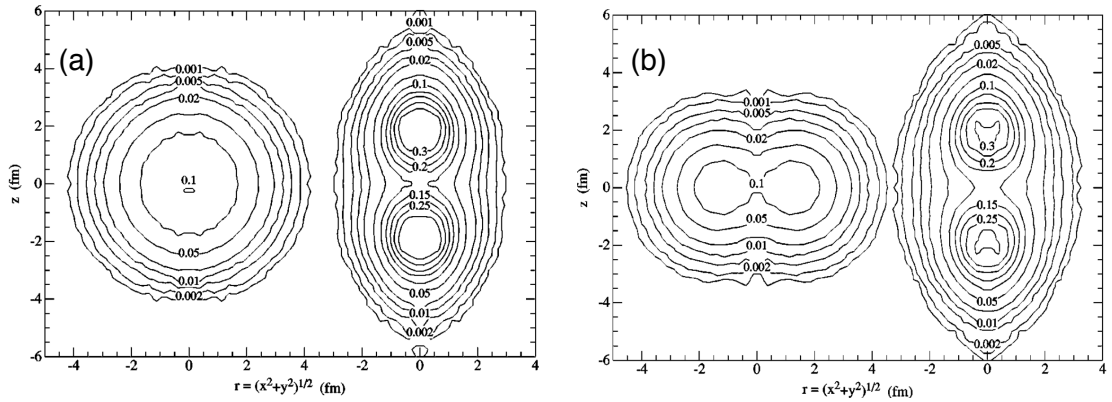

Figure 2.4: Figures 15 and 16 from Ref. [70]. (a) Plots of constant density from GFMC using the Argonne-V18+UIX (NN+3N) interactions for the ^{8}Be ground state in the laboratory frame (left) and in the intrinsic frame (right). Clear density profiles for the two α-particle cluster are seen in the intrinsic frame. (b) The same calculations but for the first $J^\pi = 4^+$ excited state of ^{8}Be.

In the case of the $J^\pi = 11^-$ isomer in ^{194}Pb and ^{196}Pb [68], the g-factors were found to be consistent with a 2-particle 2-hole excitation scheme in the Nilsson model, where two protons in the $3s_{1/2}$ shell are excited to $1h_{9/2}$ and $1i_{13/2}$ states in the presence of moderate oblate deformation.

2.3.2 Cluster Models

The clustering of α's in certain nuclei is a well accepted phenomenon in light nuclei. As mentioned before, this is due to the α nucleus having a very large binding energy per nucleon. It is common to see cluster structures just above the consituent particle decay threshold. One of the famous cases for cluster structure is ^{8}Be, where the ground state is 92 keV above the $\alpha - \alpha$ threshold. GFMC calculations of its ground state wave-function show two distinct α-clusters, shown in Fig. 2.4, and the first few excited states are well described as a rotational band built on this deformed structure, as GFMC methods also predict α clustering for the first $J^\pi = 4^+$ [70]. Another famous example is the Hoyle state in ^{12}C. This state is essential for the creation of ^{12}C in the nucleosynthetic pathway of stars, and ^{12}C serves as a seed for the synthesis of heavier elements. Three α's come together and live as an excited state of ^{12}C. Most of the time these fall back apart but a very small fraction of the time this state will γ-decay to the ground state, resulting in the ^{12}C that makes up

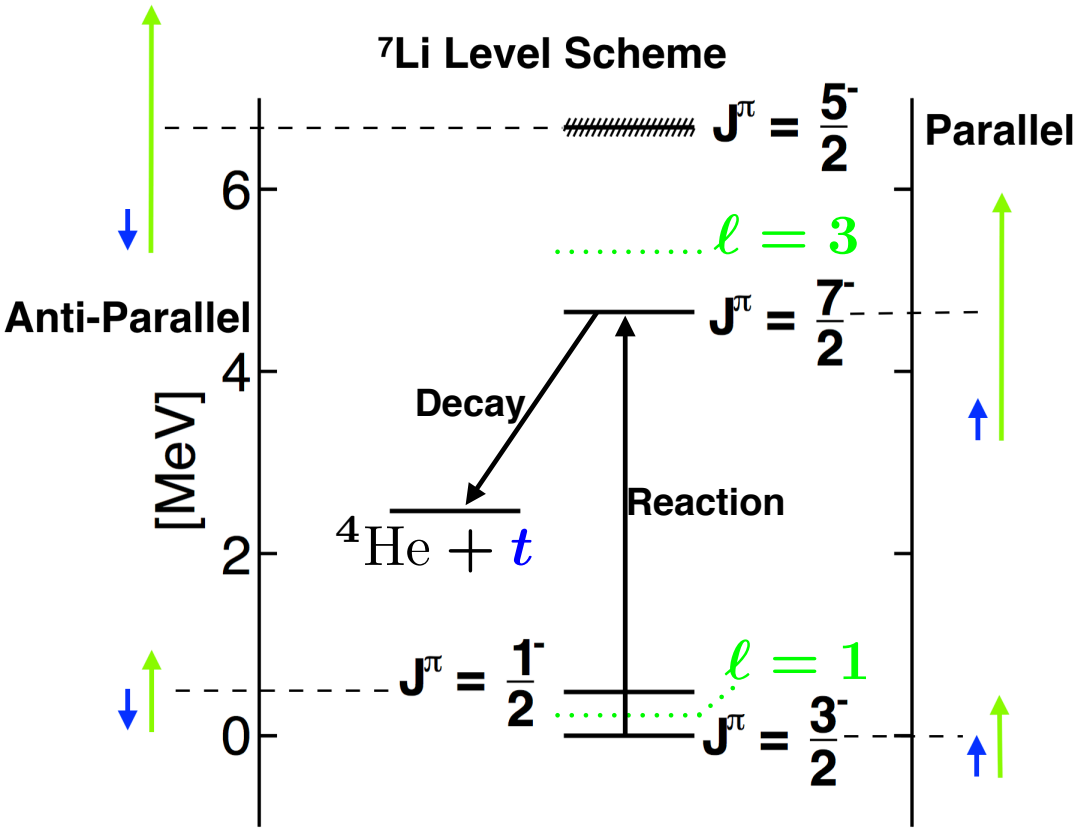

Figure 2.5: A level scheme of ^{7}Li highlighting its cluster structure. The green arrows represent the internal angular momentum between the $\alpha + t$ in ^{7}Li. The blue arrows show the orientation of the triton spin. The first few levels of ^{7}Li show the spin-orbit splitting from this cluster model. The internal orbital angular momentum of the pair is indicated by ℓ and the energy positions without spin-orbit coupling are indicated by the green dotted lines. The upward black arrow indicates the inelastic excitation induced in this work and the downward black arrow shows the subsequent decay used to report on the alignment of the $J^\pi = 7/2^-$ state.

all organic life and provides a seed to create heavier elements. Other examples of α-cluster nuclei include ^{6}Li, ^{7}Li, ^{7}Be, ^{8}Be, ^{9}Be, and ^{10}Be. The importance of clustering in heavier nuclei is hotly debated. However, the propensity of very heavy nuclei to undergo α decay strongly suggests clustering in the low density surface regions. Somewhere below 1/3 of the saturation density, nucleonic matter becomes unstable with respect to α-matter [71].

Treating these nuclei as clusters, when appropriate (i.e. states near the particle decay threshold), makes dynamical calculations much more tractable. In the case for the beam employed in the current study, treating ^{7}Li as a cluster of an $\alpha + t$ had several consequences. The ground state and first excited state are treated with $\ell = 1$ with a coupling to the

spin of the triton, s_t, parallel and anti-parallel respectively. The $J^\pi = 7/2^-$ at 4.6 MeV is then described with internal angular momentum $\ell = 3$. For the $7/2^-$ state we have $\ell \parallel s_t$. A summary of this first four excited states of ^{7}Li in this cluster model is shown in Fig. 2.5. When the $J^\pi = 7/2^-$ state falls apart into an $\alpha + t$ we can reasonably assume that the fragments carry a relative orbital angular momentum of $\ell = 3$. This significantly constrained fits to the angular correlations, that give the resulting magnetic substate. How these decay correlations are dictated by the magnetic substate populations will be discussed in the following chapter.

Chapter 3

Nuclear Reactions

> *"Although the problem of transmuting chemical elements into each other is much older than a satisfactory definition of the very concept of chemical element, it is well known that the first and most important step towards its solution was made only nineteen years ago by the late Lord Rutherford, who started the method of the nuclear bombardments."*
>
> —Enrico Fermi (1938)

The discovery of the nucleus is attributed to Rutherford after his "gold-foil" experiment, that involved collimating α radiation onto a thin Gold foil. Techniques for measuring radiation were very tedious at the turn of the 19^{th} century. The target and source were kept in a dark chamber lined with some scintillation material (zinc sulfide in the case of the "gold-foil" experiment) and the flashes of light around the chamber were counted by astute eyes. To the surprise of Geiger, Marsden, and Rutherford there were many large angle events, including events near the source (180^o scattering). They also observed a large fraction of α particles were unaffected by the presence of the foil, indicating there were large gaps between the scattering entities in the target material. This led to Rutherford's idea that the mass and charge of atoms were concentrated in a small region within the material (the nucleus).

Modern experiments have gone far beyond these initial nuclear bombardments. For

instance, with the advent of the Large Hadron Collider (LHC) it is common to perform proton-proton scattering at TeV energies. For studying the scattering of nuclei off each other there are many facilities around the world that provide stable beams and even radioactive beams (Texas A&M Cyclotron Institute, National Superconducting Cyclotron Laboratory, and ATLAS at Argonne National Laboratory to name a few). With these facilities, it is possible to perform many different nuclear reaction studies relevant for many fields.

There are many processes that are encompassed by nuclear reactions, including, but not limited to: transfer (of one or many nucleons relocated from the projectile to target or vice versa), knockout (of one or many nucleons from the projectile or target), fusion, projectile fragmentation, etc. The focus of this thesis is mainly on inelastic reactions, where one or both of the nuclei present are merely raised to an excited state and the N and Z of both are unchanged. Inelastic reactions are one of many direct reactions, which are generally peripheral collisions.

Scattering can be considered in a more general context than just between nuclei, and we can understand a great deal about scattering by starting from classical principles. As is the usual approach to describing quantum phenomena, we will extend the classical ideas into the quantum regime.

3.1 Cross Sections

An important quantity associated with scattering experiments is the cross section of the interaction, which gives the probability of a particle interacting with some other particle. In practice, this can be directly measured by looking at the loss in flux of beam passing through some material. If flux is lost in the beam, then the particle must have interacted with the material. This is the basis for many total cross section measurements of nuclei [72, 73, 74]. By measuring the probability of scattering as a function of scattering angle, we can determine what is called the differential cross section. The differential cross section (and other observables) are a powerful tool for understanding physical processes, highlighted by

Rutherford et al.'s great leap in understanding by observing "unusual" scattering phenomena. This is because the cross section is directly related to the physics of the interaction, so we can compare theoretical calculations of the cross section to experiment and learn about the underlying physical processes.

Starting from classical principles, suppose we measure the number of particles deflected into a certain small solid angle, $d\Omega$, and find $N(\theta, \phi)$ particles deflected per unit time with a constant beam flux of N_0 passing through a material of areal number density, ρ (particles/m^2). Then the probability of finding scattered particles in a particular solid angle, or differential cross section, is given by,

$$\frac{d\sigma}{d\Omega} = \frac{N(\theta, \phi)}{N_0 \rho}. \tag{3.1}$$

If we integrate the differential cross section over all solid angle we get the total probability of interaction within a given area, or σ,

$$\sigma = \int \frac{d\sigma}{d\Omega} d\Omega = \int_0^{2\pi} d\phi \int_0^{\pi} d\theta \frac{d\sigma}{d\Omega} \sin\theta, \tag{3.2}$$

and this is exactly the cross section. The angle of deflection can be mapped to an *impact parameter*, b, that characterizes the approach of the projectile to the target. A pictorial representation of b is shown in Fig. 3.1 for the case of Rutherford scattering. A number of particles going through a small area $N_0 b|db|d\phi$ will be directly mapped to the number of particles in a given solid angle,

$$\begin{aligned} d\sigma &= \frac{d\sigma}{d\Omega} \sin\theta d\theta d\phi = \frac{N_0 b|db|d\phi}{N_0} \Rightarrow \\ \frac{d\sigma}{d\Omega} &= \frac{b}{\sin\theta} \left| \frac{db}{d\theta} \right|. \end{aligned} \tag{3.3}$$

Once a mapping between the impact parameter and the scattering angle is found, for a specific scattering case, the whole classical problem can be solved.

3.1.1 Elastic Scattering off a Hard-Sphere

A nice example for Eq. (3.3) is to calculate the elastic scattering cross section for scattering off a hard-sphere. It turns out that the impact parameter as a function of scattering angle for a hard-sphere with radius R is,

$$b(\theta) = -R\cos(\theta/2) \Rightarrow \left|\frac{db}{d\theta}\right| = \frac{R}{2}\sin(\theta/2). \tag{3.4}$$

Plugging this into the classical formula for the cross section one obtains,

$$\begin{aligned}\sigma_{HS} = \int \frac{d\sigma}{d\Omega} d\Omega &= \int_0^{2\pi} d\phi \int_0^{\pi} d\theta(-R)\cos(\theta/2)\frac{R}{2}\sin(\theta/2) \\ &= 2\pi \int_0^{\pi} d\theta \frac{R^2}{4}\sin\theta = 4\pi\frac{R^2}{4} = \pi R^2.\end{aligned} \tag{3.5}$$

Not surprisingly the areal probability of interacting with the hard-sphere is just the cross-sectional area of the sphere, showing the origin of the term.

3.1.2 Rutherford Scattering

In the case of Rutherford scattering, only the Coulomb forces between the two nuclei are considered. As is the case in the previous problem, one needs a relationship between the impact parameter and the outgoing scattering angle. With each impact parameter there is an associated L for the collision angular momentum. This can be defined as $L = p_\infty b \Rightarrow b \overset{\mathbf{NR}}{=} L/(2mE)^{1/2}$, where p_∞ is the momentum of the incoming beam (far from scattering). From conservation of angular momentum and energy one can derive the relationship,

$$\theta = 2\arctan\left(\frac{Z_1 Z_2 e^2}{2Eb}\right) = 2\arctan\left(\frac{\alpha_C}{2Eb}\right). \tag{3.6}$$

Inverting the equation for θ we obtain the impact parameter as a function of scattering angle,

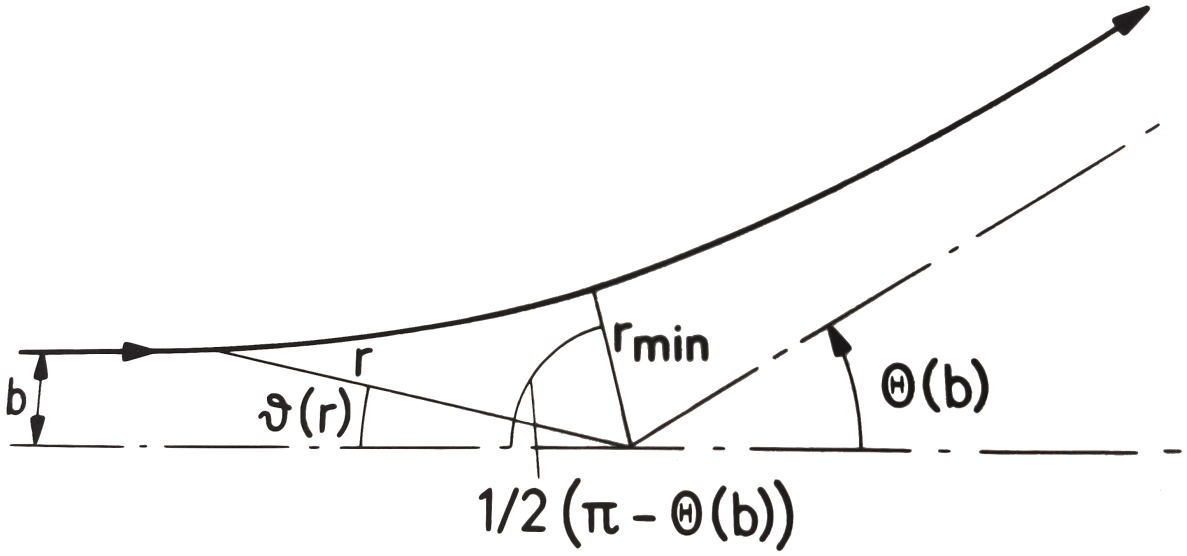

Figure 3.1: The definition of the impact parameter and the mapping to the deflection angle. From *Lecture Notes in Physics 51* by Nörenberg and Weidenmüller [75].

$$\begin{aligned} b &= \frac{\alpha_C}{2E}\cot(\theta/2) \Rightarrow \\ \frac{db}{d\theta} &= \frac{-\alpha_C}{4E}\csc^2(\theta/2). \end{aligned} \tag{3.7}$$

Plugging these into our forumula for the classical cross section we arrive at Rutherford's scattering forumula,

$$\left(\frac{d\sigma(E)}{d\Omega}\right)_{Ruth} = \frac{\alpha_C \cot(\theta/2)}{2E\sin(\theta)}\frac{\alpha_C}{4E\sin^2(\theta/2)} = \frac{\alpha_C^2}{4E^2\sin^4(\theta/2)}. \tag{3.8}$$

For nuclear reactions above the Coulomb barrier, deviations from Rutherford scattering are expected, especially at large scattering angles. Large scattering angles correspond to closer collisions, and thus nuclear forces start to come into play. A common parameter to characterize the deviation from Rutherford scattering is the grazing angle, θ_{gr}, corresponding to a particular L_{gr}. Provided that the bombarding energy is larger than the Coulomb barrier, the grazing angular momentum, L_{gr}, is defined by the formula,

$$L_{gr} = p_\infty R(1 - \frac{V_{CB}}{E_{\text{c.m.}}})^{1/2} = p_\infty b_{gr}, \tag{3.9}$$

where V_{CB} is the potential energy of the Coulomb barrier at $r_{\min}$ of Fig. 3.1 and R is a distance of closest approach that corresponds to a grazing collision. If the two nuclei have mass A_1 and A_2, and remembering that the size of a nucleus goes approximately by $A^{1/3}$ or $r \approx 1.2A^{1/3}$ fm, then in a touching spheres approximation, $R \approx 1.2(A_1^{1/3} + A_2^{1/3})$. To relate this to θ_{gr} the Sommerfield parameter is defined,

$$\eta = \frac{Z_1 Z_2 e^2}{4\pi\epsilon_0 \hbar v}. \tag{3.10}$$

Then as Nörenberg and Weidenmüller show [75],

$$\theta_{gr} = 2\arctan(\eta\hbar/L_{gr}). \tag{3.11}$$

Below the grazing angle, the resulting scattering will be similar to Rutherford scattering. Scattering angles larger than the grazing angle correspond to smaller impact parameters. At low enough bombarding energies the de Broglie wavelength of the projectile becomes commensurate with the size of the impact parameter and thus a full quantum-mechanical formalism is needed.

3.2 Quantum-Mechanical Scattering Theory

Taking these ideas into the quantum realm, let's start with the Hamiltonian,

$$H = T + V = H_0 + V. \tag{3.12}$$

The original eigenfunctions are that of the free particle hamiltonian, $|\phi_{\mathbf{k}}\rangle$. In this formalism it is assumed that V is a real potential. Complex potentials will be introduced later to model loss of flux from the beam (i.e. reactions). Writing down the Schrödinger equation as what

is called the Lippmann-Schwinger equation, the wavefunction is given by,

$$|\psi_{\mathbf{k}}\rangle = |\phi_{\mathbf{k}}\rangle + \frac{1}{E(\mathbf{k}) - H_0 + i\epsilon} V |\psi_{\mathbf{k}}\rangle \,. \tag{3.13}$$

The fractional term is called the free particle propagator (it is effectively a different representation of the Green's function) and it's implied that $\lim_{\epsilon \to 0}$ after evaluation. In this representation $E(\mathbf{k}) = \hbar^2 k^2 / 2\mu$, with μ as the reduced mass of the system. The scattered states are then represented by $|\psi_{\mathbf{k}}\rangle$. Projecting $\langle \phi_{\mathbf{r}}|$ onto Schrödinger's equation,

$$\begin{aligned} \langle \phi_{\mathbf{r}} \mid \psi_{\mathbf{k}} \rangle &= \langle \phi_{\mathbf{r}} \mid \phi_{\mathbf{k}} \rangle + \langle \phi_{\mathbf{r}}| \frac{1}{E(\mathbf{k}) - H_0 + i\epsilon} V |\psi_{\mathbf{k}}\rangle \\ \Psi_{\mathbf{k}}(\mathbf{r}) &= \frac{1}{(2\pi\hbar)^{3/2}} e^{i\mathbf{k}\cdot\mathbf{r}} + \int d^3\mathbf{r}' \, \langle \phi_{\mathbf{r}}| \frac{1}{E(\mathbf{k}) - H_0 + i\epsilon} |\phi_{\mathbf{r}'}\rangle \langle \phi_{\mathbf{r}'}| V |\psi_{\mathbf{k}}\rangle \,, \end{aligned} \tag{3.14}$$

where the completeness of the states $|\phi_{\mathbf{r}}\rangle$ has been employed in the last line, and $\Psi_{\mathbf{k}}(\mathbf{r})$ is just the standard wavefunction in the position basis. The matrix elements of the propagator can be evaluated in the complex plane giving the result,

$$\lim_{\epsilon \to 0} \langle \phi_{\mathbf{r}'}| \frac{1}{E(\mathbf{k}) - H_0 + i\epsilon} |\phi_{\mathbf{r}}\rangle = \frac{-\mu}{2\pi\hbar^2} \frac{e^{ik|\mathbf{r}-\mathbf{r}'|}}{|\mathbf{r}-\mathbf{r}'|}. \tag{3.15}$$

Using the far field limit (i.e. the measurement will take place far from the interaction distance),

$$\begin{aligned} \lim_{\mathbf{r} \to 0} \frac{1}{|\mathbf{r}-\mathbf{r}'|} &= \frac{1}{r}, \\ k|\mathbf{r}-\mathbf{r}'| &\cong kr - \mathbf{k}\cdot\mathbf{r}'. \end{aligned} \tag{3.16}$$

Putting these all together one obtains,

$$\begin{aligned}\Psi_{\mathbf{k}}(\mathbf{r}) &= \frac{1}{(2\pi\hbar)^{3/2}}\left[e^{i\mathbf{k}\cdot\mathbf{r}} + \frac{e^{ikr}}{r}\frac{-\mu}{(2\pi\hbar)^{1/2}}\int d^3\mathbf{r}' e^{-i\mathbf{k}\cdot\mathbf{r}'}V(\mathbf{r}')\Psi_{\mathbf{k}}(\mathbf{r}')\right] \\ &= \frac{1}{(2\pi\hbar)^{3/2}}\left[e^{i\mathbf{k}\cdot\mathbf{r}} + f(k,\theta)\frac{e^{ikr}}{r}\right].\end{aligned} \tag{3.17}$$

The quantity $f(k,\theta)$ is known as the *scattering amplitude* of the resulting spherical wave (that interferes with the initial plane-wave), and is related to the elastic differential cross section by,

$$|f(k,\theta)|^2 = \frac{d\sigma}{d\Omega}. \tag{3.18}$$

In the case of classical scattering theory, all that is needed to solve the scattering problem is the equation for $b(\theta)$. In the quantum mechanical case, the problem is completely solved if one finds an equation for $f(k,\theta)$. The connection between the differential cross section and the scattering amplitude can perhaps be elucidated with the question; If we have a free particle with plane-wave solutions (send in a beam of particles), what is the probability of scattering (lost from the beam to other angles) if we add a scattering potential (throw a slab of material in front of it) and how does that vary as a function of angle and energy (where I put my detector and the my selection of beam energy)? The scattering amplitude is *what's different* between the plane-wave and full solution with the scattering material.

It is also important to introduce the transition amplitude, or T matrix, which is used to describe the transition from initial to final scattering states. Looking at equation Eq. (3.17), the transition amplitude is the integral that incorporates the potential, which can be written in the Dirac form (by completeness of the states $|\phi_{\mathbf{r}}\rangle$),

$$T_{i,f} = \langle\Psi_{\mathbf{k}}|\, V\, |\phi_{\mathbf{k}}\rangle\,. \tag{3.19}$$

The *Born approximation* is now introduced, which treats the scattering potential as a per-

turbation. In this case, first order perturbation theory tells us that the main contribution to the transition amplitude will be,

$$T_{i,f}^{BA} = \langle \phi_{\mathbf{k}'} | \, V \, | \phi_{\mathbf{k}} \rangle \, , \tag{3.20}$$

as the unperturbed solutions to the Schrödinger equation are used in place of the full solutions.

3.2.1 Partial Wave Analysis

In order to solve the final wavefunction numerically, and to gain insight into the calculations, it is useful to do a partial wave analysis of the final wavefunction. Focusing on the the radial portion of the Schrödinger equation in spherical coordinates,

$$\frac{-\hbar^2}{2\mu r}\frac{d^2}{dr^2}(rR_L(r)) + \frac{\hbar^2 L(L+1)}{2\mu r^2}R_L(r) + (V-E)R_L(r) = 0. \tag{3.21}$$

Here $R_L(r)$ are the radial components to our wavefunction $\Psi_{\mathbf{k}}(\mathbf{r})$. Our goal is to compare the asymptotic limits of $\Psi_{\mathbf{k}}(\mathbf{r})$ and $\phi_{\mathbf{k}}(\mathbf{r})$ and use Eq. (3.17) to solve for $f(k,\theta)$. Since the distances in the lab ($\sim$ m) are much greater than the interaction distance ($\sim$ fm) the asymptotic limits of the wavefunctions will ultimately be what are measured.

A plane-wave can be represented as a sum of spherical waves, otherwise known as the plane-wave expansion, and so for our unperturbed eigenfunctions,

$$\phi_{\mathbf{k}}(\mathbf{r}) = \frac{e^{i\mathbf{k}\cdot\mathbf{r}}}{(2\pi\hbar)^{3/2}} = \sum_{L=0}^{\infty}(2L+1)i^L j_L(kr)P_L(\hat{\mathbf{k}}\cdot\hat{\mathbf{r}}), \tag{3.22}$$

where j_L is a spherical Bessel function, and P_L is a Legendre polynomial. The spherical Bessel functions are the spherical wave solutions for the free-particle wave equation. The asymptotic limits of the spherical Bessel function is,

$$\lim_{\rho\to\infty} j_L(\rho) = \frac{1}{\rho}\sin(\rho - \pi L/2). \tag{3.23}$$

The perturbed wavefunction is a solution to the inhomogeneous partial differential wave equation (3.14). The general solution to this equation in the asymptotic limit is a linear combination of spherical Henkel functions, h_L. Thus one can write,

$$\begin{aligned}\lim_{r\to\infty} R_L(r) &= e^{2i\delta_L} h_L + h_L^* \\ &= \frac{1}{2ikr}\left(e^{2i\delta_L} e^{i(kr-L\pi/2)} - e^{-i(kr-L\pi/2)}\right). \\ &= \frac{e^{i\delta_L}}{kr}\sin(kr+\delta_L - \pi L/2).\end{aligned} \tag{3.24}$$

The first term in the first line is the outgoing spherical wave, and after scattering it picks up a *phase shift*, δ_L, after passing through the potential (hence they are a function of the scattering potential). The second term in the first line represents the incoming spherical wave in the partial-wave expansion, and so it has a coeffecient of 1, preserving probability because V is a real potential. Since these solutions are also spherical wave solutions one can perform a partial-wave expansion of $\Psi_{\mathbf{k}}(\mathbf{r})$,

$$\Psi_{\mathbf{k}}(\mathbf{r}) = \sum_{L=0}^{\infty}(2L+1)i^L R_L(r) P_L(\hat{\mathbf{k}}\cdot\hat{\mathbf{r}}). \tag{3.25}$$

By comparing the partial wave expansions of the plane-wave and full solutions using the asymptotic limits given Eqs. (3.23) and (3.24), one can derive a relationship for the scattering amplitude in terms of the phase shifts,

$$f(k,\theta) = \frac{1}{k}\sum_{L=0}^{\infty}(2L+1)e^{i\delta_L}\sin(\delta_L)P_L(\hat{\mathbf{k}}\cdot\hat{\mathbf{r}}). \tag{3.26}$$

With the definition $f_L(k) = e^{i\delta_L}\sin\delta_L/k = (e^{2i\delta_L}-1)/2ik$ this previous equation can be written rather succinctly as,

$$f(k,\theta) = \sum_{L=0}^{\infty}(2L+1)f_l(k)P_L(\hat{\mathbf{k}}\cdot\hat{\mathbf{r}}). \tag{3.27}$$

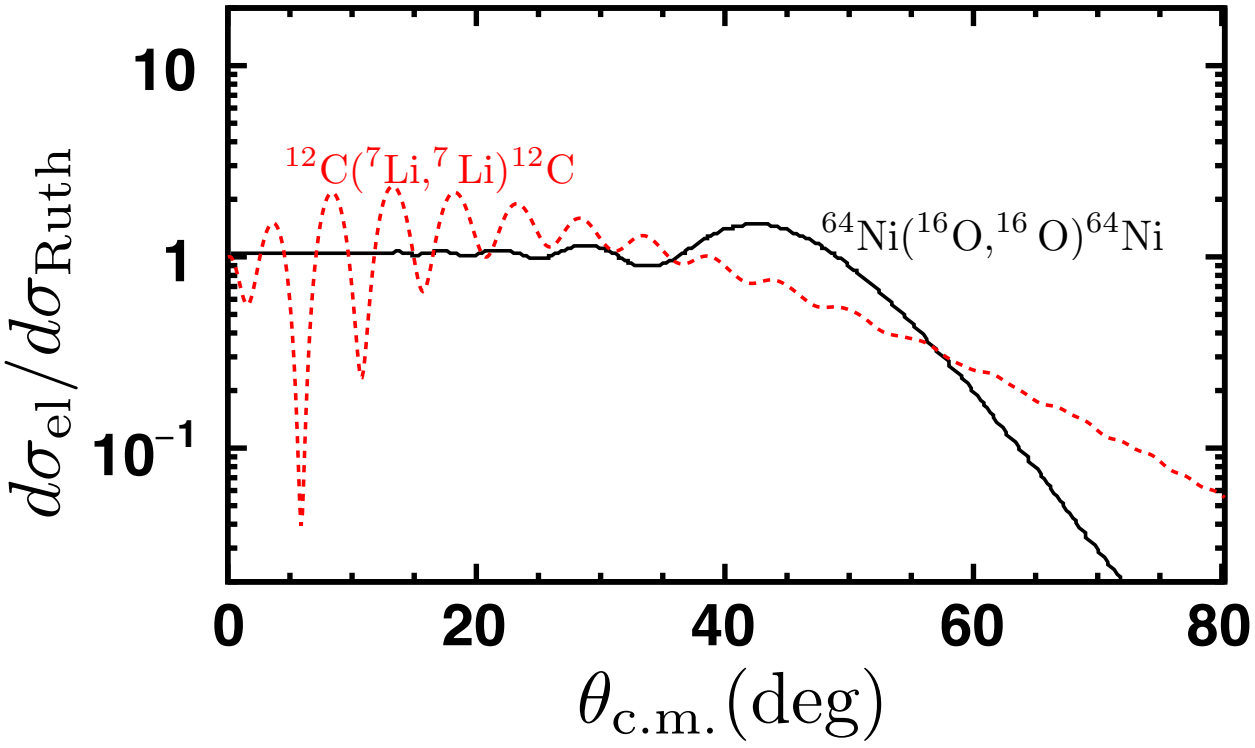

Figure 3.2: An optical-model calculation of elastic scattering of $E = 60$ MeV ^{16}O off ^{64}Ni (black solid line). For small angles, the scattering is approximately Rutherford scattering due to low relative kinetic energy and high charge and mass. The solid red line shows a DWBA calculation of $E = 168$ MeV ^{7}Li scattering off ^{12}C. For less massive and less charged systems, the deviations from Rutherford scattering are more prominent at small scattering angles. Both of these calculations were performed with FRESCO [76].

3.2.2 Distorted Wave Born Approximation

The scattering theory presented above provided the full solutions to the Schrödinger equation for neutrally charged particles (ignoring Coulomb forces) and also introduced the *Born approximation*, which designates that the unperturbed solutions to the Schrödinger equation are plane waves. The full solutions to Eq. (3.17) are often call *distorted waves*. If one used the Coulomb potential and Woods-Saxon potentials with spin-orbit coupling as the scattering potential, the partial wave analysis of the previous section can be applied to

obtain the wavefunctions,

$$\chi_{\mathbf{k}}(\mathbf{r}) = \sum_{L} i^{L} e^{i\sigma_{k,L}} R_L(r) P_L(\hat{\mathbf{k}} \cdot \hat{\mathbf{r}}), \tag{3.28}$$

where now $R_L(r)$ are solutions to the radial Schrödinger equation, and the factors $\sigma_{k,L}$ represent the corresponding phase shifts associated with the distorting potential. In order to capture more of the physics, the distorted-wave Born approximation (DWBA) was introduced, which uses the full solutions to some auxiliary potential as the unperturbed solutions to the Hamiltonian. There are many in depth textbooks and papers on the use of DWBA theory for direct reactions [77, 78], and this theory has been applied to many different types of reactions. There are a handful of computer programs that handle nuclear scattering using DWBA. Two common programs are DWUCK and FRESCO. Fig 3.2 shows a calculation using the code FRESCO for the elastic cross section in the ^{7}Li+^{12}C system of interest, as well as the elastic cross section for a heavier system, ^{16}O + ^{64}Ni.

For most purposes the Coulomb potential and Woods-Saxon potentials with spin-orbit coupling are used as the auxiliary potential in DWBA calculations. Typically the auxiliary potentials are chosen such that they reproduce elastic scattering data (i.e. are fit to data). Using these potentials, and the scattering solutions in Eq. (3.28), one can extend the formulation of the T matrix to the DWBA case where,

$$T_{i,f}^{DWBA} = \langle \chi_{\mathbf{k}_f} | \, V \, | \chi^{*}_{\mathbf{k}_i} \rangle \, . \tag{3.29}$$

This equation will be extremely useful for later analysis, as the T matrix can be specified for any initial or final scattering state, including those for specific magnetic substates. This particular formalism of the T matrix will be used later to specify the final magnetic substate distributions of the resulting nucleus, elucidating how spin alignment can be generated in nuclear reactions.

3.2.3 Optical Models

The discussion on quantum-mechanical scattering theory used the fact that V is a real potential. When we are working with a real potential then all of the scattering, by definition, must be elastic. Using the formalism above, and introducing the scattering matrix element, $S_L = e^{2i\delta_L}$, the total elastic cross section can be written as,

$$\begin{aligned}\sigma_{elastic} &= \int d\Omega \frac{d\sigma}{d\Omega} = \int d\Omega |f(k,\theta)|^2 \\ &= \frac{\pi}{k^2}\sum_{L=0}^{\infty}(2L+1)|S_L - 1|^2 \\ &= \frac{\pi}{k^2}\sum_{L=0}^{\infty}(2L+1)(|S_L|^2 - 2\Re[S_L] + 1),\end{aligned} \tag{3.30}$$

where in this equation the fact that $\int d\Omega P_L(\hat{\mathbf{k}}\cdot\hat{\mathbf{r}})P_{L'}(\hat{\mathbf{k}}\cdot\hat{\mathbf{r}}) = \frac{4\pi}{2L+1}\delta_{L,L'}$ has been used.

By conservation of the probabilities, one can derive what is called the *Optical Theorem*[†], which relates the total cross section to the imaginary component of the scattering amplitude at zero scattering angle. This is mathematically described by,

$$\sigma_{tot} = \frac{4\pi}{k}\Im[f(k,\theta=0)] = \frac{2\pi}{k^2}\sum_{L=0}^{\infty}(2L+1)(1-\Re[S_L]). \tag{3.31}$$

where the imaginary scattering amplitude at zero angle corresponds to *flux being lost from the beam*. If the scattering potential is real then $|S_L| = 1$ and the elastic cross section is exactly equal to total cross section. Introducing complex scattering potentials is rather straightforward, but all of the quantities become complex, in particular the phase shifts and the scattering matrix elements. Therefore one can obtain $|S_L| < 1$, and the difference from unity takes into account non-elastic channels. The total reaction cross section can then be defined as the difference between the total cross section and the elastic scattering cross

[†]A history of the optical theorem and its use in quantum mechanics is presented in Ref. [79].

section,

$$\begin{aligned}\sigma_{Rx} &= \sigma_{tot} - \sigma_{elas} \\ &= \frac{\pi}{k^2}\sum_{L=0}^{\infty}(2L+1)(2 - 2\Re[S_L] - |S_L|^2 + 2\Re[S_L] - 1) \\ &= \frac{\pi}{k^2}\sum_{L=0}^{\infty}(2L+1)(1 - |S_L|^2).\end{aligned} \tag{3.32}$$

The use of complex potentials to model losses in a material is not only of use in nuclear scattering. As the name "Optical Model" suggests, these ideas were originally used to describe absorption processes of light in a medium. A rather simple example of this is modeling dielectrics. By introducing an imaginary part to the dielectric constant, the imaginary component corresponds to losses of light in the material (that turn into heat).

The typical form of the potentials used for optical models is the same as those used for nuclear structure, Woods-Saxon potentials. The main term of the potential is typically called the *volume* term. In addition to the the volume potential other terms can be added (e.g. spin-orbit coupling and surface absorption).

Because these potentials are phenomenological, the parameters are often opened to a fit of the elastic scattering angular distributions and/or other observables. If one focuses on a particular reaction, a reasonable set of parameters can usually be found that describes that reaction well. However, these parameters are expected to have an energy dependence and also differ for each reaction. What this means is that finding a global set of optical-potential parameters, or even a function connecting the parameters for different scattering partners, is a daunting task.

Taking further ideas from optical theories, there is an extension of the regular optical model, that was mentioned before, called the Dispersive Optical Model (DOM) which applies dispersive corrections to the optical model through many-body theory dispersive relations (similar to the Kramers-Konig relations) that enforce causality. This is a powerful relation

for connecting structure (real components) to reaction calculations (imaginary components). At the moment, only nuclei near closed shells can be calculated effectively (a closed-shell nucleus can be used as a "core" for the calculations). As a result, most of the experimental data used to fit the potential comes from experiments involving such nuclei, including ^{40,48}Ca, and ^{208}Pb, to name a few. Of particular interest, are neutron total cross sections, and many experiments have been done measuring these cross sections with the object of fitting the DOM, which is then used to extract interesting properties of nuclei [74, 80, 81, 82].

3.2.4 Characterizing Reactions

In the quantum mechanical formalism, the impact parameters are not as well-defined as in the classical case. What this means, is that many impact parameters or L waves contribute to scattering at any given angle. To understand the relationship between different L waves and the particular process of interest, the total reaction cross section for a nuclear reaction can be decomposed into contributions from different L's, and thus different impact parameters. This partial-wave decomposition can be defined from Eq. (3.32),

$$\begin{aligned}\sigma_{Rx}(E_{\text{c.m.}}) &= \pi\lambda\!\!\!^{-2}\sum_{L=0}^{\infty}(2L+1)T_L(E_{\text{c.m.}}) \\ &= \sum_{L=0}^{\infty}\sigma_L(E_{\text{c.m.}}),\end{aligned} \tag{3.33}$$

where $\lambda\!\!\!^{-}$ is the de Broglie wavelength ($1/k^2 = \lambda\!\!\!^{-2}$), and T_L is the transmission coefficient. By inspection one can see that T_L is related to the scattering matrix element, S_L, by,

$$T_L = 1 - |S_L|^2. \tag{3.34}$$

The effective radius of the projectile is given by $\lambda\!\!\!^{-}$, and so its area is $\pi\lambda\!\!\!^{-2}$. As the impact parameter is increased, the available area for a reaction increases, i.e. the cross section, and

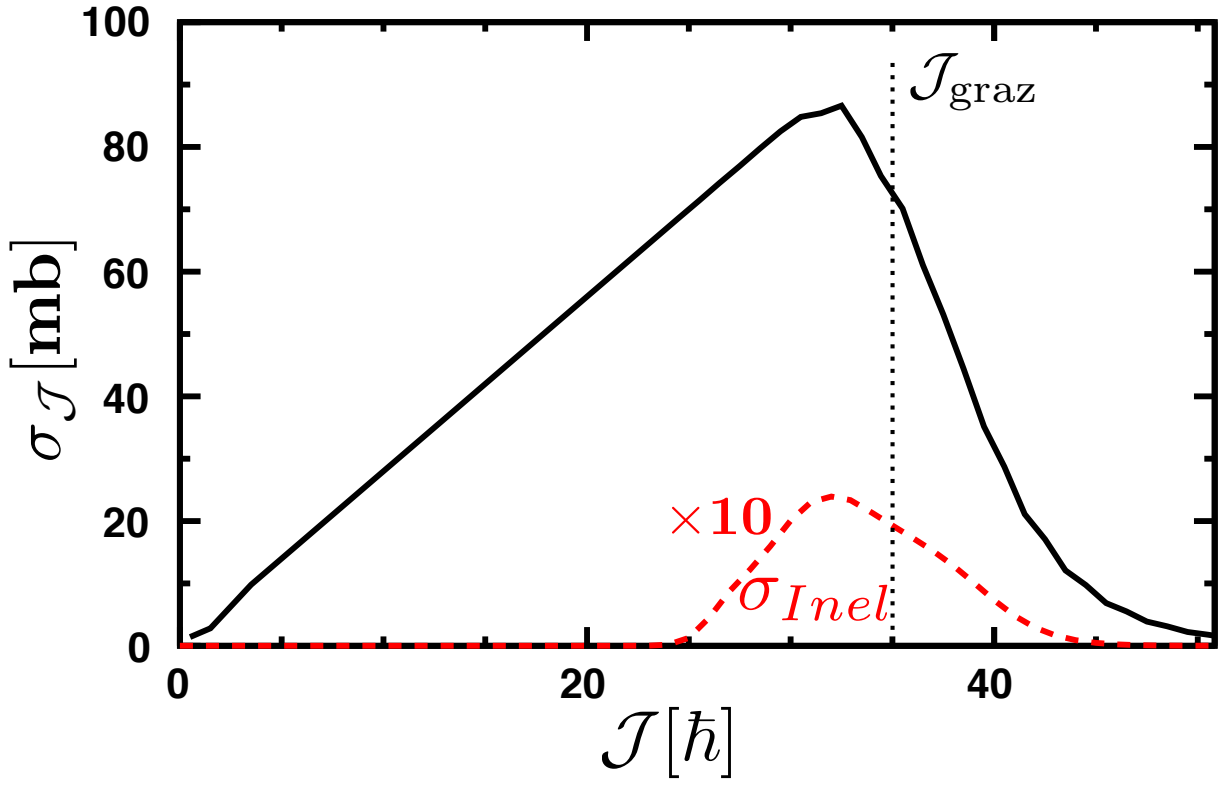

Figure 3.3: The solid black line shows the partial-wave contributions to the total reaction cross section for the ^{7}Li + ^{12}C system at $E/A = 24$ MeV as a function $\mathcal{J}$. The dashed red line shows the partial-wave contribution for the inelastic excitation of ^{7}Li to the 4.63 MeV state, while the target remains in its ground state. This inelastic cross section has been scaled up a factor of 10 for display.

this is represented by the factor $(2L + 1)$. In fact this description is what gives rise to the pattern described in the Introduction and shown in Fig. 1.6. Once a scattering potential has been defined for the reaction (e.g. from the optical model) one can derive the partial cross section decomposition, σ_L, and even the cross section for a particular process using Eq. (3.33).

Figure 3.3 shows a decomposition of the total reaction cross section $E = 24$ MeV/A ^{7}Li projectiles on a ^{12}C target from FRESCO DWBA scattering calculations (black solid line) in the $\mathcal{J}$ basis, where $\boldsymbol{\mathcal{J}} = \mathbf{L} + \mathbf{J}_{\rm proj}$ (changing this basis requires a transformation using the relevant Clebsch-Gordan coefficients). As the nuclei involved are lighter, the portion of the total reaction cross section corresponding to small impact parameters will involve fusion

and massive breakup reactions. If the nuclei were much larger, then the region between the critical and grazing impact parameters would correspond to deep inelastic reactions. Above L_{graz}, or $\mathcal{J}_{\text{graz}}$ in Fig. 3.3, the transmission coefficient drops steeply to zero. The region underneath the defined peak corresponds to peripheral collisions, giving rise to direct reactions. As mentioned before, inelastic reactions fall into this category, and the predicted partial cross section for the reaction of interest is shown as the red dashed line in Fig. 3.3. This curve has been scaled by a factor of 10 for comparison to the total cross section. As can be seen, the particular reaction of interest in this work takes up a small portion of the total reaction cross section. Other processes will contribute to the total cross section in this region, including transfer and nucleon knockout. Such reactions were also observed during the experiment involving ^{7}Li, and these processes will be highlighted in Chapter 5.

3.3 Angular Correlations for Sequential Decays

Once a particular state has been formed, it can decay by several methods. The dominant methods of decay in nuclear regimes is γ decay and particle emission or breakup. The way the nucleus decays can give us information about the initial state that was formed. If the decay happens sufficiently far away from the scattering event, then it can be treated as a sequential decay process. In practice, this means the reaction is described by two successive 2-body processes (e.g. the formation of ^{7}Li* and the decay of ^{7}Li*). For the case of the sequential breakup of ^{7}Li* in the inelastic reaction of interest, this is an appropriate assumption as the lifetime of the state ($\sim 10^{-21}$ s) and the particular beam energy means ^{7}Li* will travel a mean distance of ~ 200 fm from the point of interaction before decaying into an $\alpha + t$.

For the following presentation, the work of Strazzeri is followed [83]. Provided with unpolarized initial states (and thus summing over all the spin degrees of freedom), the double differential cross section for a sequential decay process, a+X $\rightarrow$ b+Y $\rightarrow$ b +c+Z, can be written in a form that separates the processes,

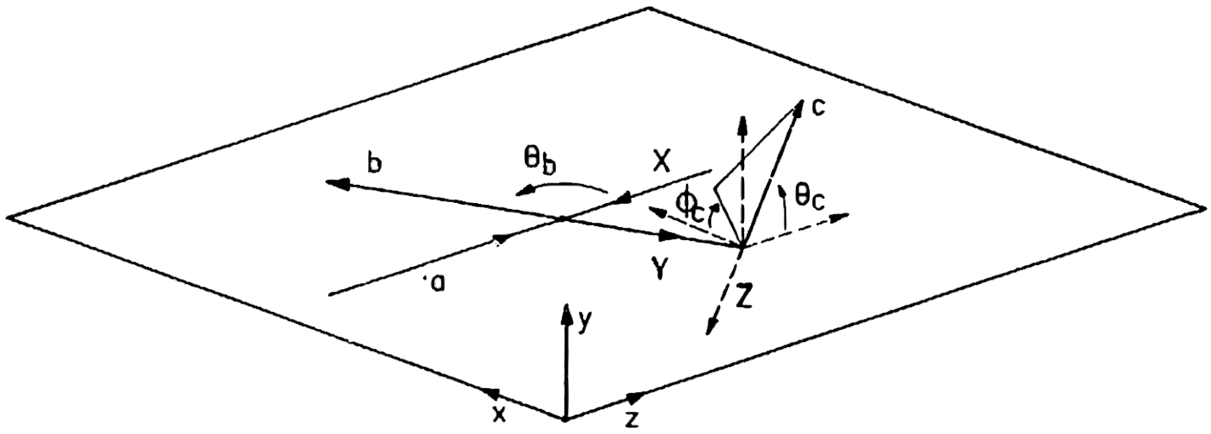

Figure 3.4: Figure 1 from Ref. [83], showing the angle definitions of the sequential decay process using the beam axis as the z axis, which is also the quantization axis.

$$\begin{aligned}\frac{d^2\sigma}{d\Omega_b d\Omega_c} \propto & \sum_{m_p,m_t,m_{p*},m_{t*},m_c,m_Z} |\sum_{m_Y} T^{m_p,m_t,m_{p*},m_{t*},m_c,m_Z}(\theta_b, E_{\text{c.m.}}) \\ & \times \sum_{l_c,J'} \langle l_c m_{l_c}; J', m_Y - m_{J'} | J_Y m_Y \rangle S^{J_Y}_{s_c,s_Z}(E_{\text{decay}}) \\ & \times \langle J_Z m_Z; s_c, m_c | J', m_c + m_Z \rangle Y^{l_c}_{m_Y - m_{J'}}(\theta_c, \phi_c)|^2 \end{aligned} \tag{3.35}$$

where there are sums over the many different spin degrees of freedom, and the T refers to the T matrix for the particular reaction of interest, which specifies the populated magnetic substates in the reaction. l_c denotes orbital motion of the decay, and the factor S describes the decay process (for example, one could use the R-Matrix formalism [84] for branching ratios). The definitions of the different angles are given in Fig. 3.4, and it should be noted that the notation for spherical harmonics, Y^L_M, is used here. For the following equations, the degrees of freedom in the first sum will be denoted by the index, i.

If only processes where $s_Z = 0$ are considered and there is only one angular momentum in the decay (both of these conditions are satisfied for the ^{7}Li case), then the equation simplifies considerably and one can write,

$$\begin{aligned}\frac{d^2\sigma}{d\Omega_b d\Omega_c} &\propto \sum_i |\sum_{m_Y,m_c} T^i_{m_Y}(\theta_b, E_{\text{c.m.}})\langle l_c, m_{l_c}; s_c, m_c | J_Y, m_Y\rangle Y^{l_c}_{m_Y - m_c}(\theta_c,\phi_c)|^2 \\ \frac{d^2\sigma}{d\Omega_b d\Omega_c} &\propto \sum_i |\sum_{m_{l_c}} T^i_{m_{l_c}}(\theta_b, E_{\text{c.m.}}) Y^{l_c}_{m_{l_c}}(\theta_c,\phi_c)|^2.\end{aligned} \tag{3.36}$$

In the last line of Eq. 3.36, the fact that we can transform to the l_c basis by,

$$\sum_{m_{l_c}} T^i_{m_{l_c}} = \sum_{m_Y,m_c} T^i_{m_Y = m_{l_c}+m_c}\langle l_c, m_{l_c}; s_c, m_c | J_Y, m_Y\rangle, \tag{3.37}$$

has been used. The resutling T matrix determines the population of particular magnetic substates of l_c (the decay orbital angular momentum), and so these population parameters can be written as the matrix C by,

$$C_{m_{l_c}, m'_{l_c}} = \sum_i T^i_{m_{l_c}} [T^i_{m'_{l_c}}]^*, \tag{3.38}$$

The coefficients $C_{m_{l_c},m'_{l_c}}$ are related to the density matrix of the decay orbital angular momentum, $\rho^{l_c}_{m_1,m_2}$, by normalizing the parameters by the trace of the C matrix [77]. With the provided formalism, one can follow the analysis in Ref. [48], which separates out the diagonal and off-diagonal values of the density matrix for the population of internal orbital momentum eigenstates. Using the decomposition of spherical harmonics into Wigner's little-d matrix,

$$Y^l_m(\psi,\chi) = (-1)^m \sqrt{\frac{2l+1}{4\pi}} d^l_{m,0}(\psi) e^{im\chi}, \tag{3.39}$$

and Wigner's little-d matrix is,

$$d^l_{m,0} = \sqrt{\frac{(l-m)!}{(l+m)!}} P^l_m(\cos\psi). \tag{3.40}$$

This ultimately gives us the equation (removing the subscript c for the orbital motion of the decay),

$$\frac{d^2\sigma}{d\Omega d\Omega} \propto C_{0,0}(\theta_b)|d^l_{0,0}(\theta_c)|^2 + 2\sum_{m_l=1}^{l}|d^l_{m,0}(\theta_c)|^2(C_{m_l,m_l}(\theta_b) + (-1)^{m_l}C_{m_l,-m_l}(\theta_b)\cos(2m_l\phi_c))$$
$$+4\sum_{\substack{1\le m_1\le l\\ -m_1<m_2<m_1}} Re\left[C_{m_1,m_2}(\theta_b)\right](-1)^{m_1+m_2}d^l_{m_1,0}d^l_{m_2,0}\cos((m_1-m_2)\phi_c). \tag{3.41}$$

Using this equation, the measured angular correlations are fit to the parameters C_{m_1,m_2} in order to obtain the population of different magnetic substates of the orbital decay motion. This can be simplified further, by projecting onto θ_c and all of the interference terms drop out, giving the equation,

$$W(\theta_c) \propto \rho^l_{0,0}(\theta_b) + 2\sum_{m_l=1}^{l}\rho^l_{m_l,m_l}(\theta_b)|d^l_{m,0}(\theta_c)|^2. \tag{3.42}$$

In the case of ^{7}Li* [4.63 MeV], $l = 3$ and $J_Y = 7/2$, and one can couple back the 1/2 spin of the triton to obtain the magnetic substate population of the excited nucleus defined by the density matrix $\rho^J_{m,m'}$. With these constraints on the nucleus, Eqs. (3.37) and (3.38) are used to obtain a set of linear equations between $\rho^l_{m,m'}$ and $\rho^J_{m,m'}$,

$$\begin{aligned}
\rho^{l=3}_{3,3} &= \langle 3,3\,;1/2,1/2\,|\,7/2,7/2\rangle^2\,\rho^{J=7/2}_{\frac{7}{2},\frac{7}{2}} + \langle 3,3\,;1/2,-1/2\,|\,7/2,5/2\rangle\,\rho^{7/2}_{\frac{5}{2},\frac{5}{2}}\\
\rho^{l=3}_{2,2} &= \langle 3,2\,;1/2,1/2\,|\,7/2,5/2\rangle^2\,\rho^{J=7/2}_{\frac{5}{2},\frac{5}{2}} + \langle 3,2\,;1/2,-1/2\,|\,7/2,3/2\rangle\,\rho^{7/2}_{\frac{3}{2},\frac{3}{2}}\\
\rho^{l=3}_{1,1} &= \langle 3,1\,;1/2,1/2\,|\,7/2,3/2\rangle^2\,\rho^{J=7/2}_{\frac{3}{2},\frac{3}{2}} + \langle 3,1\,;1/2,-1/2\,|\,7/2,1/2\rangle\,\rho^{7/2}_{\frac{1}{2},\frac{1}{2}}\\
\rho^{l=3}_{0,0} &= \langle 3,0\,;1/2,1/2\,|\,7/2,1/2\rangle^2\,\rho^{J=7/2}_{\frac{1}{2},\frac{1}{2}} + \langle 3,0\,;1/2,-1/2\,|\,7/2,-1/2\rangle^2\,\rho^{7/2}_{-\frac{1}{2},-\frac{1}{2}}.
\end{aligned} \tag{3.43}$$

In Eq. (3.43), the left-hand side are the observables of the experiment, and by back substitution the density matrix parameters of the inelastically excited state can be inferred.

Chapter 4

Experiment

"We are not to tell nature what she's gotta be. ... She's always got a better imagination than we have."

—Richard Feynman

In order to determine the population of excited states in ^{7}Li, the momenta of the resulting breakup fragments ($\alpha + t$) were reconstructed to find the invariant mass of ^{7}Li. By gating on one particular state of the projectile, the target energy can be reconstructed, as 3 out of 4 parameters of the kinematics are known (the initial momenta of the projectile and target and the final momentum of the projectile). Thus the final target momentum is constrained, and the subsequent missing mass can be found for the target (and thus its excitation energy).

The experiment with ^{7}Li was performed in August in 2015 at the Texas A&M University Cyclotron Institute. Their K-500 cyclotron provided a primary ^{7}Li beam with $E/A = 24$ MeV, that impinged upon targets of natural carbon, aluminum, and beryllium. Aluminum and beryllium are mono-isotopic (^{27}Al and ^{9}Be, respectively), while natural carbon is almost 99% ^{12}C. To make the analysis of the data using ^{12}C easier, the $\sim 1\%$ of ^{13}C in the target was neglected. The ^{12}C target not only satisfied the requirement of having a spin-zero target, but also the large separation between its ground and first excited state allowed for decisive

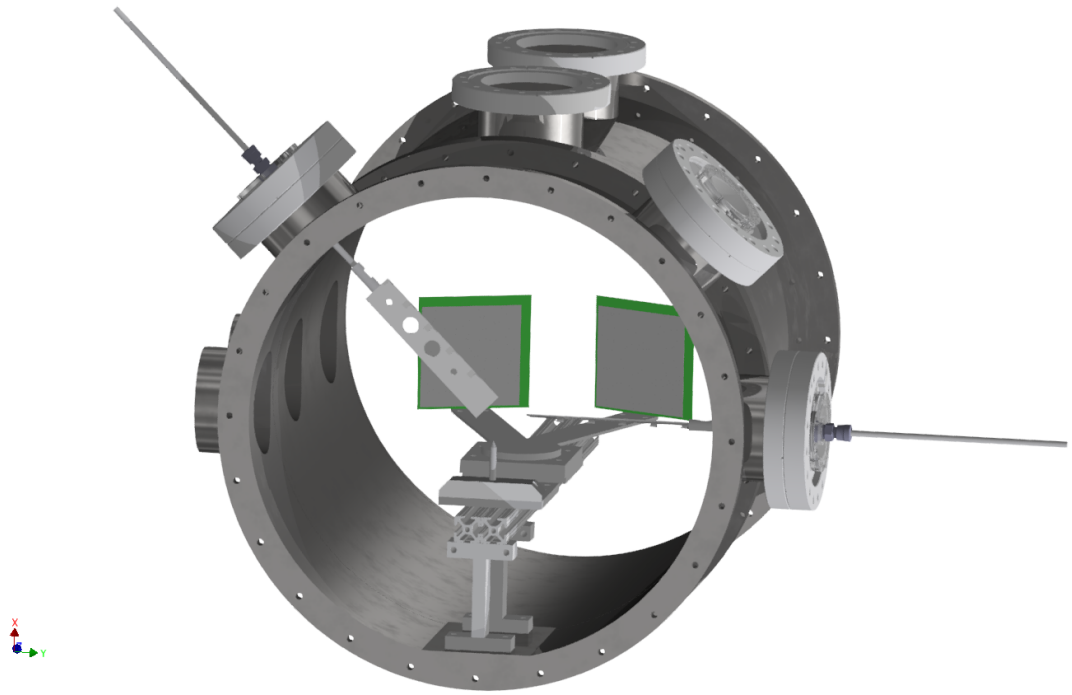

Figure 4.1: A 3D CAD model of the setup with two micron semiconductor TTT Si detectors.

exclusion of events where ^{12}C was excited.

4.1 Monte Carlo Simulations

While the geometrical acceptance of the detector array can be determined analytically, this is cumbersome and other physical effects cannot be easily taken into account. For instance, if two the fragments happen to go into the same CsI(Tl) then the event will not be counted. Analytically, this would require integrals over the available phase space, while in the Monte Carlo simulations (that sample the available phase space) one can just check if this has occurred for the simulated event and mark that simulated event as bad, as in the experiment such events are rejected.

Monte Carlo simulations were used to determine what would be the best detector array to use for the experiment. Two different detector arrays were simulated. One array included two design Micron semiconductor TTT Si detectors (128x128 segmented x-y strip detector,

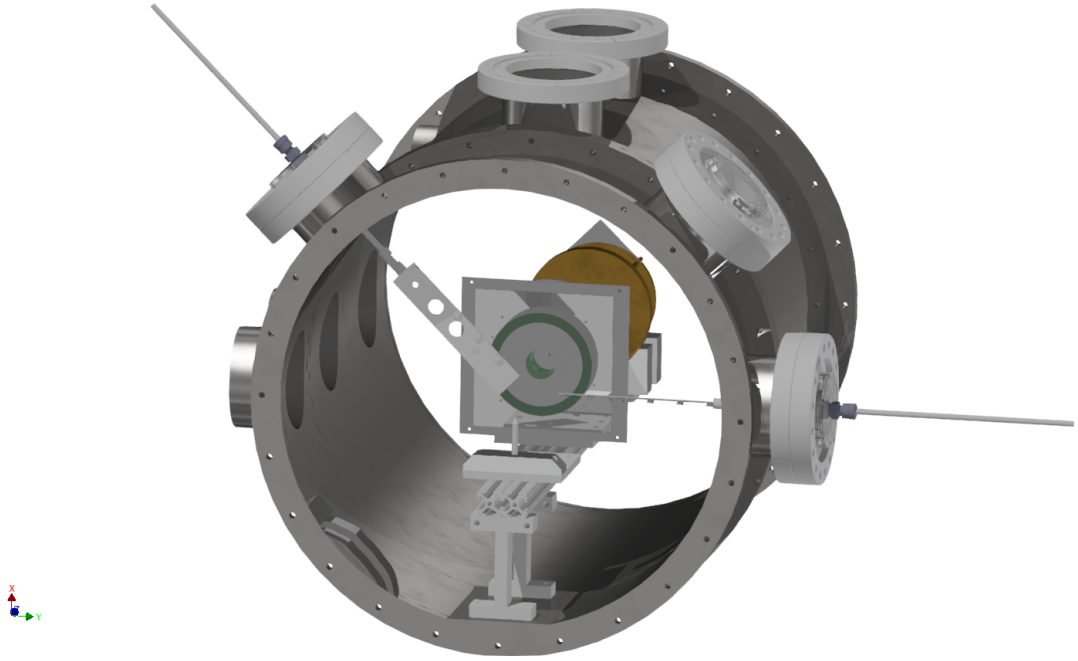

Figure 4.2: A 3D CAD model of the two annular Si detectors used in the experiment.

with an active area of 97mm x 97mm), shown in Fig. 4.1, and the other included two annular Si detectors, shown in Fig. 4.2. These Monte Carlo simulations were not only useful for determining the setup, but were also crucial for extracting the magnetic substate distributions of the inelastically excited ^{7}Li* by generating geometrical-detector-array efficiency maps, that are used to correct the experimental hit maps..

Of the two options considered, the two design TTT option provided large angular coverage, and much better angle resolution, resulting in better invariant-mass reconstructions. Their main drawback was the feasibility of the setup. To mount the TTT's, movable arms would have to be mounted inside the vacuum chamber, and accurate measurements of the distance from the detectors to the target would need to be determined. A 3D CAD model of a possible experimental setup with two TTT Si detectors is shown in Fig. 4.1. Because a sizeable gap between the detectors is required to allow the beam to pass through (and be out of range of elastic scattering), the detection efficiency of the breakup fragments suffered.

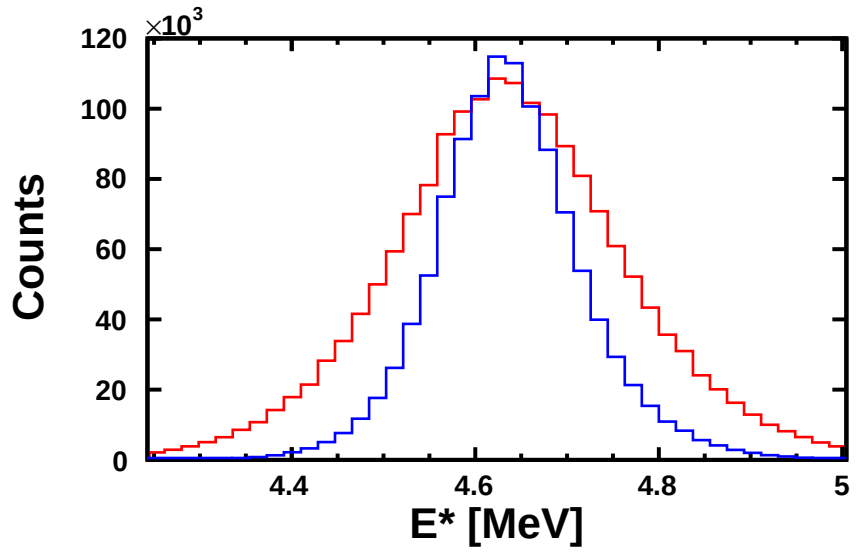

Figure 4.3: A comparison between the expected resolution of the invariant-mass reconstruction of ^{7}Li* [$J^{\pi} = 7/2^{-}$, 4.63 MeV] using two TTT's (blue) and the two annular Si's (red). For the TTT's a Gaussian with FWHM = 185 keV was fit to the distribution, while the fit for the annular telescopes resulted in a FWHM = 280 keV.

The overall geometrical efficiency of a typical double TTT setup was 37.4%.

An annular detector array provided much more coverage of the decays, as the beam can pass through the center of the devices. The geometrical efficiency determined for this array in the experimental setup was 58.5%, significantly larger than that for two TTT's. The setup was also made easier, as the annular detectors could be mounted to one rail which would need to be aligned with the beam-axis. Distances to the detectors were determined by putting spacers on the rail. Detailed drawings of the setup were made in 3D-CAD, so the distances to the target were able to be determined by the 3D models of the setup. Another advantage of this setup was the reduced Si-channel count. A 3D CAD model of the setup used in the experiment is shown in Fig. 4.2. While the main goal of the experiment was science focused, the experiment was also a chance to debug the latest generation HINP-16C chips, as this experiment was the first run with this technology.

A comparison of the expected invariant-mass resolutions for the particular state of interest, from each setup, are shown in Fig. 4.3. It was ultimately decided to go with the annular

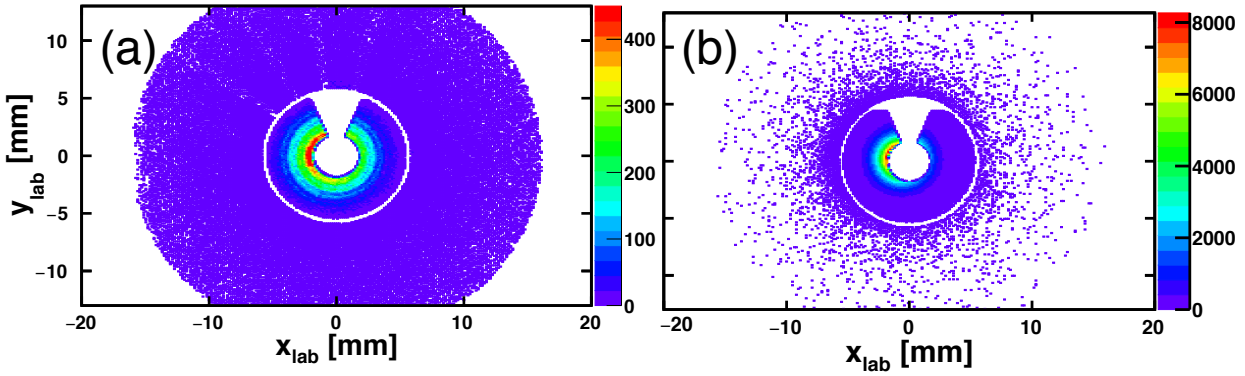

Figure 4.4: The effects of the beam alignment can be seen by the asymmetry of the distribution with respect to ϕ_{lab}. (a) The experimental hit-map of detector events for ^{7}Li* breakup events after scattering off the ^{12}C target. (b) Simulated hit-map of ^{7}Li elastic scattering off the ^{12}C target. The effects of the beam divergence and beam misalignment have been included in the simulation.

detector array due to the ease of setup and larger efficiency, even though the invariant-mass energy resolution was worse. It did turn out that aligning the detectors with the beam axis was more difficult than expected, and a tilt with respect to the beam axis and detector had to be taken into account in the Monte Carlo simulations.

The tilt of the beam axis with respect to the detector axis was determined to be 0.62^{o}. This tilt was determined from Monte Carlo simulations by rotating the beam in the simulation until the experimental hit-map of elastic-scattering events was largely reproduced. A comparison of the experimental and simulated hit-maps of elastic ^{7}Li scattering off the ^{12}C target is shown in Fig. 4.4. The tilt of the beam is very apparent in the experimental hit-map for the downstream detector, where there is a clear asymmetry in the azimuthal distribution of events around the detector axis. A beam divergence characterized by a two-dimensional Gaussian with $\sigma_Y = 1.53^{o}$ and $\sigma_X = 0.32^{o}$ was also included in the simulations. The divergence parameters were calculated from LISE++ simulations of the several quadrupole and dipole magnet settings used to tune the beam [85]. The effects of a beam spot size at the target of 4 mm were also included. The beam spot was determined by tuning the beam through a 4 mm hole in a target blank covered in a scintillator. By looking at a camera

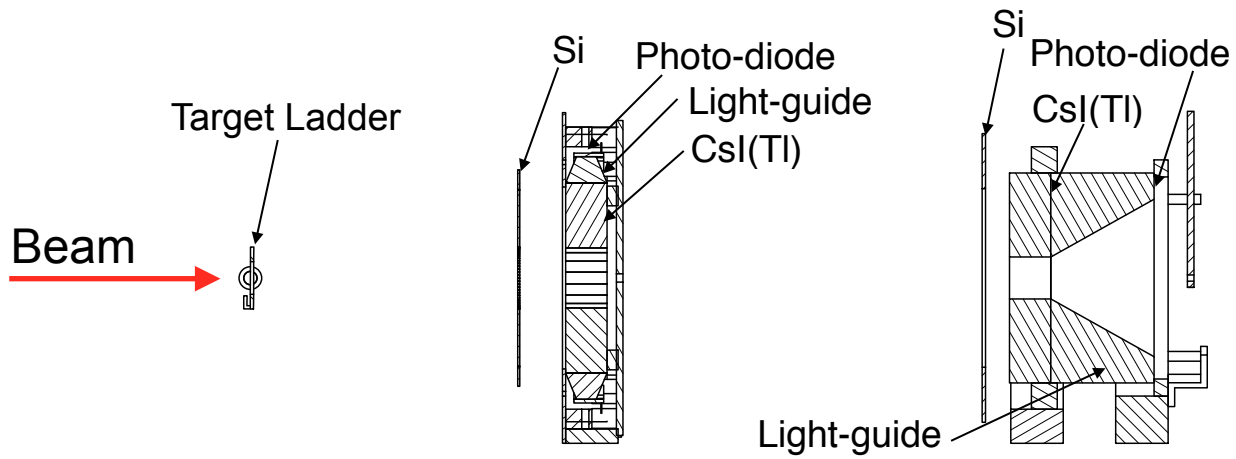

Figure 4.5: A schematic of the detector setup consisting of two Si-CsI(Tl) telescopes. The first telescope was placed 15 cm, and the second 35 cm, downstream of the target position.

directed at the target position, the amount of beam hitting the scintillating material was minimized.

4.2 Experimental Setup

The experimental setup for the detector arrays was designed using the 3D-CAD software, Autodesk Inventor. A schematic of the array is shown in Fig. 4.5, and a picture of the setup in Fig. 4.6. The carbon, aluminum, and beryllium targets were 9.60, 10.37, and 9.47 mg/cm^2 thick, respectively, and were mounted on a target ladder that allowed us to change targets while the chamber was under vacuum. The detector array consisted of two Si-CsI(Tl) ΔE-E telescopes. Here, telescope means that not only the energy and momentum of the particle can be measured but also the particle type. Pictures of the detectors used are presented in Fig. 4.7. The first telescope was placed 14.9-cm downstream from the target position, parallel to the beam-axis, and the other 35.8-cm from the target also along the beam axis. This setup provided a polar angular range of 2^o-16^o with a small gap at 5.6^o in the laboratory frame. A 13.8 mg/cm^2 sheet of Ta was placed in front of each Si detector to block any scattered electrons from entering the detectors.

Si detectors work as reverse-biased p-n junction semiconductors. When a p-n type semi-

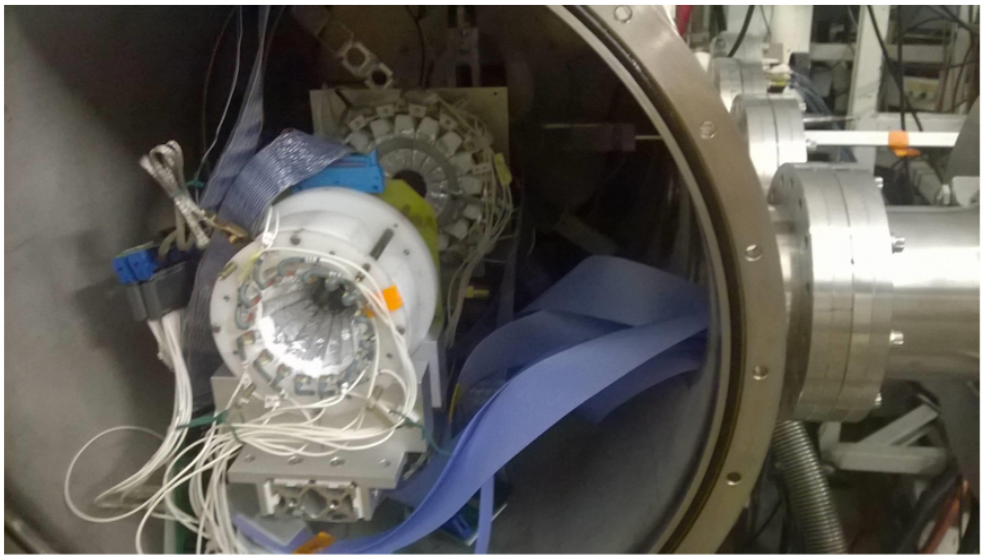

Figure 4.6: A picture from the experiment showing the detection hardware consisting of two telescope arrays.

conductor is run in reverse-biased mode, the depletion region (named so because the region at the junction is depleted of charge carriers) is physically widened. If relatively high-energy ionizing radiation passes through the material, electrons are excited to the conduction band (the band gap for Si is 1.1 eV) leaving behind "holes" in the valence band[†]. The electrons drift to the positive voltage side, while the correlated electron "holes" drift to the negative voltage side. In practice, this means that one side of the detector provides a negative voltage signal (electrons) and the other provides a positive voltage signal (holes). Since the Si wafer is segmented radially and azimuthally on the two sides, the event can be localized to a small region determined by the readout of a signal from one ring segment and one pie segment. The number of electron-hole pairs produced is proportional to the amount of energy deposited in the material across the thin dimension (perpendicular to the x-y plane of the detector), and so an accurate measurement of the energy deposited can be made by measuring the magnitude of the signal produced.

[†]If one is interested, the origin of the band gap is formulated from first principles in Appendix A.

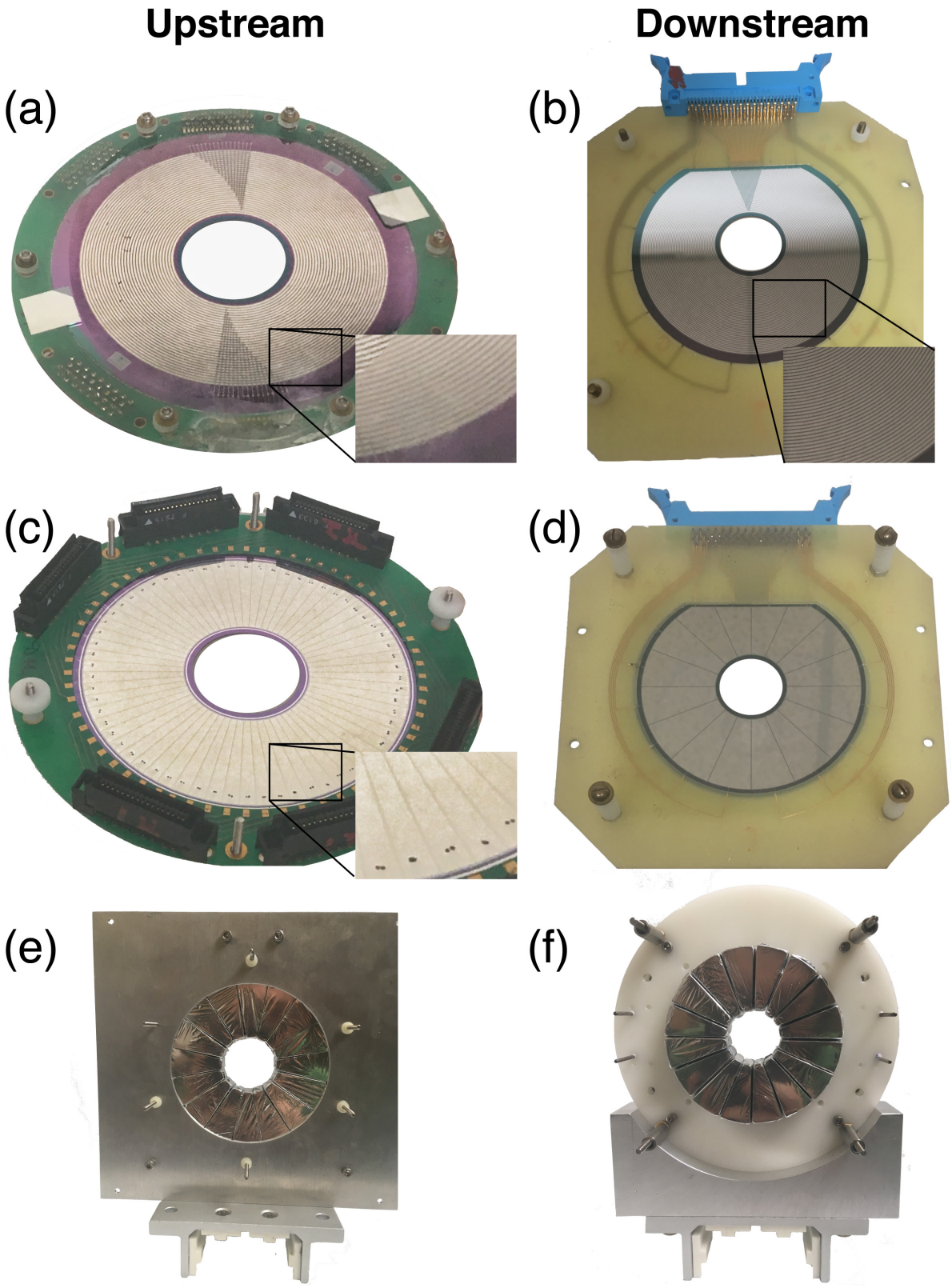

Figure 4.7

Figure 4.7: A display of the different components of the detector array. The upstream array (closest to the target) used a custom designed 525-μm thick segmented Si wafer with 32 rings and 64 pies, with a 15-mm radius hole in the center and an outer diameter of 85 mm. For the downstream array (furthest from the target), a design S2 Si detector was used, which has 48 incomplete rings and 16 pies, with a 11-mm radius hole in the center and an outer diameter of 70 mm. As can be seen, the top of the S2 silicon is truncated, and this feature of the S2 detector was taken into account in the Monte Carlo Simulations. Each Si detector was backed by a CsI(Tl) array with 16 pie-shaped crystals, displayed at the bottom. Panels (a) and (b) show the ring sides of each Si detector. Panels (c) and (d) show the pie-segment sides of each detector. Panels (e) and (f) show the CsI(Tl) detector arrays from the perspective of the target.

The front/back of each Si detector outputs a negative/positive signal, and is localized by the corresponding segments. On each segment, a thin wire bond allows the signal to be read out by 50-ohm ribbon cables. For performing the experiment, a map between the different channels and the spatial location was made.

The localization of the energy deposition event via the Si segments, allows the position of the event to be determined, and assuming the scattering event and/or decay happens in the target, the direction of the momentum can also be inferred. The rest of the energy is deposited in the CsI(Tl) crystals. After the particle type is identified via Eq. (4.1), the magnitude of the momentum can be deduced as the mass of the relevant particles are known to high precision. If the momenta and energies of all the scattering fragments are known, then the final scattering state's invariant mass can be reconstructed.

CsI(Tl) detectors work as scintillators, i.e. when ionizing radiation deposits energy into the detector, light is emitted. The integrated light output is approximately proportional to the energy deposited for the hydrogen isotopes, but for $Z > 1$, there are quenching effects due to the large dE/dx for these particles, which can cause non-linearities. Scintillators work on the principle of Stokes shift, wherein the emission spectrum is shifted from that for absorption. This can be explained by relaxation effects of the bulk material. The crystal excitations generated by the incoming radiation lose a small amount of energy through vibrations (phonon effects) or other processes and de-excite to a slightly lower energy level, which subsequently decays and emits light at a lower frequency. If this effect were not present, then the emitted light would be re-absorbed by the material. In the case of CsI(Tl), the spectrum of emitted light peaks at around 550 nm (yellow/green).

Each of the crystals and light guides in the upstream array were wrapped in reflecting material (teflon tape and aluminized mylar), except for a section where a photodiode was placed, and the total amount of light emitted was taken from the signal produced in the photodiode. The CsI(Tl) detectors in the downstream array had light guides affixed to the back, which were wrapped in reflecting material along with the crystal, and the photodiode readouts were placed at the downstream end of the light guide.

Figure 4.11 shows the electronics logic setup for the experiment, and displays the various routing of signals to the different electronic modules used. Because this experiment was focused on measuring a particle-unbound excited state of ^{7}Li that decays into an α and triton (i.e. sequential breakup), most of the experiment ran in a coincidence mode, whereby, only events were read out when at least two different CsI(Tl) detectors triggered. A few experimental runs lifted these constraints to demand at least one CsI(Tl) triggering for data to be taken, in order to get information about the elastic scattering cross section for the three different target systems. A Faraday-cup was placed at the end of the chamber in order to get absolute cross-section measurements, however, only relative cross sections were able to be confidently extracted from the data set as the Faraday-cup data were not calibrated.

Table 4.1: Calibration beams and the energies generated with the degraders.

Species	Energy [MeV/A]	Target	Thickness [mg/cm^2]	Degraded Energy [MeV/A]
p	24.2	Au	20.0	24.0
		Al	429	15.8
d	24.2	Au	20.0	24.1
		Al	429	20.3
		Al	858	15.8
	12.0	Au	20.0	11.9
α	24.0	Au	20.0	23.8
		Al	429	15.6

4.3 Calibrations

Energy calibrations for the CsI(Tl) detectors were performed with proton, deuteron, and α beams at several energies. These beams impinged upon a thin Au target, and several Al targets of varying thicknesses, giving different degraded energies. A summary of the calibration beams, degraders, and resulting energies is shown in Table 4.1. The energy calibrations determined for the deuterons were used for tritons.

For the downstream telescope, angle-independent CsI(Tl) calibrations were found for deuterons and alphas. On the upstream telescope, the photodiode readouts of the scintillated light were placed on the outside radius of the CsI(Tl) crystals (called out in Fig. 4.5). This external radial readout introduced non-uniform light collection that depended on the polar angle of the energy deposition in the CsI(Tl) crystal. To correct for this, energy calibrations were performed as a function of polar angle, taking into account the effective thickness and kinematic effects, by gating on eight different regions of polar angle determined by the Si detector. The raw spectrum demonstrating this defect of the upstream CsI(Tl) readouts can be seen by the dashed line in Fig. 4.8(a). Furthermore, the histograms under each dashed line correspond to different polar-angle regions determined by the Si detector. The result of performing a calibration for each angular region is shown in Fig. 4.8(b), and the effect of non-uniform light collection has been largely mitigated.

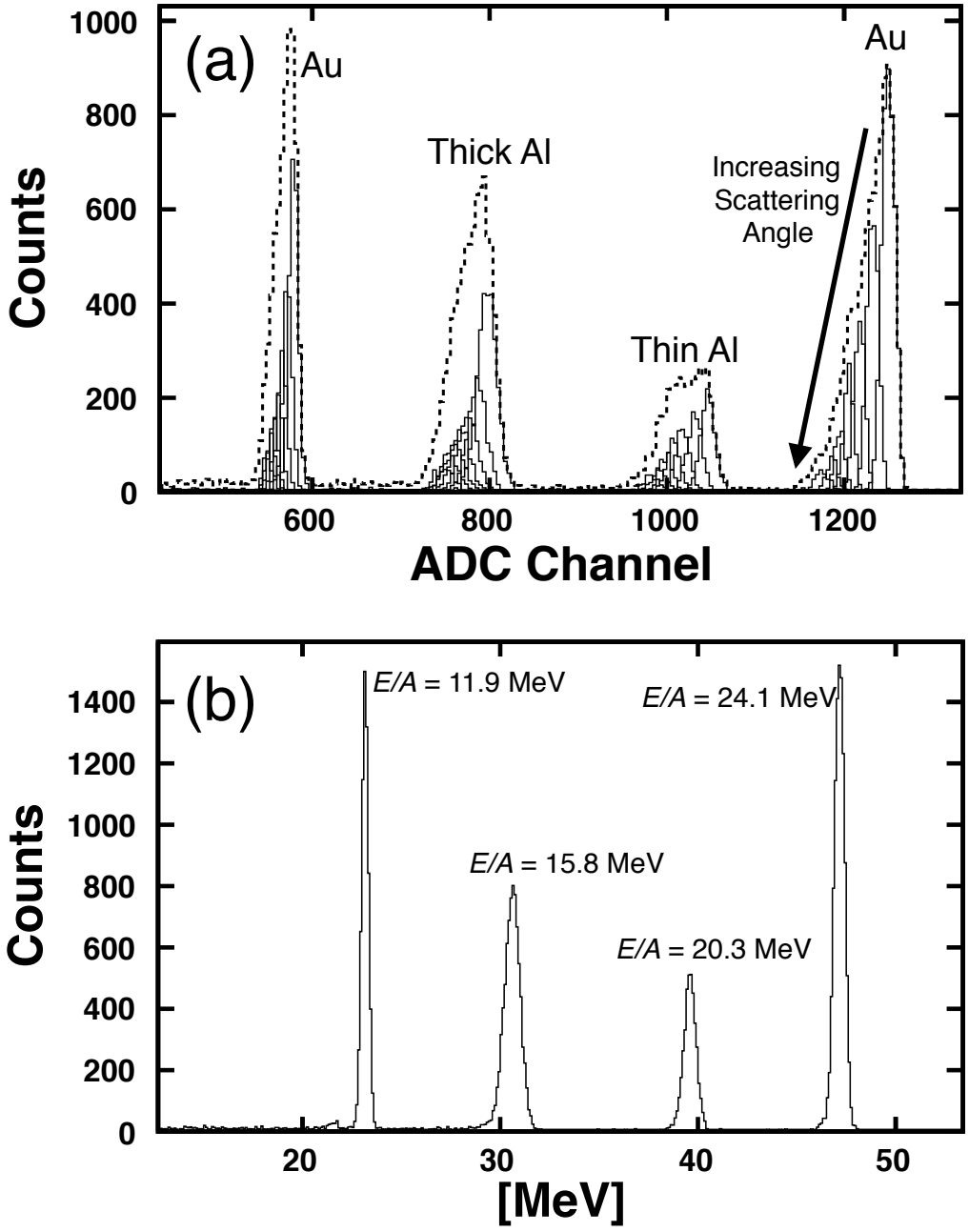

Figure 4.8: A comparison of the raw (a) and calibrated (b) spectra from one of the upstream CsI(Tl) crystals for all four deuteron calibration energies. The dashed line in (a) shows the raw spectrum for all scattering angles. The eight histograms under each peak show the contribution from different polar-angle regions. The inferred energies deposited in the Ta foil and Si have been added back into the energy reported in (b).

Table 4.2: α-particle energies from the mixed α source along with the branching ratios of the decays. α_0 corresponds to decays to the lowest-energy state of the daughter with a significant fraction, while α_1 and α_2 are decays to increasingly excited states of the daughter, respectively.

Parent	$t_{1/2}$ [years]	E_{α_0} [MeV]	E_{α_1} [MeV]	E_{α_2} [MeV]	f_{α_0}	f_{α_1}	f_{α_2}
^{244}Cm (a)	18.1	5.805	5.763	—	0.769	0.231	—
^{241}Am (b)	432.6	5.486	5.443	5.388	0.848	0.131	0.017
^{239}Pu (c)	24110	5.157	5.144	5.106	0.708	0.171	0.119
^{148}Gd (d)	71.1	3.182	—	—	1	—	—

Energy calibrations for the Si detectors were performed with a mixed α source of ^{148}Gd, ^{239}Pa, ^{241}Am, and ^{244}Cm. The α particle energies and branching ratios for these isotopes are presented in Table 4.2. For the downstream Si detector, the α particle calibrations were sufficient. A summary spectrum showing the calibrated α-particle spectrum (ordinate) for each pie segment in the S2 Si detector (abcissa) is shown in Fig. 4.9. Although the calibrations worked for the downstream detectors, the α-particle calibrations were not sufficient for the upstream Si detector either due to a non-uniform dead layer or an incomplete depletion region. Therefore, the upstream Si detector was used solely for determination of the scattering angle and particle identification. The energy lost in the upstream Si was determined from the energy deposited in the CsI(Tl) and SRIM energy-loss tables [86]. The spectrum in Fig. 4.8(b) has the inferred energy lost in the upstream Si, and Ta foil, added back into the reported energy, thus the energies shown in Fig. 4.8(b) can be directly compared to the energies in Table 4.1.

The particle identification was performed by plotting the energy deposited in the thin Si versus the remaining energy deposited in the CsI(Tl) crystals. The element and isotope can be interpreted (i.e. identified) based on the charge and mass proportionalities in the Bethe-Bloch equation. In a low-energy approximation the proportionalities are given by,

$$\frac{dE}{dx} \propto \frac{Z^2 A}{E}. \tag{4.1}$$

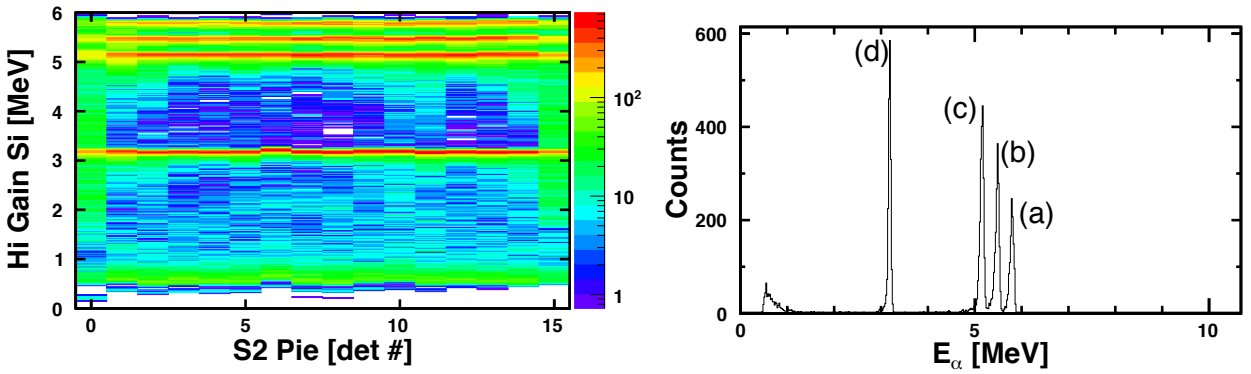

Figure 4.9: A summary plot of the S2 alpha calibrations, where the calibrated alpha spectrum is plotted for each of the pie Si segments, as well as a plot of a calibrated α-particle spectrum from one of the S2 pie segments. The peaks correspond to α particles from the different isotopes in Table 4.2, and they are labeled accordingly.

The $1/E$ dependence for each particle type can be seen in a sample ΔE-E plot shown in Fig. 4.10. The Si detectors, being thin, provide a direct measure of dE. The thick CsI(Tl) detectors provide a measure of the total energy, E. Therefore a plot of dE(Si) versus E(CsI) yields loci of elements and isotopes splayed in proportion to Z^2 and A. The Z^2 dependence of the energy deposition is clear in Fig. 4.10, where elements up to Li are shown. The isotopic determination is robust, as the bands for each isotope are well separated. It should be noted that this method of particle identification will only work for isotopes that are particle stable (i.e. they live long enough to make it to the detector). There is a noticeable gap between ^{4}He and ^{6}He because ^{5}He is particle unstable (in fact there are no stable A=5 nuclei). From these plots, it is clear which line corresponds to the primary beam isotope as there is a large peak corresponding to elastic scattering, confirming the assignment for ^{7}Li.

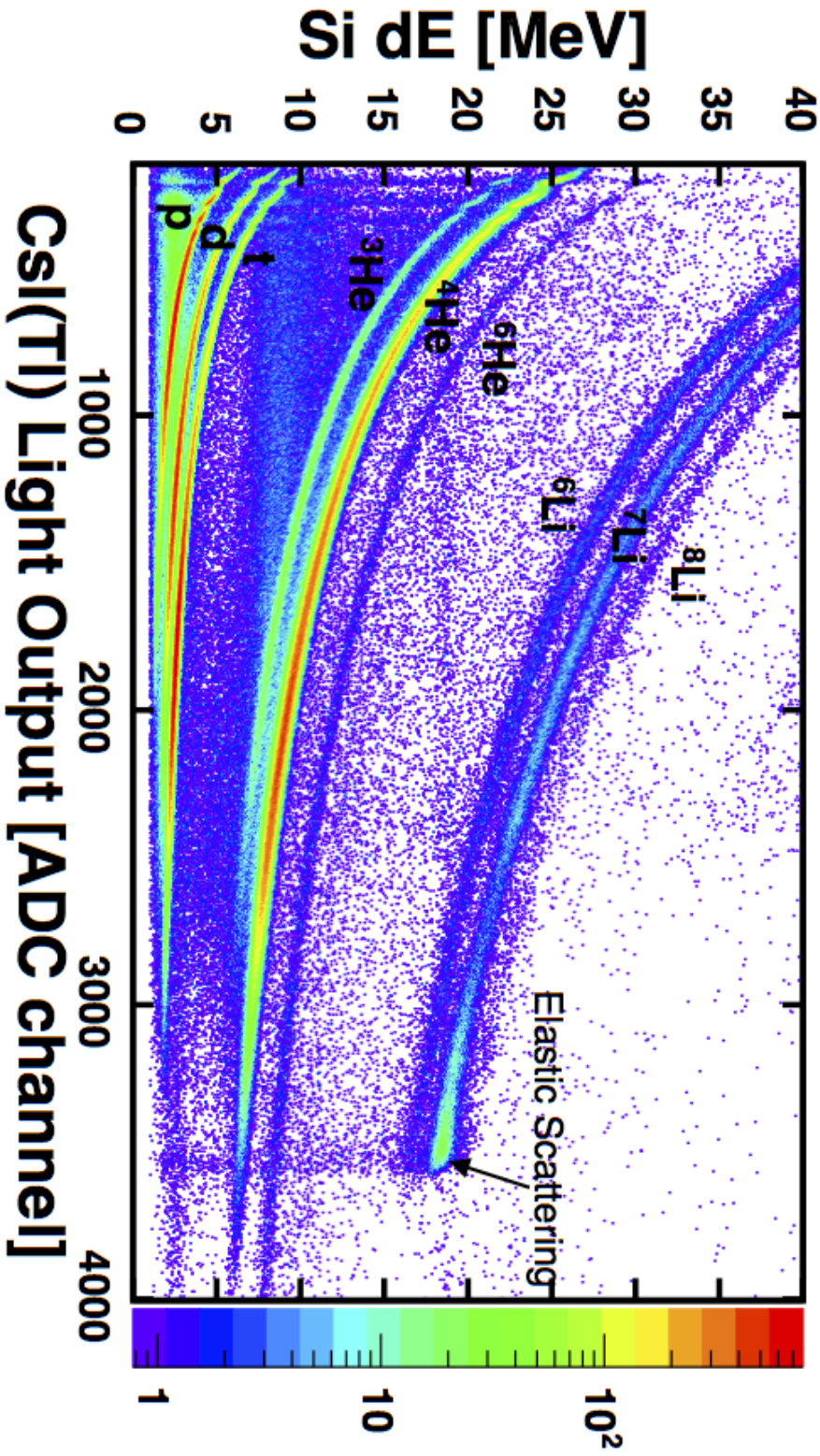

Figure 4.10: A sample ΔE-E spectrum obtained for one CsI(Tl). Clear bands for each element can be seen, with separate bands for each isotope.

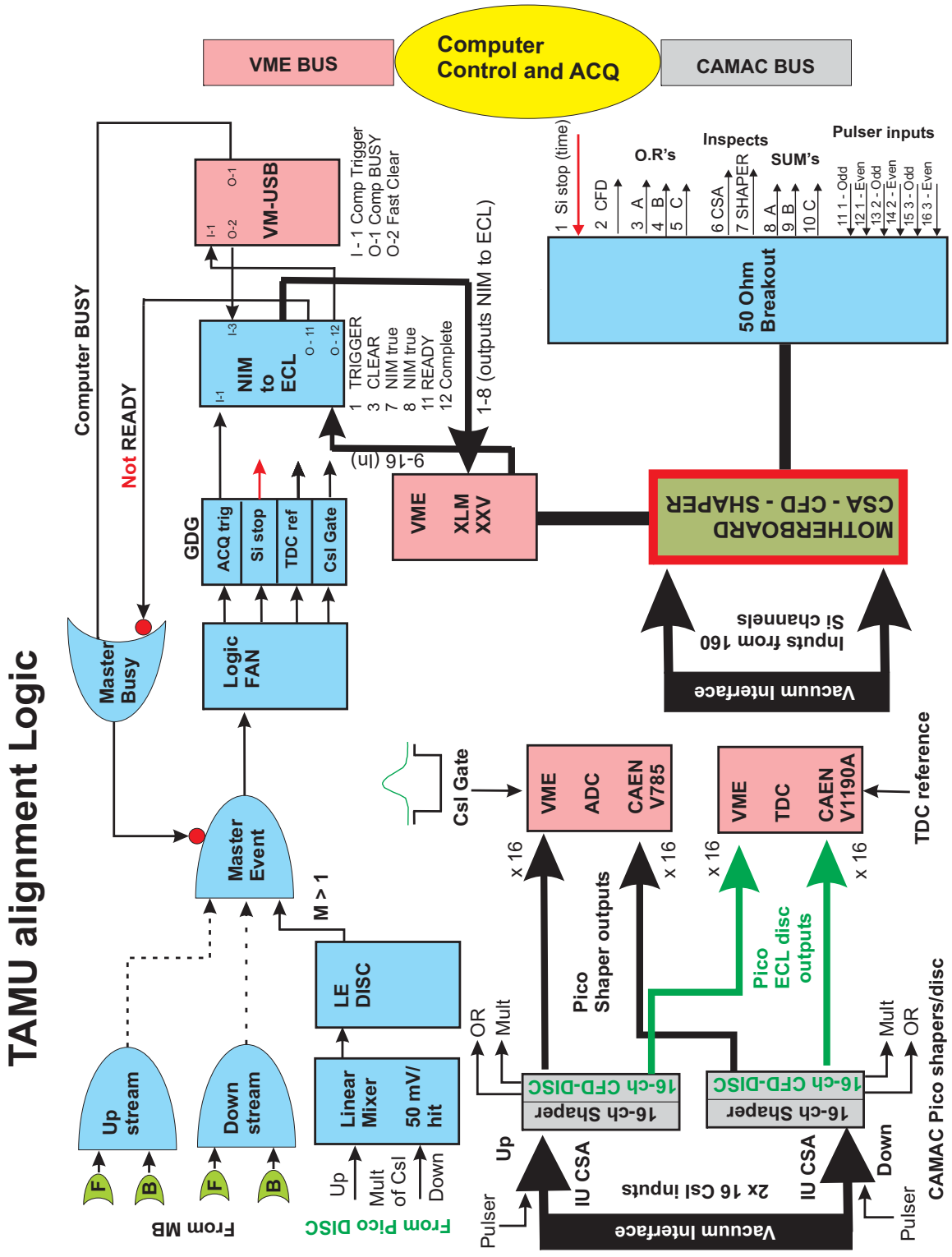
TAMU alignment Logic
VME BUS
Computer Control and ACQ
CAMAC BUS
VM-USB
I - 1 Comp Trigger
O-1 Comp BUSY
O-2 Fast Clear
Computer BUSY
Not READY
NIM to ECL
1 TRIGGER
3 CLEAR
7 NIM true
8 NIM true
11 READY
12 Complete
1-8 (outputs NIM to ECL)
9-16 (In)
1 Si stop (time)
2 CFD
O.R's
3 A
4 B
5 C
Inspects
6 CSA
7 SHAPER
SUM's
8 A
9 B
10 C
Pulser inputs
11 1 - Odd
12 1 - Even
13 2 - Odd
14 2 - Even
15 3 - Odd
16 3 - Even
50 Ohm Breakout
VME XLM XXV
MOTHERBOARD CSA - CFD - SHAPER
Vacuum Interface
Inputs from 160 Si channels
GDG
ACQ trig
Si stop
TDC ref
CsI Gate
Logic FAN
Master Busy
Master Event
M > 1
LE DISC
Linear Mixer
50 mV/ hit
Up
Mult
of CsI
Down
From Pico DISC
Up stream
Down stream
F
B
From MB
CsI Gate
VME ADC CAEN V785
VME TDC CAEN V1190A
TDC reference
x 16
Pico Shaper outputs
Pico ECL disc outputs
OR
Mult
16-ch Shaper
16-ch CFD-DISC
Pulser
IU CSA
2x 16 CsI inputs
Vacuum Interface
CAMAC Pico shapers/disc

Figure 4.11

Figure 4.11: Electronics logic for the alignment experiment at TAMU. All elements that sit between the vacuum interface (thick-black band) and the host acquisition computer (yellow oval) are indicated. The elements in blue are NIM modules, and with the exception of the breakout box, are logical (logic in – logic out) elements. The elements in pink sit in the VME crate and those in gray (servicing the CsI(Tl)) are CAMAC units. The motherboard (green with a red boarder) services the Silicon detectors and hosts the ASIC system. The host computer has access to the high- and low-speed parallel buses of the VME and CAMAC backplanes. The thin lines are individual 50-ohm coaxial cables while the thick lines are either 50-ohm flat 16-ch coaxial ribbon (AMP style) or 110-ohm flat (standard density) 34-conductor or (high-density) 68-conductor ribbon cable. The shielded coaxial cable is used for linear signals while standard ribbon is used for logical signals. Standard NIM to standard ECL logic conversion is done in one module that both sends to (i.e. output on lines 1-8) and receives from (input on lines 9-16) the logic module that sits in the VME crate. That module (XLM-XXV) orchestrates the event readout. In addition to XLM-XXV module, there are three other modules (pink) in the VME crate. Two of these service the CsI(Tl) detectors, one for digitizing the pulse heights and the other for digitizing the times of the CsI(Tl) detectors.

The signal processing for both Si and CsI(Tl) detectors follow similar logical paths, starting with a CSA and followed by a shaping amplifier, for the linear branch, and a CFD-discriminator for the generation of a time. The CSA's for the CsI(Tl) are of the Indiana University design [87]. Two 16-ch boards of the IU preamps are bolted to the outside of the vacuum chamber. The amplified CsI(Tl) signals are processed by two dual-width 16-ch CAMAC units with linear shapers and CFD discriminators for each channel [88]. One of these units is used for the upstream CsI(Tl) array and the other for the downstream array. The shaped outputs are fed to ADCs and the CFD outputs are fed to TDCs to be readout at acquisition. In the case of the Si detectors, the CSAs, CFDs, peak trackers (and more) are in the ASIC HINP-16C. Two of these chips are on each chip board (CB), six of which were used in this experiment and are housed in the motherboard (MB). The MB is also bolted to the vacuum chamber, to allow direct feed through of the Si signals.

The front-end logical branches generate OR's and linear multiplicity signals (M) that have an amplitude proportional to the number of hits. Leading edge (LE) discrimination of these signals allows for multiplicity selection. Selecting $M_{CsI} > 1$ was used to generate the master event trigger for the experiment. The calibration of the Si and CsI(Tl) detectors required other triggers (dotted lines).

Both the Si and CsI(Tl) pulse processing streams allow for pulsing of channels and inspection of the linear and logical outputs for any channel. These testing features can be controlled remotely and any signal can be visualized (on an oscilloscope) remotely. The part of the logic diagram that allows for this has been omitted.

Chapter 5

Data Analysis

"Mass and energy are both but different manifestations of the same thing"

—Albert Einstein

Methods for measuring the spin alignment of excited nuclei are dependent on the decay mode. For bound excited states, the population of magnetic substates (and thus the spin alignment/polarization) can be measured by analyzing the angular distribution of an emitted γ ray [89, 90, 91, 92, 34, 93, 94]. On the other hand for unbound excited states, the angular correlations of the sequential breakup fragments can be measured to determine the final magnetic substates [48, 95], which is the approach taken in this dissertation. But first, the population of excited states has to be determined, and this was done through invariant-mass spectroscopy.

5.1 Invariant-Mass Reconstruction

A conserved quantity from special relativity is the *proper* or *invariant* mass of a particle. This is perhaps best understood by looking at the 4-momentum (which is conserved under Lorentz transforms),

$$p^{\mu} = \begin{bmatrix} E/c \\ p_1 \\ p_2 \\ p_3 \end{bmatrix}, \tag{5.1}$$

where E is the total energy of the particle (including the mass-energy), and the components p are the usual 3-momentum. The square gives the invariant mass,

$$p_{\mu}p^{\mu} = \begin{bmatrix} E/c, p_1, p_2, p_3 \end{bmatrix} \begin{bmatrix} E/c \\ p_1 \\ p_2 \\ p_3 \end{bmatrix} = -E^2/c^2 + p^2 = -m^2c^2, \tag{5.2}$$

which is just the usual momentum-energy relation from special relativity (the negative signs come from the *metric* for the spacetime, and here Minkowski (flat) spacetime is assumed). If $\mathbf{p} = 0$ (the 3-momentum), then we obtain Einstein's famous formula, $E = m_0c^2$. When a nucleus is excited its total energy increases, and consequently the mass increases. This is, in fact, true for any closed system which gains energy, including atoms, but in the case of atoms the electron orbital excitations are on the order of $\sim$eV. A 1 eV change in energy corresponds to a change in mass of $1.78{\cdot}10^{-33}$ g, which will likely never be directly measured (e.g. by putting in on a scale). Of course these types of transitions are measured all the time in Chemistry, and absolute measurements of the mass are not necessary. The same principle applies for invariant-mass measurements, where we measure changes in mass (energy) relative to the ground-state mass of the nucleus.

Since we can determine the total kinetic energy and particle type (mass) of the fragments from nuclear reactions using Si-CsI(Tl) telescopes, we can extract the momenta and energies

of the fragments. In the case of sequential breakup, we reconstruct the momentum of the nucleus of interest from the momenta and energies of the fragments, in their center-of-mass frame, and Eq. (5.2) becomes,

$$mc^2 = \left[(\sum_{\text{frag}} E_{\text{frag}})^2 + (\sum_{\text{frag}} \mathbf{p}_{\text{frag}} c)^2 \right]^{1/2} . \tag{5.3}$$

By subtracting off the known rest mass of the nucleus of interest we can obtain an excitation energy, or *invariant-mass*, spectrum. Because this method relies on accurate measurements of the momentum, it is required that there is little uncertainty in the location of the decay vertex. In practice, this distance is constrained by the nucleus of interest decaying near the target position (i.e. scattering event), which is satisfied if the lifetime is sufficiently short. For the case of ^{7}Li* [4.63 MeV], the intrinsic width of the state is 93 keV, which corresponds to a lifetime on the order of 10^{-21}s by the Heisenberg uncertainty principle. At a beam energy of $E/A = 24$ MeV, the velocity of ^{7}Li* is 6.67 cm/ns, and so it travels a mean distance of only $\sim$ 200 fm before decaying, constraining the decay to inside the target. All of the subsequent invariant-mass spectra generated from reconstructions of the decay fragments of the projectile-like fragment (PLF) use the data from all three targets. This particular application of the invariant-mass method relies on the fact that only a small portion of the mass, with reference to the ground state, is measured. Because the particle type is able to be identified, the majority of the mass (and thus energy) is already accounted for.

The invariant-mass method is not strictly for characterizing nuclear reactions. In fact, one of the major discoveries of physics in the 21$^{\text{st}}$ century came from invariant-mass measurements of γ-γ events; the mass measurement of the Higgs boson by the ATLAS[†] collaboration at the LHC [96]. Figure 5.1 shows a schematic for the decay of the Higgs boson. There are many processes that may contribute to the decay of the Higgs (denoted by the circle), and some of these will result in the emission of two γ rays. The resulting invariant-mass reconstruction of $\gamma - \gamma$ events shows a clear peak at $m_{\gamma\gamma} = 125.4$ GeV, giving an accurate

[†]ATLAS is also the name of a detector array, it is not be confused with the facility at Argonne.

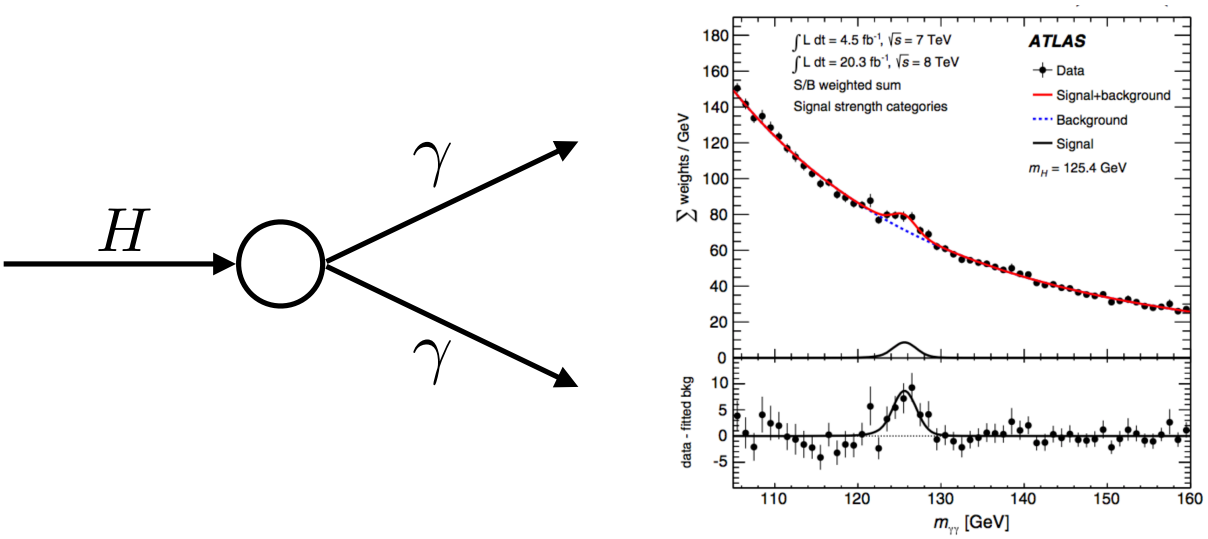

Figure 5.1: A simple decay scheme of the Higg's boson into two γ's. The circle denotes that many processes may decay through this mode. The resulting invariant-mass reconstruction is shown as well, giving a mass measurement of the Higgs boson of $m_H = 125.4$ GeV and FWHM = 4 GeV. The intrinsic width is expected to be ~ 10 MeV, so this FWHM is almost all detector resolution.

measurement of the Higgs mass. For nuclear experiments, we can replace the Higgs with ^{7}Li or another PLF, and the two γ's by an α and triton or other decay fragments. The principles of the measurements are the same.

5.2 Nucleon Transfer and Knockout

5.2.1 ^{6}Li

^{6}Li is produced when a neutron is transferred to the target, or knocked out from the ^{7}Li projectile. Excited ^{6}Li is unbound with respect to $\alpha + d$ emission, and thus measuring this decay channel allows one to see the production of ^{6}Li*. Furthermore, an invariant-mass reconstruction of $\alpha + d$ events is a good test of the energy calibrations, and the resulting spectrum is shown in Fig. 5.2(a). The width of the first particle-unbound state in ^{6}Li at 2.185 MeV is 24 keV[†] much smaller than the experimental resoultion, so the measured width of this state is a good indicator of the instrinsic resolution of the detector system. The

[†]From the Heisenberg uncertainty principle this corresponds to a half-life of 1.4×10^{-20} s.

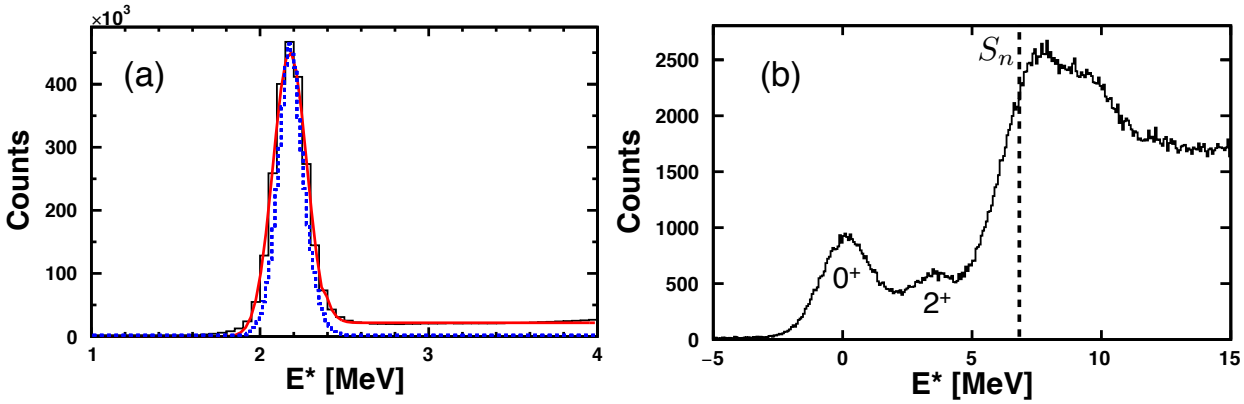

Figure 5.2: (a) The invariant-mass spectrum for $\alpha + d$ events showing the first particle-unbound state of ^{6}Li. The solid red line is a fit to the measured distribution, shown by the histogram, with the background modeled by an inverse Fermi function. The dashed blue line is the expected experimental resolution from the Monte Carlo simulations. (b) By gating on the peak shown in (a) a missing-mass reconstruction of the residual ^{10}Be nuclei was made for events with the ^{9}Be target. The dashed line shows the neutron separation energy, S_n, for ^{10}Be.

solid red line in Fig. 5.2(a) is a fit to the measured distribution using a Fermi function to model the background. The centroid of this fit is 2.177 MeV, with a FWHM of 235 keV. The measured width is a little larger than predictions from Monte Carlo simulations of the detector system, shown as the blue dashed line in Fig. 5.2(a). The discrepancy is most likely due to imperfect energy calibrations.

5.2.2 ^{10}Be

The reconstruction of the target excitation energy is not restricted to inelastic reactions, but can be performed for the residual nucleus from nuclear reactions such as transfer (the projectile drops off a nucleon/nucleus to the target) or pickup (the projectile grabs a nucleon/nucleus from the target). The target excitation energy is determined from momentum and energy conservation, since 3 out of 4 components of the kinematics are known the "missing" mass can be determined, and hence this scheme is known as the missing-mass method. In the case of neutron transfer to the ^{9}Be target, the resulting nucleus is ^{10}Be. Gating on the 2.65 MeV state in ^{6}Li, we can reconstruct the momentum of the residual target nucleus and the missing-mass reconstruction is shown in Fig. 5.2(b). The ground state of ^{10}Be

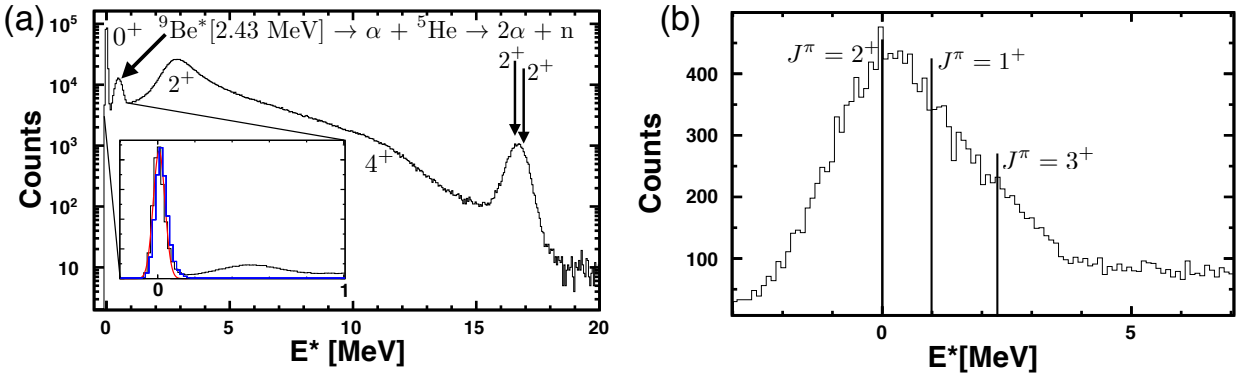

Figure 5.3: (a) The invariant-mass spectrum for $\alpha + \alpha$ events showing states in ^{8}Be. The peak around 0.5 MeV can be attributed to the decay of an excited state in ^{9}Be. A log scale is used in order to see the peak above 16 MeV. The inset figure shows a Gaussian fit to data (solid red line) and the expected resolution from Monte Carlo simulations (blue) of the ground-state resonance. The widths of the simulation and data are similar but the centroid of the simulation is shifted with respect to the data by $\sim$ 15 keV. (b) By gating on the ground-state peak of ^{8}Be, an invariant-mass reconstruction of the residual ^{8}Li was made.

($J^\pi = 0^+$), as well as the first excited $J^\pi = 2^+$ state, is clearly seen. The intense structure at higher energies is likely due to neutron knockout reactions in the projectile. In this case, the residual target nucleus is ^{9}Be, and the particle threshold for ^{9}Be + n is at 6.81 MeV (otherwise known as the neutron separation energy) with reference to the ^{10}Be ground state, right where the intense structure appears.

5.2.3 ^{8}Be

^{8}Be is produced when ^{7}Li picks up a proton from the target. The invariant-mass reconstruction of ^{8}Be is another good case to check the α calibrations, since the ground state of ^{8}Be is unstable with respect to $\alpha - \alpha$ breakup by only 91.8 keV.[†] The ground-state resonance of ^{8}Be is also very narrow, with a width of only 5.57 eV. Figure 5.3(a) shows the invariant-mass reconstruction of $\alpha - \alpha$ events and several states of ^{8}Be are seen, including the ground state and the first excited $J^\pi = 2^+$ [3.03 MeV] state. There is also a signature of the 3.5 MeV wide $J^\pi = 4^+$ state, around 11 MeV.

[†]Interestingly, as mentioned for A=5 nuclei, there are also no stable A=8 nuclei.

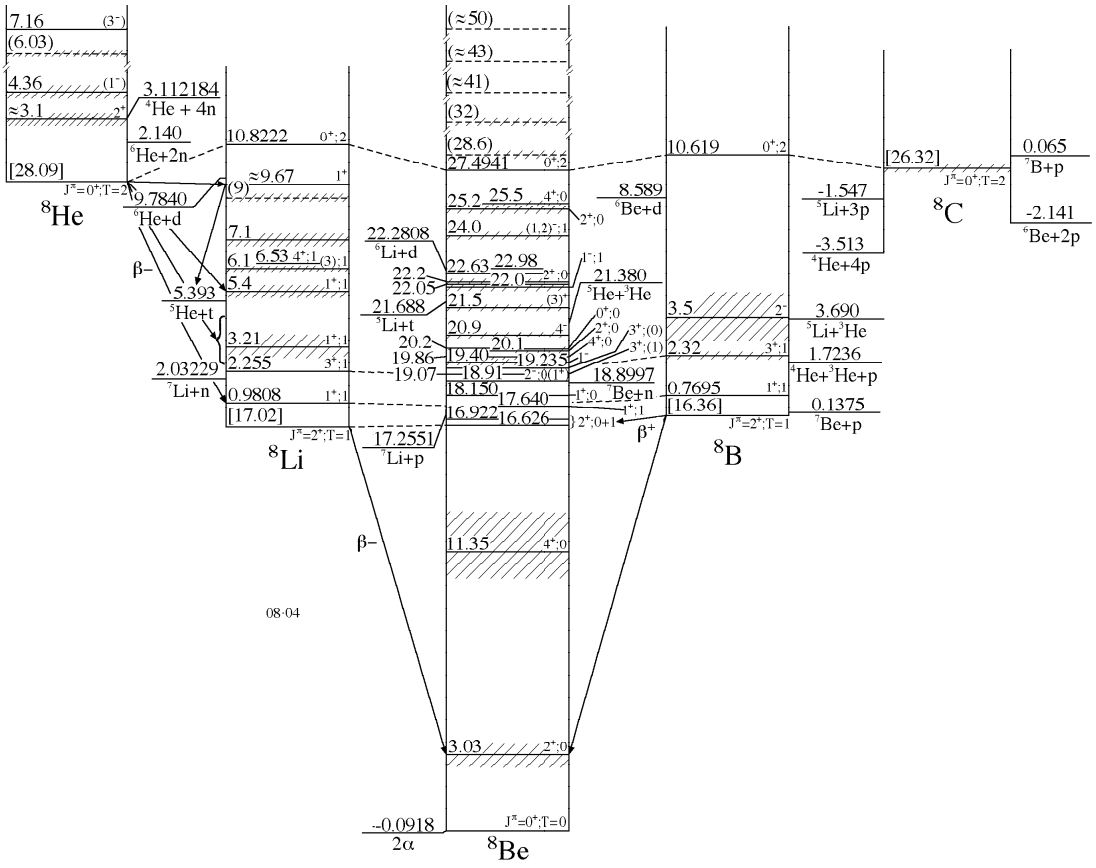

Figure 5.4: A=8 isobar diagram from TUNL, showing the different energy levels and spin/isospin assignments to the different states. Analog states are connected by the dashed lines.

Isospin is not a perfect symmetry, and isospin symmetry breaking is indicated by the presence of some isospin mixed states. The peak above 16 MeV can be attributed to the mixing of two isobaric analog states in ^{8}Li and ^{8}B ($J^\pi = 2^+$) at 16.6 and 16.9 MeV. Fig. 5.4 shows an $A = 8$ isobar diagram from TUNL which highlights these analog states. Because these states in ^{8}Be are the analogs to the ^{8}Li and ^{8}B ground states, they are also characterized by $J^\pi = 2^+$.

The inset in Fig. 5.3(a) shows a Gaussian fit to the data (red solid line) and the expected resolution from Monte Carlo simulations (blue) for the ground-state decay of ^{8}Be. The FWHM of the simulation is 78 keV, compared to the FWHM for the data of 73 keV. The simulation's fitted centroid is at 21 keV, while the data's fitted centroid is at 7 keV. The discrepancy between the simulation and data suggest there is a small systematic error, which

could be attributed to imperfect energy calibrations or in the experiment's setup.

^{9}Be is produced when ^{7}Li picks up a proton and neutron from the target. The peak around 0.5 MeV in Fig. 5.3(a) is attributed to the decay of ^{9}Be* [2.43 MeV] $\rightarrow$ ^{5}He + α $\rightarrow$ 2α + n [97]. ^{5}He decays rather quickly, as its ground state is rather broad, with a width of 0.648 MeV†. The Q-value for neutron decay of ^{5}He is rather small (0.798 MeV), and so there is little recoil given to the resulting α particle. Therefore, the final α particles are still strongly correlated. With increasing energy of the emitted neutron, such a peak would be broadened until it was completely washed out.

5.2.4 ^{8}Li

Gating on the ground state peak of ^{8}Be, the momentum and energy of the residual target nucleus was determined. Since the projectile picked up a proton from the target, the residual nucleus with the ^{9}Be target is ^{8}Li. The missing-mass reconstruction for ^{8}Li is shown in Fig. 5.3(b). The wide peak is due to two higher-lying excited states in ^{8}Li, and these states are indicated by the solid black lines.

5.3 Inelastic Processes

5.3.1 ^{7}Li

Since the primary beam of the experiment is ^{7}Li, the population of excited states in ^{7}Li predominately come from inelastic reactions with the target. A level scheme for ^{7}Li is provided in Fig. 5.5(e). ^{7}Li has one low-lying excited state at 0.478 MeV, which decays by γ-ray emission. Since the experiment did not have any γ-ray detectors, there is no way to determine the population of this state from the data set. The 2$^{\text{nd}}$ excited state (and the particular state of interest) in ^{7}Li, with $J^{\pi} = 7/2^{-}$ at 4.63 MeV, is particle unbound with respect to $\alpha + t$ emission by an energy of 2.169 MeV. This is the first state seen in the

†From the Heisenberg uncertainty principle this corresponds to a half life of 5.1 $\times 10^{-22}$ s

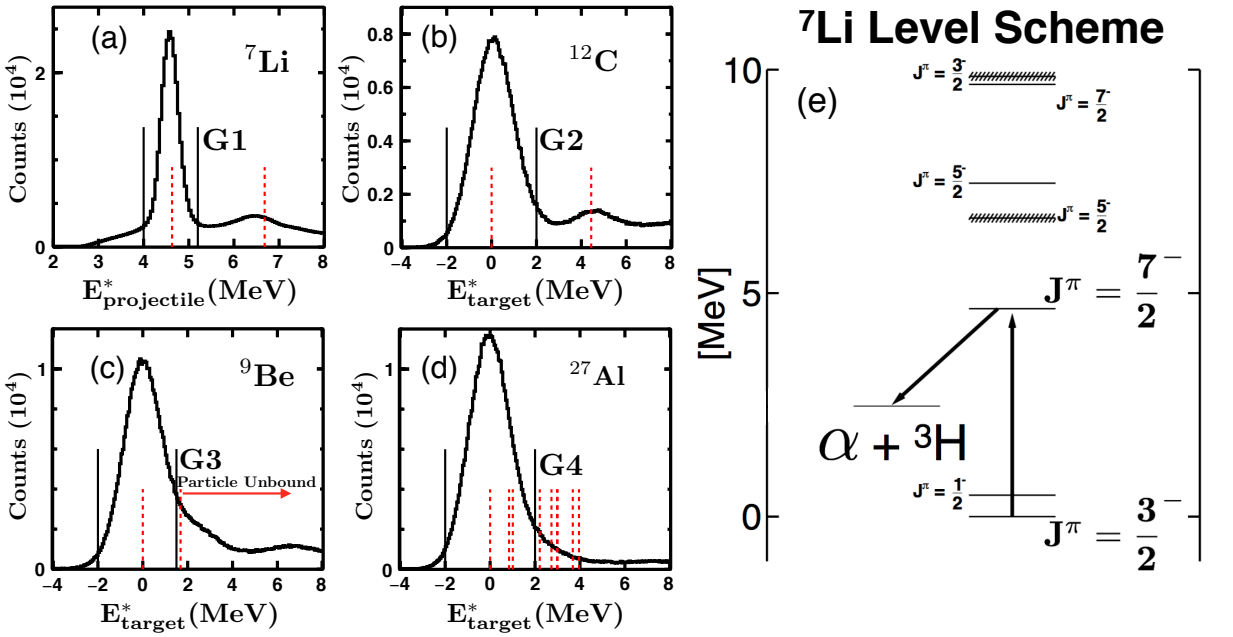

Figure 5.5: (a) The invariant-mass spectrum for $\alpha + t$ events showing particle-unbound states in ^{7}Li. By applying the gate G1, the $J^\pi = 7/2^-$ [4.63 MeV] state can be studied further. The reconstructed target-excitation-energy spectra for (b) ^{12}C, (c) ^{9}Be, and (d) ^{27}Al. The red dashed lines correspond to energy levels in the respective nuclei. (e) A level scheme for ^{7}Li.

$\alpha + t$ invariant-mass reconstruction shown in Fig. 5.5(a). In order to focus on the particular reaction of interest, a gate (called out by G1 in Fig. 5.5) can be placed on the resonance. The energy determined for the higher-lying states of ^{7}Li tend to be lower in energy than the accepted values for the resonance, as is apparent for the $J^\pi = 5/2^-$ state [6.68 MeV] in Fig. 5.5(a). This is most likely due to the fact that wide resonances are not equally populated, as the population of the state depends on the method of formation. This was very apparent for the case of ^{5}H, where the overall resonance energy and width of the ^{5}H resonance is largely dependent on the reaction populating it [98].

5.3.2 Target-Excitation-Energy Reconstruction

The excitation energy plots shown in Fig. 5.5(b)(c)(d) were created by gating on the $J^\pi = 7/2^-$ state, using G1 shown in Fig. 5.5(a). The target excitation energy spectrum from 2-body kinematics for ^{12}C is shown in Fig. 5.5(b). There is a clear separation between

the ground state and the first excited state in ^{12}C at 4.4 MeV allowing for a clean gate [G2]. The target excitation energy spectrum determined for ^{9}Be is shown in Fig. 5.5(c). The overall resolution of the device limited the ability to fully separate the populations of the ground and first excited state in ^{9}Be. Furthermore, ^{9}Be is particle unbound with respect to ^{8}Be + n, this will contribute to the tail seen above that energy. Therefore a tight gate [G3] placed around the expected location of the ground-state peak can bias the correlation data set with events where the target remains in its ground state. The target excitation energy spectrum for ^{27}Al is shown in Fig. 5.5(d). There are several low-lying excited states in ^{27}Al, and these can be observed as the tail in the respective spectrum, but again a gate [G4] on the large observed peak will bias in favor of the ground-state component.

An interesting feature observed in all of the reconstructed target, and target-like fragment, excitation energy spectra is the prominent ground state peak. It appears that at low to intermediate bombarding energies that small energy transfers prefer single fragment excitations. This seems to be a generic feature of these types of reactions, and was also observed for the inelastic scattering of ^{7}Be, ^{6}Li, and ^{17}Ne projectiles on ^{9}Be targets [48, 51]. This feature of the spectra can be understood from a basic probability theory standpoint if we assume that the probability of exciting the target or projectile are independent (this is clearly not a great assumption, but it elucidates the point) and are small. In this case, the probability of exciting both the target and the projectile will just be the multiplication of the independent probabilities, resulting in an even smaller probability of exciting both the projectile and target.

5.4 Differential Cross Sections

To extract differential cross sections and angular correlations it is necessary to have a complete understanding of the detector array geometry and resolution (i.e. response to ionizing radiation). As mentioned in the previous chapter, there was a Faraday cup in the experimental setup, however, it only provided relative data (it was uncalibrated). Thus,

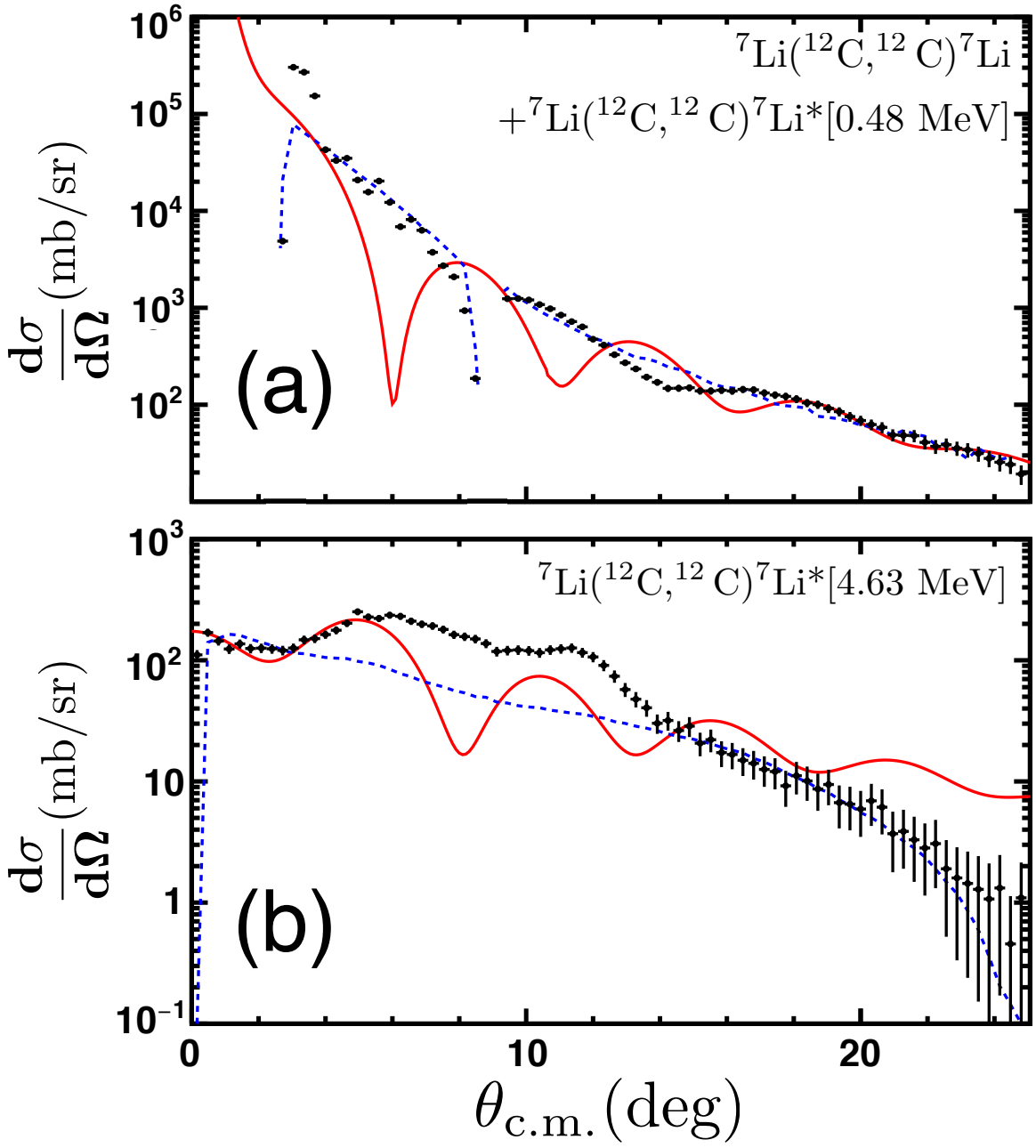

Figure 5.6: Data (black circles) and DWBA predictions (solid red lines) for the ^{7}Li + ^{12}C system: (a) elastic scattering and the single inelastic excitation of ^{7}Li to the 0.48 MeV state and (b) the single inelastic excitation of ^{7}Li to the 4.63 MeV state. The predicted angular distributions were used as inputs into the Monte Carlo simulations of the detector system and the expected detector distributions are compared to the data (blue dashed lines).

Table 5.1: Fitted optical potential parameters for the ^{7}Li + ^{12}C DWBA calculations, assuming a cluster model for ^{7}Li ($\alpha + t$). The volume terms use a Woods-Saxon form. The spin-orbit coupling uses a differential Woods-Saxon form. The asterisks show the parameters that were not varied during the fitting procedure.

System	Type	V [MeV]	r_{real} [fm]	a_{real} [fm]	W [MeV]	r_{imag} [fm]	a_{imag} [fm]
^{7}Li$-^{12}$C	Volume	169.4	1.28	0.800	34.8	1.67	0.758
	Spin-Orbit	0.550	1.48	0.727	0.720	1.48	0.485
$\alpha-^{12}$C	Volume	72.0	1.433*	0.692*	32.0	1.43*	0.692*
$t-^{12}$C	Volume	65.3	1.15	0.400	30.9	1.35	0.407
$\alpha - t$	Volume	71.6	1.20	0.736			

the relative cross section between elastic scattering and inelastic scattering of interest could be found, and the data were scaled to DWBA predictions. Furthermore, because we used the invariant-mass method to reconstruct the projectile, we were unable to determine the population of the 1$^{\text{st}}$ excited state ($J^{\pi} = 1/2^{-}$, 0.46 MeV) shown in Fig. 5.5(e)) and so the elastic scattering data will also include this component. However, DWBA calculations suggest the cross section for populating the 0.46 MeV state is several orders of magnitude lower than the elastic scattering cross section, and thus our inability to dissect the elastic from inelastic excitation to the $J^{\pi} = 1/2^{-}$ state does not significantly affect the data.

The effect of the beam misalignment and beam divergence on the scattering angle can be seen in Fig. 5.6. The input into the simulations for ^{7}Li + ^{12}C scattering (solid red lines) can be compared to the output from the Monte Carlo simulations including these effects (dashed blue lines) and the raw data (black circles).

5.4.1 Optical-Model Fits

DWBA breakup calculations (that will be outlined in the following chapter) were performed for the ^{7}Li + ^{12}C system using FRESCO [76], assuming an $\alpha + t$ cluster structure of ^{7}Li. Optical potentials are needed for the composite ^{7}Li + ^{12}C system, as well as for the $\alpha-^{12}$C, $t-^{12}$C, and $\alpha - t$ subsystems. Many of the parameters for these potentials were

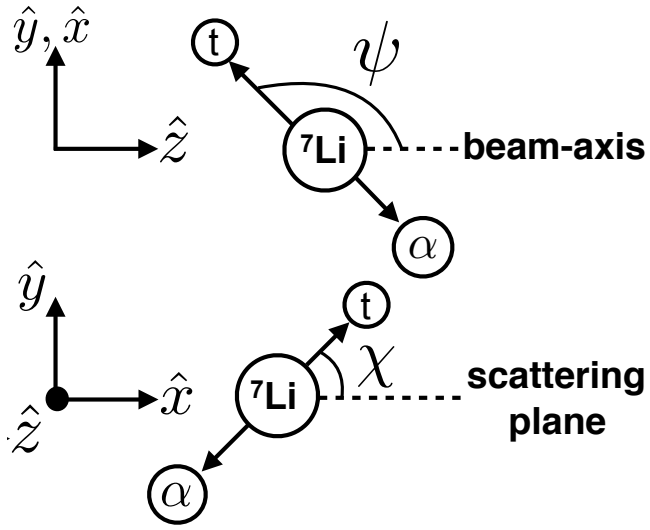

Figure 5.7: A diagram of the angles ψ and χ used for the correlations.

obtained from a fit of the relative elastic and inelastic scattering angular distributions, as well as the angular correlations for the breakup of ^{7}Li* [4.63 MeV]. Since absolute cross sections were not available, the relative cross section data (black circles in Fig. 5.6(a) and 5.6(b)) were scaled to the DWBA predictions in the fitting procedure. The volume terms for the phenomenological optical potentials are described by a Woods-Saxon form, while the spin-orbit coupling uses a differential Woods-Saxon form described by Eq. (2.8), where instead of a nucleon mass the mass of the charged pion is used. The initial $\alpha-^{12}$C effective interaction was obtained from [99] and the magnitude of the interaction was allowed to vary in fitting. The $t-^{12}$C potential was extrapolated from a ^{3}He-^{12}C effective interaction. The $\alpha - t$ and ^{7}Li-^{12}C potential parameters were allowed to vary during the fitting procedure, as well as the spin-orbit coupling of ^{7}Li. The fitted potential parameters are listed in the Table II and the resulting fits to the elastic and single inelastic excitation cross sections of ^{7}Li are shown in Fig. 5.6(a) and 5.6(b) as the solid red lines.

5.5 Extracting Magnetic Substate Populations

Because we measure the complete kinematics of the system in question, extracting the correlation angles ψ and χ is straightforward. A diagram defining the angles ψ and χ is provided in Fig. 5.7 (ψ and χ are precisely the angles θ_c and ϕ_c presented in Sec. 3.3). The correlation angle ψ is defined as the angle of the breakup with respect to the beam axis, which is also our quantization axis. The correlation angle χ is measured from the reconstructed scattering plane. The scattering plane is defined by the momentum of the beam, and final momentum of the scattered ^{7}Li. By momentum conservation, the momentum of the target is also in this plane. A major issue with correlation measurements is the limited acceptance of the detector array. If some of the particles are missed in the decay, the resulting correlations will be biased. In order to correct for this, the Monte Carlo simulations of the reactions were used to determine the experimental geometrical efficiency of the detector array.

The raw data for the correlations of ^{7}Li* breakup, after interacting with the three targets used, are shown in Fig. 5.8. There are clear features present in each of the histograms that come from the limited acceptance of the detector array. The raw correlation patterns are very similar, and there are already clear peaks at $\cos(\psi) = 90^o$ suggesting that the spin ^{7}Li* is largely aligned longitudinal to the beam axis.

5.5.1 Density Matrix Fits

The rest of the presented correlation spectra were efficiency corrected by the maps generated by the Monte Carlo simulations. These efficiency maps are shown in Fig. 5.9. Once the raw correlation data are efficiency corrected the analysis outlined in Sec. 3.3 can be directly applied. The efficiency-corrected angular correlations for the decay of ^{7}Li* projectiles, after interaction with C, Be, and Al targets, are shown in Figs. 5.10(a), (b), and (c), respectively. The resulting angular correlations are all very similar with prefered fragment emission transverse to the beam [$\cos(\psi) = 0$]. This result is consistent with the prior study

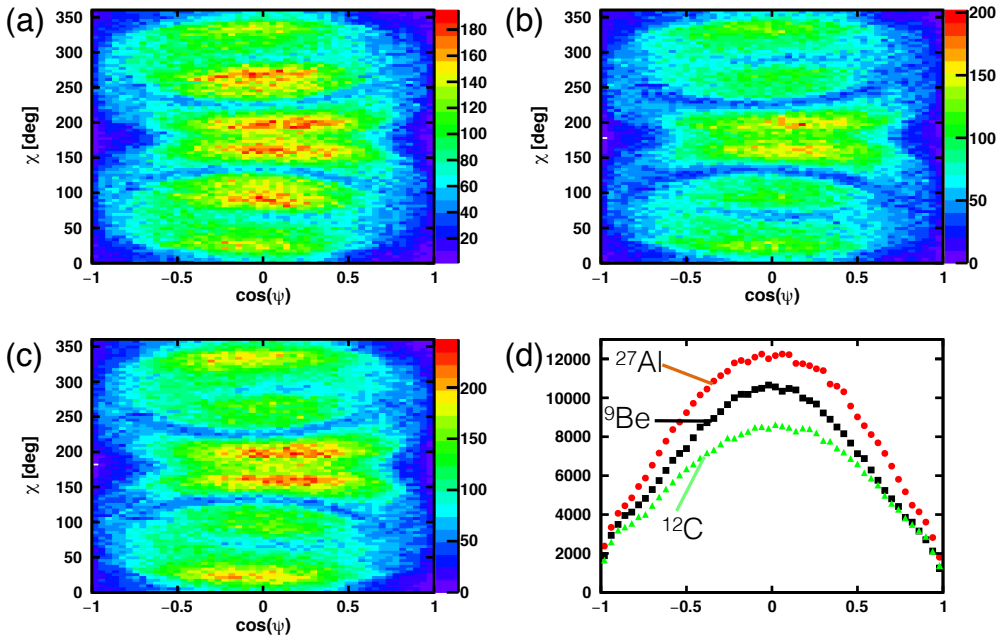

Figure 5.8: Raw data for the angular correlations of ^{7}Li* breakup after interacting with (a) ^{9}Be, (b) ^{12}C, and (c) ^{27}Al. Panel (d) shows the projections of the raw correlations on the cos(ψ) axis.

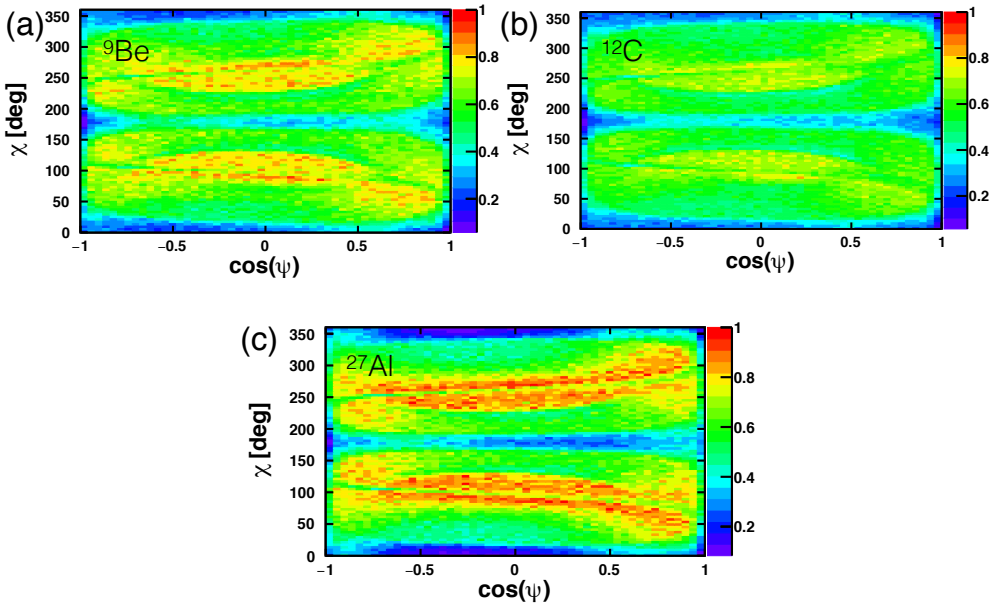

Figure 5.9: Monte Carlo efficiency maps of the detector setup for the three different targets: (a) ^{9}Be, (b)^{12}C, (c) ^{27}Al.

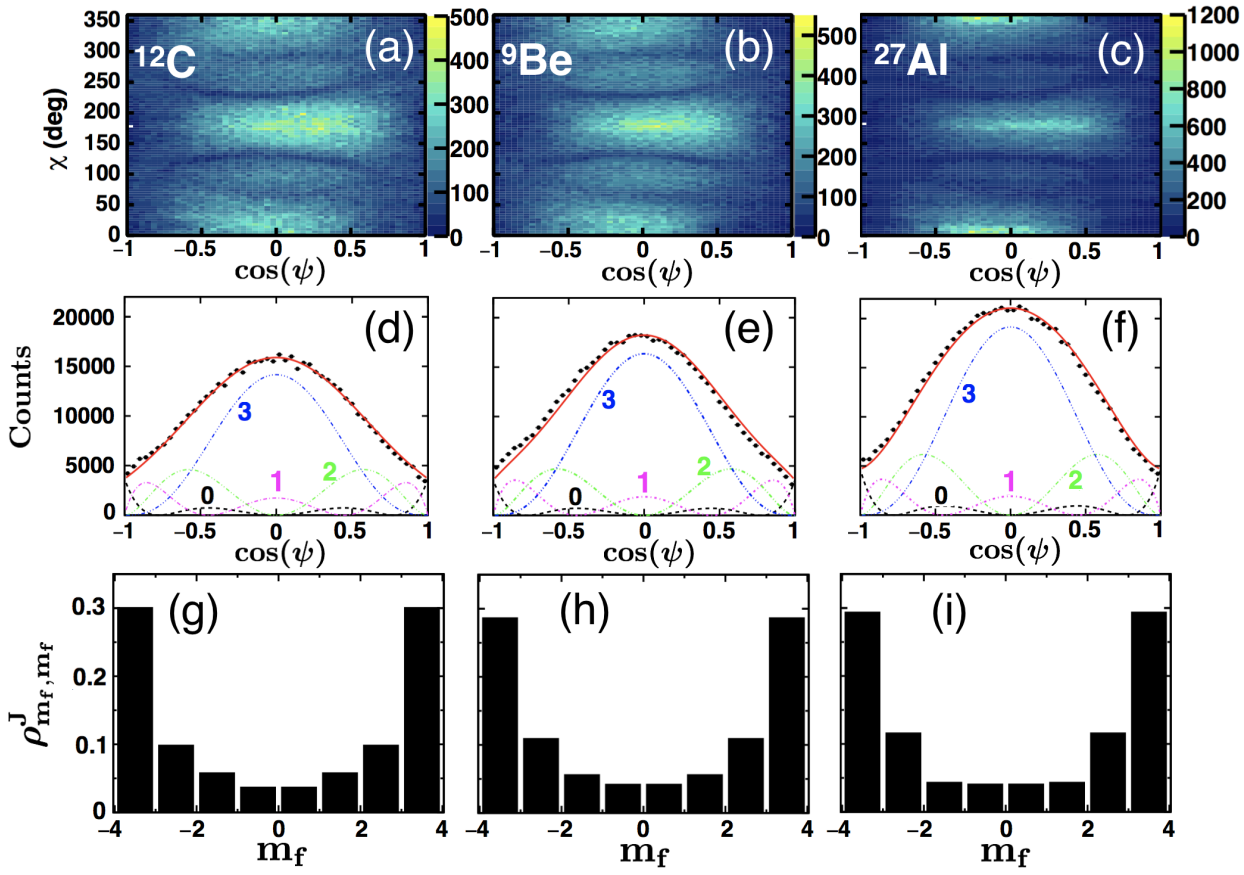

Figure 5.10: The efficiency-corrected angular correlations for the breakup of ^{7}Li* after interacting with (a) C, (b) Be, (c) and Al targets over the measured angular range; (d),(e),(f) the projections of the angular correlations onto the cos(ψ)-axis; and (g),(h),(i) the extracted magnetic-substate distributions of ^{7}Li* with the separate targets, respectively. All data have been gated on the ground-state peak of the respective target nucleus.

using a beam of ^{7}Be at $E/A = 65.5$ MeV [48], and the magnitude of alignment is extremely similar.

The projections of the angular correlations on the cos(ψ) axis are described by Eq. (3.42). The experimental spectra and squared fits to the Wigner little d matrices are shown in Figs. 5.10(d), (e), and (f). The asymmetry in the cos(ψ) distributions is likely due to imperfect energy calibrations. This was determined by introducing a small linear shift to the assigned energies of the tritons in the Monte Carlo simulations which reproduced the observed asymmetries. The magnetic-substate distributions of ^{7}Li* extracted from the angular correlations are shown in Figs. 5.10(g), (h), and (i) for the three targets.

For ^{7}Li* inelastically excited to the $J^\pi = 7/2^-$ state, the magnitude of alignment was found to be $\mathcal{A} = 0.49(1), 0.53(1), 0.53(1)$ after scattering off C, Be, and Al nuclei, respectively. This magnitude of alignment for ^{7}Li* is quite large compared to other types of reactions at similar energies. The similarity of the alignment found for ^{7}Li in this work, for each target, also requires an explanation and this is provided in the following chapter.

5.6 Sources of Error

Si-CsI(Tl) telescopes provide reasonable energy resolution of charged-particle fragments resulting from nuclear reactions. Si detectors typically have good energy resolution ($\sim$ 50 keV FWHM), while CsI(Tl) have worse energy resolution ($\sim$ 200 keV FWHM). The energy resolution for the Si detectors is largely from electronic sources (e.g. thermal noise), while the resolution for the CsI(Tl) largely comes from optical sources (e.g. photodiode/PMT noise, non-linear energy to light conversion, and/or non-uniform light collection). There is also an error associated with the polar scattering angle, that depends on the size of the segments on the Si detector, and the distance of the detector from the target. The distances to the target are known within $\pm$2 mm, and the size of the rings on the upstream telescope is 0.86 mm, while the size of the rings on the downstream telescope is 0.5 mm. These errors combine to a polar angle resolution of $\sim 0.5^o$ for the upstream telescope, and a resolution of $\sim 0.1^o$ for the downstream telescope in the laboratory frame. The azimuthal scattering angle error is dominated by the size of the pie sections of the Si detectors. The resolution of the azimuthal angle for the upstream telescope is $\sim 3^o$, and for the downstream telescope is $\sim 11^o$. The uncertainties on the scattering angle do significantly affect the invariant-mass reconstruction of ^{7}Li, as shown in Fig. 4.3. The largest sources of error for the scattering angle turned out to be the misalignment of the detector axis with the beam axis, and the overall beam divergence. These features of the beam severely limited the scattering-angle precision. However, this lack of precision has little effect on resulting invariant-mass reconstructions, which are largely dependent on the relative angle of the decay. The finite

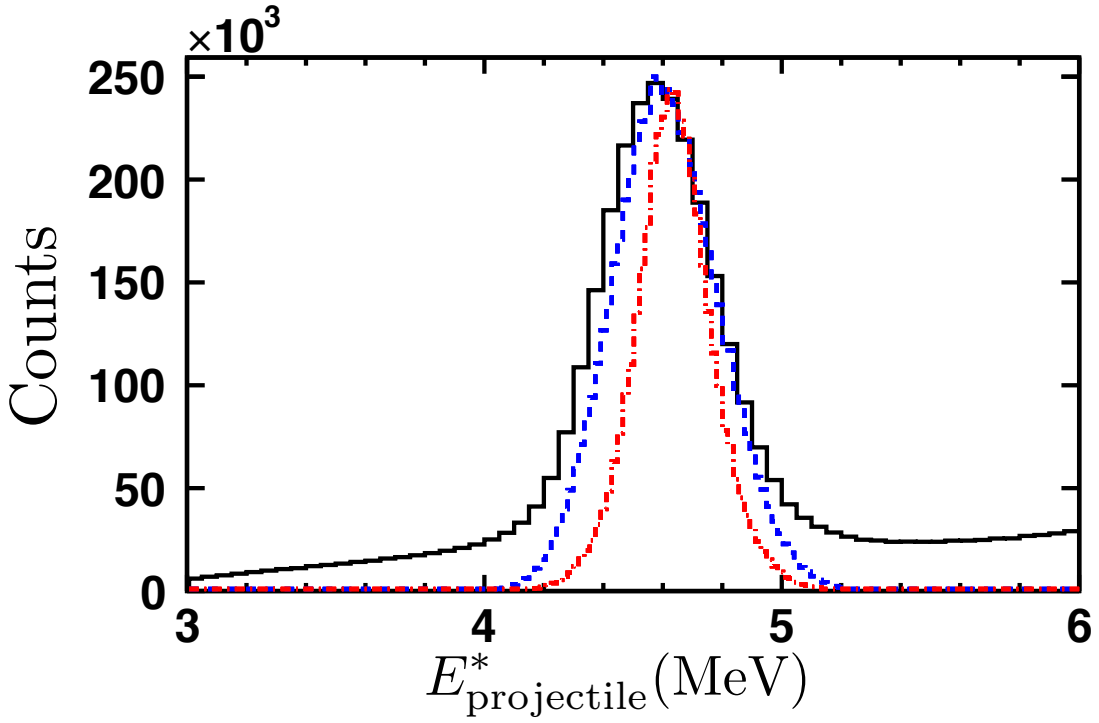

Figure 5.11: The invariant-mass spectrum for $\alpha + t$ events showing particle-unbound states in ^{7}Li is shown again (solid black line). The predicted width of the 4.63-MeV resonance from the Monte Carlo simulations assuming perfect energy calibrations for the tritons is shown as the red dash-dot line. The expected width of the 4.63 MeV resonance by introducing a linear shift to the triton calibrations is shown as the blue dashed line.

size of the beam interaction with the target also has to be accounted for, as well as the associated energy losses of the projectile and projectile fragments in the target. The result of all these effects (specifically the precision in scattering angle) is quite apparent in the measured differential cross sections shown in Fig. 5.6.

For the resolution of the invariant-mass spectra of ^{8}Be and ^{6}Li, shown in Figs. 5.3 and 5.2, the main contribution was the scattering-angle resolution. This is demonstrated by the reproduction of the measured widths for these two nuclei by the Monte Carlo simulations. For the invariant-mass spectrum for ^{7}Li, the red dot-dashed line in Fig. 5.11 shows the predicted width assuming perfect energy calibrations for the tritons. This width is much smaller than the observed width, which can be almost fully explained by introducing a linear shift to the triton energy calibrations in the Monte Carlo simulations, shown as the blue dashed line.

Table 5.2: The contribution to width of the measured ^{7}Li* lineshape as determined from Monte Carlo simulations. The major contribution to the resolutions was the angular resolution of the Si detectors ($\sim$ 160 keV), however, the intrinsic CsI pulse-width resolution also contributed significantly ($\sim$ 90 keV). A linear shift to the triton energies in the Monte Carlo simulations was required to produce the measured width of the distribution.

Source of Error	FWHM of lineshape [keV]
Si Angle Error	161
CsI(Tl) Resolution	92
Target Thickness	39
Beam Divergence	< 1
Off-Axis Beam	< 1
All effects	280
All effects with triton calibration energy shift	400
Measured	410

This discrepancy shows the importance of obtaining good calibrations for the particles of interest during the experiment. For the case of triton events, this is difficult since tritium beams are not typically provided for a variety of reasons.

The remaining contributions to the width in the invariant-mass spectrum of ^{7}Li is shown in Table 5.2. The effect of each source of error was determined by removing all effects except the one of interest in the Monte Carlo simulations. From Table 5.2 it is clear the angular resolution of the Si detector system had the most significant contribution to the overall width, followed by the inherent CsI(Tl) resolution. The CsI(Tl) resolution was modeled by a Gaussian with $\sigma = \sqrt{E} \cdot (0.085)$, where the $\sqrt{E}$ takes into account the statistical error from photon counting of the scintillation while the intrinsic resolution of the CsI(Tl), as well as light collection effects, are taken into account by the factor of 0.085. This formula produces percent errors of the energy on the order of 0.1%, which is consistent with more detailed studies of CsI(Tl) detector resolutions. [100].

Also of some importance were the energy losses of the fragments in the target. Since the position of the decay within the target is not fully constrained, the total amount of energy lost is not perfectly known. For particles of significantly different charge and mass this can

give rise to a larger differential energy loss, resulting in degraded invariant-mass resolution.

In summary, the Si angle resolution and lack of triton calibration were the leading factors in degrading the invariant-mass resolution. The Si-angle error could have been reduced by using a detector array with much better angle resolution. Micron semiconductor now provides an annular segmented Si with a similar areal size to a design TTT detector, that also has 128x128 segments, called the S4. The experiment at Texas A&M would have benefited from a design S4, not only for the improved invariant-mass resolution, but it would have provided enough solid angle coverage to justify using only one telescope, greatly easing setup. Furthermore, if a triton calibration beam had been provided the error due to triton calibrations mitigated, the invariant-mass resolution would be improved by a factor one and a half. If an S4 Si detector was also used, the invariant-mass resolution would be over a factor of two better. However, the final resolution was quite adequate for determining the resulting spin alignment, the goal of this dissertation.

Chapter 6

Polarization Phenomena in Nuclear Reactions

"I think I can safely say that nobody understands quantum mechanics."

—Richard Feynman

Before discussing the reaction mechanism for generating spin alignment in inelastic nuclear reactions, it is useful to look at other nuclear reactions mechanisms that generate spin polarization or alignment. The arguments provided for the proposed reaction mechanism describing inelastic reactions stem from similar principles for other nuclear reactions. The reaction mechanisms for the processes of fusion, deep inelastic collisions, projectile fragmentation, and Coulomb excitation are discussed before moving into the discussion of spin alignment generated in inelastic nuclear reactions.

6.1 Fusion

At reaction angular momenta below L_{crit}, and energies near and/or above the Coulomb barrier, where the projectile nucleus is sufficiently close to the target nucleus, the projectile and target nucleus will fuse. At this stage in the process, all of the collision angular momentum is transferred to the intrinsic angular momentum (i.e. spin) in the excited composite system formed in the collision. If the angular momentum barrier is shallow for the result-

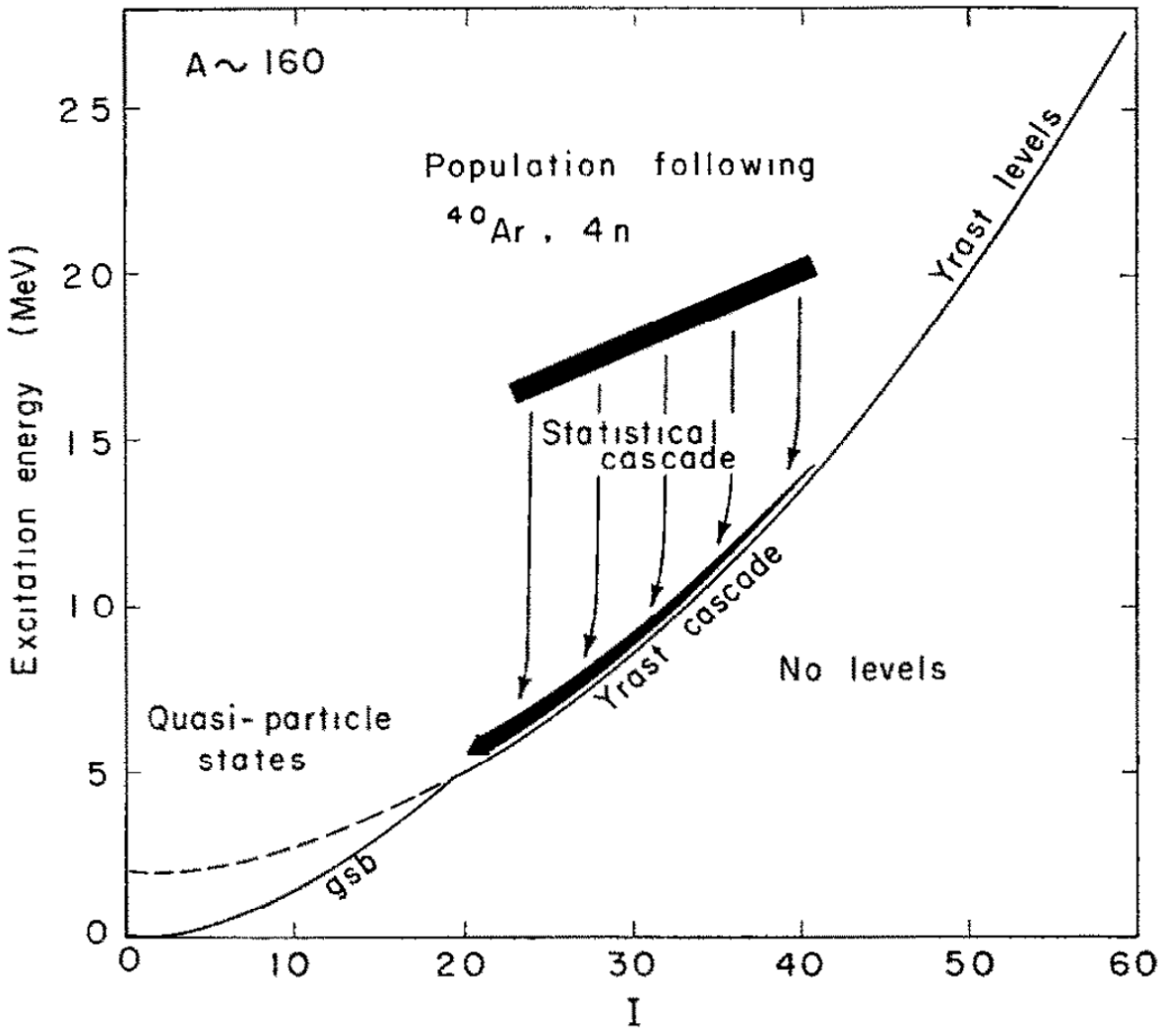

Figure 6.1: Figure 1 from Ref. [101], which shows the scheme for a statiscal cascade of particle evaporation before reaching the yrast line of the evaporation residude, which then γ-decay cascades to the ground state.

ing nucleus then it will fall back apart into two fragments, with this process referred to as qausi-fission. Otherwise a compound nucleus is formed after the system equilibrates and has a resulting alignment $\mathcal{A} = -1$. As this nucleus begins to decay, it will shed (evaporate) low mass-particles (n's, p's, and α's with the relative yields typically in that order) to carry away some of the resulting excitation energy, leaving an excited evaporation residue on the yrast line of states. The yrast states are defined as the lowest-energy levels for a given angular momentum in a nucleus. The evaporation residue will then decay by a cascade of γ-rays before reaching its ground state. This process is outlined in Fig. 6.1 for a ^{40}Ar projectile on a heavy target $A \sim 160$.

During the evaporation process, the full transverse spin alignment of the compound nucleus is diminished by the evaporation particles carrying away angular momentum. Even still, the resulting evaporation residue is heavily aligned, as evidenced from γ-ray angular distribution measurements. In the case of breakup fusion initiated by $E/A = 11$ MeV ^{7}Li on ^{159}Tb, the alignment of the resulting $^{162-x}$Dy residue from αxn reactions depends on the number evaporated neutrons (x) and was largely aligned for low particle evaporation, i.e. $\mathcal{A} \sim 0.6$ for $\alpha 2n - \alpha 4n$ reactions.

Furthermore, these γ-ray angular distributions can be used to determine the most likely spin orientation of the compound nucleus, allowing for correlation measurements with respect the spin-axis of the nucleus. This fact was utilized by the spin-spectrometer [102], which helped elucidate reaction mechanisms for compound-nucleus formation [103, 104, 105]. The evaporation residues produced in these type of reactions can be quite exotic nuclei [106], and many properties about the resulting nucleus can be determined [107, 108, 109, 110, 111].

6.2 Deep Inelastic Collisions

Deep inelastic collisions occur in heavy-ion collisions over a range of partial waves, i.e. over a range of impact parameters. The smaller the impact parameter the larger the deflection angle. This can be understood as an increase in the amount of time the two nuclei

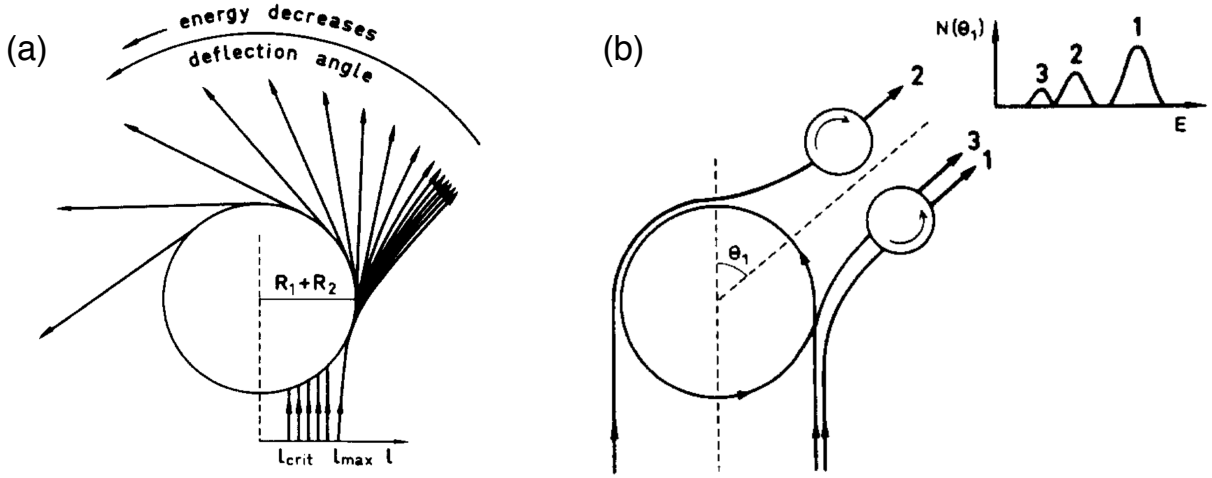

Figure 6.2: A combination of Figs. 1 and 2 in Ref. [31], showing the predicted polarization of exit-channel fragments in deep inelastic collisions at the same scattering angle and different final kinetic energies for the presented reaction mechanism.

are interacting, as depicted in Fig. 6.2(a). During this interaction the nuclei can exchange energy, and through frictional forces the total kinetic energy of the system is lost to "heat" i.e. excitations of the nuclei. This scenario is depicted in Fig. 6.2(a), where small impact parameters are shown to go to larger deflection angles and result in larger kinetic energy losses. As the projectile "orbits" around the target the frictional forces impart a torque on the PLF resulting in a transfer of collision angular momentum to intrinsic spin of the excited PLF, generating a spin polarization. Similarly the target-like fragment will also acquire a spin polarization in the same direction.

In the case of near-side scattering, scenario 1 in Fig. 6.2(b), the frictional forces impart a torque pointing out of the page, perpendicular to the reaction plane (this is by definition perpendicular to the beam axis). Since the projectile does not interact with the target for a substantial amount of time, there is not much loss of total kinetic energy. Thus at a given scattering angle, this kind of scattering will have PLF's with larger energies, as indicated in the small plot of $N(\theta_1)$ versus E. Scenario 2 shows far side scattering, resulting in the same scattering angle, but now the kinetic energy is further reduced and the spin polarization points into the page, i.e. is opposite that for near-side scattering. This mechanism was confirmed by measurements of the reaction ^{40}Ar + $^{\text{nat}}$Ag, where the average

circular polarization of de-excitation γ-rays were determined [32]. These should have the same sign of polarization as the parent nucleus. When gating on deep-inelastic events (lower energy PLF's), they found that the polarization of the resulting de-excitation γ rays was consistent with far-side orbited scattering (or negative deflection angles). Scenario 3 shows a situation where the projectile almost fully orbits the target resulting in di-nuclear system.

"Sticking" phenomena similar to compound nucleus formation in fusion reactions, where the collision angular momentum is completely transferred to the compound nucleus, has also been observed for deep inelastic colissions [112]. This results in the fragments having their spin largely aligned normal to the reaction plane [44].

6.3 Projectile Fragmentation

Projectile fragmentation is a consistent source for generating longitudinal spin alignment, and also spin polarization. In this reaction, the interaction of the projectile and target shear off some of the respect nucleons, leaving only a PLF, and a target-like fragment. This type of reaction has been posed a source for generating spin polarized or aligned beams of radioactive isotopes [45].

The mechanism for this reaction is outlined in Fig. 6.3. The cross section plot on the right side of this figure shows the "Goldhaber" distributions for the PLF momentum [113]. The Goldhaber distribution gives the cross section of the process as a function of the parallel momentum distributions (along the beam axis). On the left side (low p) of the Goldhaber distribution, the PLF gets a momentum kick point opposite to the beam direction, which is imparted from the many nucleons broken off from the projectile and target. This also corresponds to an angular momentum transfer to the PLF *transverse* to the beam axis. Since this transfer is on in one direction, a polarization is generate, denoted by Fig. 6.3(a), and the alignment, $\mathcal{A}$, goes to the minimum value. The same picture works on the right side (high p) of the Goldhaber distribution, Fig. 6.3(c), but now the kick is along the beam direction resulting in the polarization in the opposite direction, corresponding to another minimum

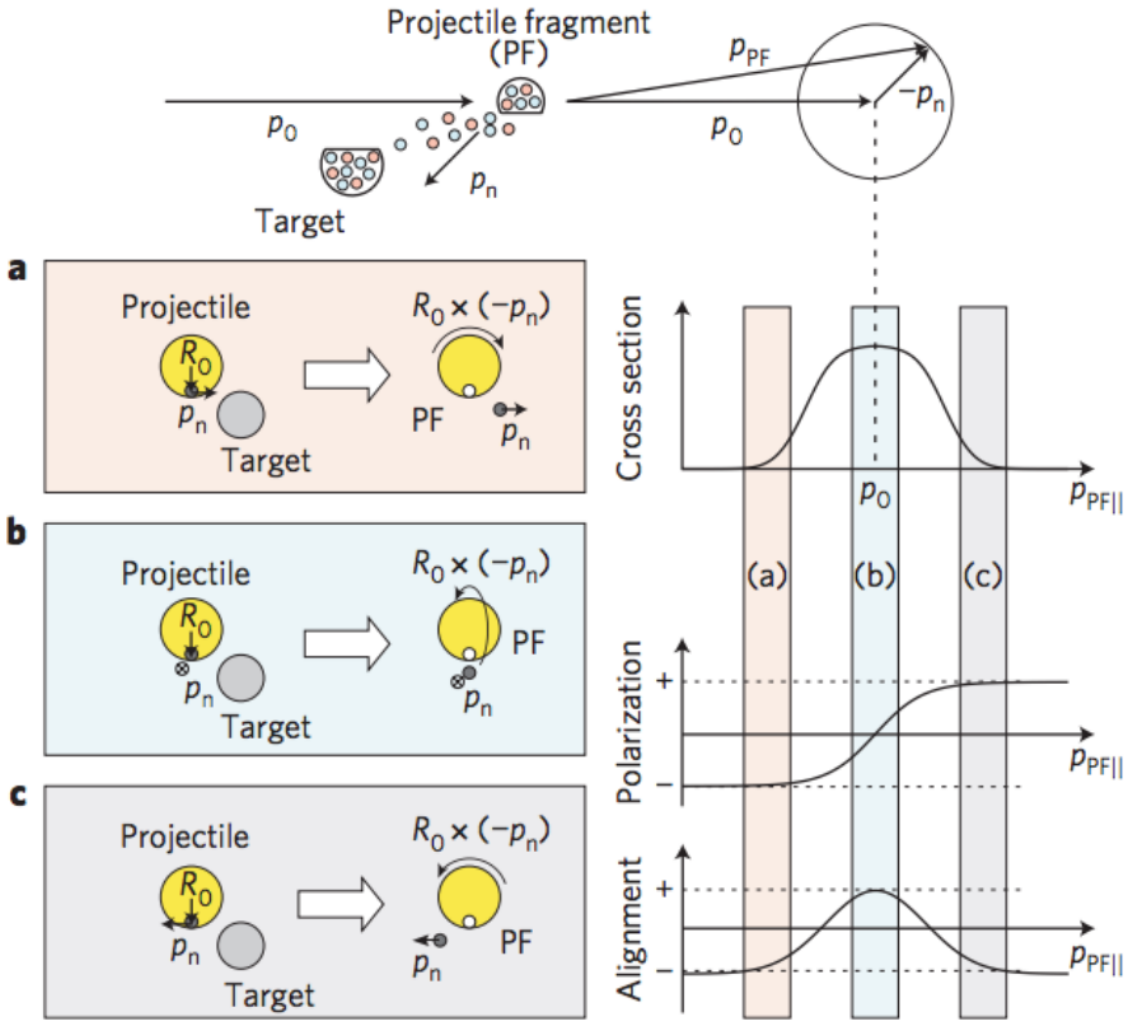

Figure 6.3: Outline of alignment and polarization mechanism in projectile fragmentation from Ref. [45].

in alignment. In the middle of the Goldhaber distribution, Fig. 6.3(b), the PLF gets a kick transverse to the beam, corresponding to an angular momentum transfer *longitudinal* to the beam. Since there is no preferred direction, this results in a net spin alignment along the beam axis. The resulting alignment from projectile fragmentation tends to be modest. The alignment of the Al isotope reported in the work that Fig. 6.3 comes from is $\mathcal{A} = 0.08$. As mentioned in the Introduction, the larget reported alignment from this class of reactions is $\mathcal{A} = 0.35$, which was generated in the population of a $J^\pi = 19/2^-$ high spin isomer in ^{43}Sc from fragmenting ^{46}Ti at 500 MeV/u.

6.4 Relativistic Coulomb Excitation

Another consistent reaction mechanism for generating large longitudinal spin alignment of excited projectiles is Coulomb excitation. This type of reaction occurs in very peripheral collisions ($b > b_{\text{graz}}$) with a high Z target and/or projectile. Although these reactions aren't strictly nuclear, i.e. the excitations do not occur due to nuclear forces (there is no overlap of nuclear densities), they still result in excited nuclei. Because the Coulomb force is well understood, unlike the strong nuclear force, calculations for these excitations are rather exact [50]. Calculations of Coulomb excitation suggest that large longitudinal alignment of excited projectiles should be generated for intermediate energy ($< \text{GeV}/A$) provided the excitation energy is sufficiently small compared to the center-of-mass kinetic energy. [114]. This generated alignment has been observed and utilized for the extraction of g-factor's [1]. Although no concrete understanding of the mechanism for this phenomenon is reported in the literature at intermediate energies, it has been suggested that the longitudinal alignment arises from Lorentz contractions of the E-field. However, this is not expected to be true.

Longitudinal alignment phenomena do arise for Coulomb excitation in ultra-relativistic regimes, where a particle passing an observer will have its electric field distribution Lorentz contracted into in a plane-perpendicular to the direction of motion and generate perpendicular magnetic fields such that it appears as a pulse of light moving along the axis of propagation [54]. This fact has been used in the equivalent photon approximation in ultra-peripheral collisions (i.e. the particles take straight-line trajectories), where the incoming projectile and target are Lorentz contracted in the center-of-mass frame to the point that they appear as two colliding photons. Ultra-peripheral heavy-ion collisions can thus give insight into photon-photon scattering cross sections [115]. In this equivalent photon picture, one can calculate the spectrum of "virtual" photons, first shown by Fermi, Weizsäcker, and Williams. If one does so for all multipolarities of photon emission, then as Bertulani and Baur say *"The impinging projectile acts like a spectrum of plane wave photons with helicity*

$m = \pm 1$." [50]. This can induce vibrations in nuclei, including the collective giant dipole resonance, and the resulting spin orientation is largely aligned along the beam axis. A giant dipole resonance excitation, that was largely spin aligned, was observed in ^{208}Pb by $\gamma - \gamma$ coincidence measurements, where ^{208}Pb was Coulomb excited via $E = 1$ GeV/A ^{209}Bi projectiles [49].

From Jackson [54], the number of "virtual" photons at a given frequency ω generated by a projectile (or target) is proportional to the charge squared. Thus, this effect will only be present for heavily charged ions at ultra-relativistic energies. The reaction of interest in this dissertation does not satisfy either of these requirements.

Furthermore, if the generation of spin alignment can be described in one particular inertial reference frame, then there must be an auxiliary solution in other inertial frames of reference, i.e. relativity tells us there is no preferred inertial reference frame. Therefore, we must construct the mechanism in a reference-frame independent way, i.e. from conservation laws of energy, momentum, and angular momentum etc. The ultra-relativistic mechanism for Coulomb excitation presented above, while it may not be immediately obvious, enforces these principles. The mechanism for generating spin alignment at intermediate energies provided in the following section also stems from such principles but in a more direct way. For example, the calculations previously cited, [114], show that the level of longitudinal alignment generated via Coulomb excitation at intermediate energies depends on the ratio of the beam energy and excitation energy of the projectile, where further increases in excitation energy at a given beam energy result in transverse alignments. This feature of the alignment is rather well explained by the kinematical argument for the proposed mechanism..

6.5 Inelastic Nuclear Reactions

While the alignment of excited nuclei generated in inelastic reactions has been measured for select systems, there was no alignment mechanism provided in the literature. This is not surprising, as the studies of spin alignment were usually focused on other properties of the

nuclei of interest. For instance, the spin alignment of single inelastic excitation of ^{12}C was measured over many energies and angles, with the purpose of correlating gross structures in alignment with resonances in the excitation function† of the reaction cross section [92, 89, 116]. Such correlations were never found, and descriptions of the alignment generated from quantum-mechanical scattering theory were qualitatively correct but lacked insight into the reaction mechanism [117]. The provided formalism of the reaction and subsequent DWBA calculations were consistent with the observed phenomena, and are explained by simple semi-classical kinematical arguments.

6.5.1 Angular Momentum Excitation Energy Matching

The longitudinal alignment arising from an angular-momentum-excitation-energy mismatch should be present in any single inelastic process X(Y,Y*)X or X(Y,Y)X*, provided the excitation energy is sufficiently small compared the beam energy. A change in intrinsic spin must be accommodated for by one or more different processes: a change between the incoming and outgoing orbital angular momenta (either a reduction in magnitude or tilting [89, 95]), a coupling of the fragment spins and the incoming orbital momentum (i.e. spin-orbit effects [118]), or some other spin-spin interaction.

For sufficiently large energies, the mechanism for generating longitudinal spin alignment can be understood classically, where a loss of center-of-mass kinetic energy directly corresponds to a change in magnitude of the reaction orbital angular momentum, ΔL, assuming a fixed radius of interaction, R. Repeating the analysis in Ref. [95], an upper limit on the possible transfer of reaction orbital angular momentum can be found by assuming $\mathbf{p}_{\text{in}}, \mathbf{p}_{\text{out}} \perp \mathbf{R}$. This gives the Newtonian result,

$$\Delta L = R\sqrt{2\mu E_{\text{c.m.}}}\left(1 - \sqrt{1 - \frac{E^*}{E_{\text{c.m.}}}}\right), \tag{6.1}$$

where μ is the reduced mass of the system, and $E_{\text{c.m.}}$ is the kinetic energy in the center-of-

†This means that the quantity is measured over many different bombarding energies.

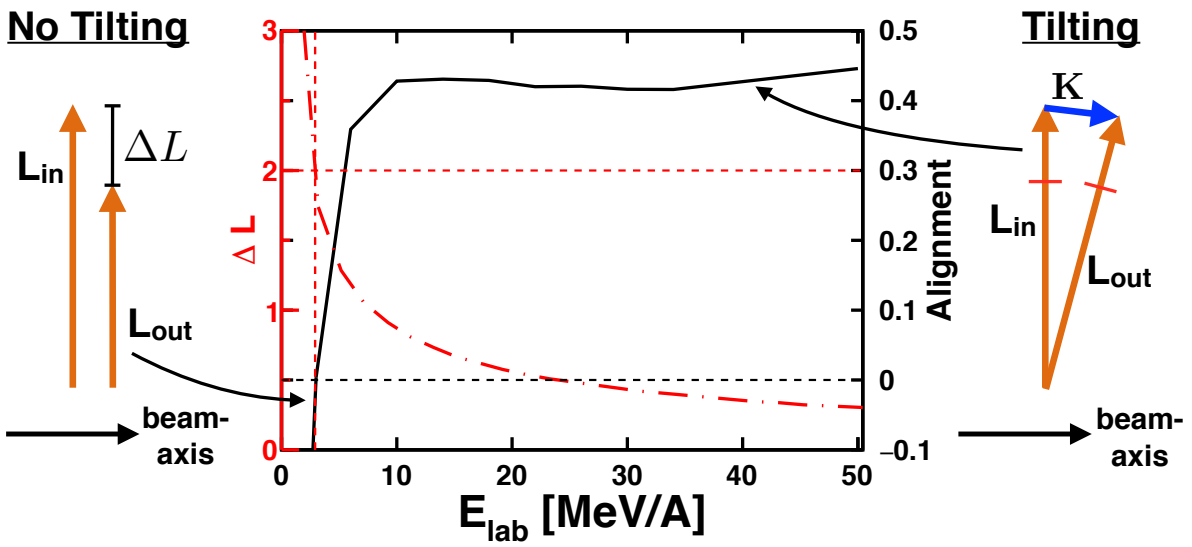

Figure 6.4: Equation (6.1) is plotted for $E^* = 4.6$ MeV and R = 5 fm (red dot-dash line). The predicted alignment from the cluster-model calculations in the angular range $5^o < \theta_{\text{c.m.}} < 15^o$ as a function of beam energy is also shown (black solid line). When $\Delta L = 2\hbar$ is allowed, the alignment disappears completely ($A = 0$) corresponding to no-tilting (left). For larger energies only tilting is allowed (right).

mass frame. Applying this equation to the studied ^{7}Li + ^{12}C system by using an excitation energy of $E^* = 4.63$ MeV, a beam energy of $E/A = 24.0$ MeV, and a radius of $R = 5$ fm, one finds $\Delta L < 1\hbar$. This means a change in magnitude of the reaction orbital angular momentum alone cannot excite ^{7}Li to the 4.63 MeV state, as the excitation requires a change in intrinsic spin of $2\hbar$. Figure 6.4 shows Eq. (6.1) with these parameters plotted as a function of beam energy. When the center-of-mass energy is much larger than the excitation energy, $E_{\text{c.m.}} \gg E^*$, L must tilt in order to conserve angular momentum when there is a change in spin of the reactant (in the absence of a spin flip of either reactant). As a result, the final reaction angular momentum is likely to have a finite projection, M, on the beam axis. This argument for an angular-momentum-excitation-energy mismatch suggests this phenomenon is a threshold effect. As one increases the beam energy (i.e. $E_{\text{c.m.}}$), the mismatch becomes greater. A sketch of non-tilting solutions (left inset) and titling solutions (right inset) are also shown in Fig. 6.4.

6.5.2 Properties of the DWBA Transition Amplitude

In order to probe the connection between the final projection of L and the inelastic excitation, it is useful to look at the transition amplitude, or T matrix, which gives the probability of going from an initial magnetic substate, m_i, to a final magnetic substate, m_f. Ultimately, it will be shown that the final projection of L is related to the change in fragment spin by $M = m_f - m_i$. By integrating the squared T matrix over a given angular region (and summing over the initial magnetic substates because the beam is unpolarized), one can predict the final outcome of the magnetic-substate distribution for an exit-channel fragment in the reaction.

To construct the T matrix for the inelastic processes of interest, we assume a general form for the projectile–target interaction. It should be able to induce multipolar excitations of the projectile by coupling the projectile–target relative motion, described with the vector $\mathbf{R}$, with the internal degrees of freedom of the projectile, described with some intrinsic coordinate $\boldsymbol{\xi}$. The interaction

$$\begin{aligned}\Delta(\mathbf{R},\boldsymbol{\xi}) = 4\pi \sum_K \frac{(-1)^K}{\sqrt{2K+1}} \\ \times \Delta_K(R,\xi)\left[Y^K(\hat{\xi})Y^K(\hat{R})\right]^0_0\end{aligned} \tag{6.2}$$

satisfies the above requirement and is rotationally invariant. The square brackets denote angular momentum coupling, where $[Y^{p_1}Y^{p_2}]^P_{M_P} = \sum_{m_1,m_2}\langle p_1 m_1 p_2 m_2|PM_P\rangle Y^{p_1}_{m_1}Y^{p_2}_{m_2}$. The requirement that $P = 0$ and $M_P = 0$ generates a scalar that only depends on the angle between $\boldsymbol{\xi}$ and $\mathbf{R}$. The actual form of the Δ functions will depend on the case under consideration and, more specifically, on the model used to describe inelastic excitation.

Focusing on breakup experiments, the population of the particle-unbound resonance is described as an inelastic excitation of the fragment-core system in terms of the relative coordinate $\mathbf{r}$. This can be easily extended to cluster-model calculations, provided the fragment is treated as a nucleus instead of a nucleon. We define the model interaction (using $p-t$, $f-t$,

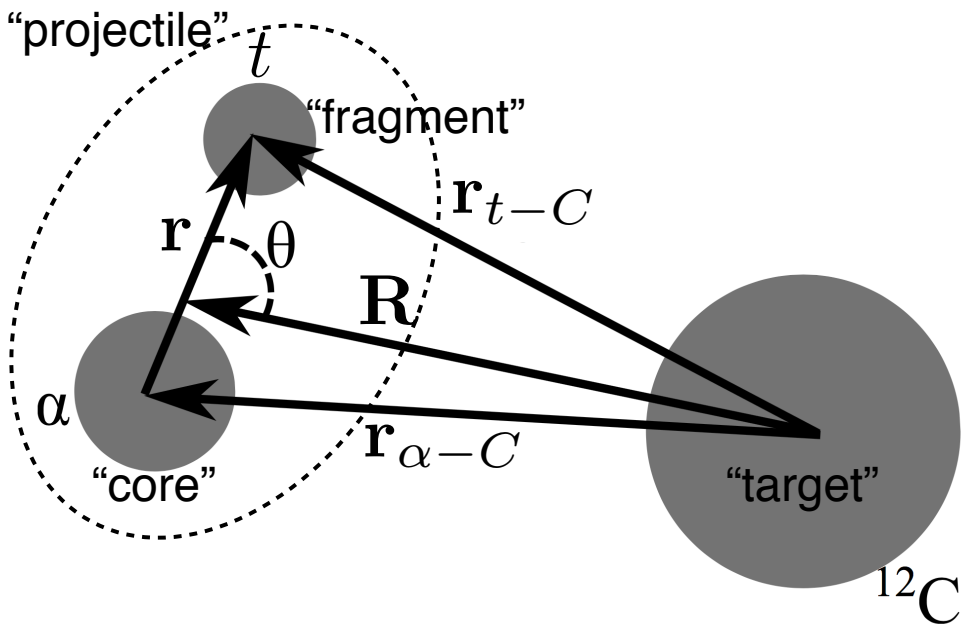

Figure 6.5: The coordinates **r** and **R** as well as the fragment-target and core-target coordinates for the ^{7}Li $+^{12}$C system.

and $c-t$ as projectile-target, fragment-target, and core-target, respectively),

$$\Delta(R, r_{c-t}, r_{f-t}) = U_{p-t}(R) - U_{c-t}(r_{c-t}) - U_{f-t}(r_{f-t}), \tag{6.3}$$

where these effective interactions are taken as central phenomenological optical potentials. This transition potential can be cast into the general form of Eq. (6.2),

$$\begin{aligned}\Delta(R, r_{c-t}, r_{f-t}) &= \sum_K \Delta_K(R, r) P_K(\theta) \\ &= 4\pi \sum_K \frac{(-1)^K}{\sqrt{2K+1}} \\ &\times \Delta_K(R, r) \left[Y^K(\hat{r}) Y^K(\hat{R}) \right]_0^0,\end{aligned} \tag{6.4}$$

where θ is the angle between **r** and **R** (diagrammed in Fig. 6.5), $P_K(\theta)$ are the Legendre polynomials. The multipole components $\Delta_K(R, r)$ can be computed from the interaction

Eq. (6.3),

$$\Delta_K(R,r) = \frac{2K+1}{2}\int_0^\pi \Delta(R, r_{c-t}, r_{f-t}) P_K(\theta)\sin\theta\, d\theta. \tag{6.5}$$

The population of the resonance is modeled as a direct, one–step inelastic excitation of the fragment–core system. The cross section is proportional to the squared modulus of the transition amplitude T_{m_i,m_f}, which is calculated in the distorted-wave Born approximation (DWBA).

The distorted waves describing the relative projectile-target motion in the initial ($\chi_{i,m_i}(\mathbf{R},\mathbf{k}_i)$) and final ($\chi_{f,m_f}(\mathbf{R},\mathbf{k}_f)$) channels are solutions of the phenomenological central optical potential $U_{p-t}(R)$ used in Eq. (6.3). Note that, in order to avoid complications inherent in the treatment of the continuum, the final particle-unbound state is modeled with a very weakly bound wavefunction (quasi–bound approximation). With these ingredients the T matrix is

$$\begin{aligned} T_{m_i,m_f} = \int \chi_f^{(-)*}(\mathbf{R},\mathbf{k}_i)\phi^*_{f,m_f}(\mathbf{r})\Delta(R, r_{c-t}, r_{f-t}) \\ \times\chi_i^{(+)}(\mathbf{R},\mathbf{k}_f)\phi_{i,m_i}(\mathbf{r})\, d\mathbf{r}\, d\mathbf{R}, \end{aligned} \tag{6.6}$$

and the differential cross section for a specific $m_i \to m_f$ transition is

$$\frac{d\sigma}{d\Omega}(\theta_{\text{c.m.}}; m_i, m_f) = \frac{k_f}{k_i}\frac{\mu^2}{4\pi^2\hbar^4}|T_{m_i,m_f}|^2. \tag{6.7}$$

In the last expression, $\theta_{\text{c.m.}}$ is the scattering angle in the center-of-mass frame. For the sake of numerical computation, but also in order to gain further insight, it is convenient to work out the partial wave analysis of Eq. (6.6). We thus write down the standard expressions of the scattering and bound wavefunctions in terms of a spherical harmonics series,

$$\begin{aligned} \chi_i^{(+)}(\mathbf{R};\mathbf{k}_i) = \frac{4\pi}{k_i R}\sum_{L_i} i^{L_i} e^{i\sigma_i^{L_i}} f_{L_i}(R)\sqrt{2L_i+1} \\ \times\left[Y^{L_i}(\hat{R})Y^{L_i}(\hat{k}_i)\right]_0^0, \end{aligned} \tag{6.8}$$

$$\chi_f^{(-)*}(\mathbf{R};\mathbf{k}_f) = \frac{4\pi}{k_f R}\sum_{L_f} i^{-L_f} e^{i\sigma_f^{L_f}} g_{L_f}(R)\sqrt{2L_f+1} \times \left[Y^{L_f}(\hat{R})Y^{L_f}(\hat{k}_f)\right]_0^0, \tag{6.9}$$

$$\phi_{i,m_i}(\mathbf{r}) = u_i(r)\sum_{\mu_i,m_{\rm frag}} \langle \ell_i\ \mu_i\ J_{\rm frag}\ m_{\rm frag}|J_i\ m_i\rangle \times Y_{\mu_i}^{\ell_i}(\hat{r})\Xi_{m_s}(\sigma), \tag{6.10}$$

$$\phi_{f,m_f}(\mathbf{r}) = u_f(r)\sum_{\mu_f,m_{\rm frag}} \langle \ell_f\ \mu_f\ J_{\rm frag}\ m_{\rm frag}|J_f\ m_f\rangle \times Y_{\mu_f}^{\ell_f}(\hat{r})\Xi_{m_s}(\sigma). \tag{6.11}$$

The radial wavefunctions $u_i(r)$ and $u_f(r)$ are computed with a simple Woods–Saxon potential which reproduces the particle-emission threshold. The functions $f_{L_i}(R)$ and $g_{L_f}(R)$ are the solutions of the radial Schrödinger equation for the potential $U_{p-t}(R)$ in the initial and final channel respectively, and $\sigma_i^{L_i}, \sigma_f^{L_f}$ are the corresponding Coulomb phase shifts. The spinors $\Xi_{m_s}(\sigma)$ describe the spin degrees of freedom. Since all the interactions we are considering are spin–independent, the spin projection $m_{\rm frag}$ remains unchanged during the collision process, while the employed version of Δ and the partial wave expansion enforces angular-momentum conservation. We define the transition density for a multipolarity K,

$$\rho_K(R) = \int u_i(r)\, u_f(r)\Delta_K(R,r)r^2\, dr. \tag{6.12}$$

Using Eqs. (6.8)–(6.12) in Eq. (6.6), and after some algebra, we obtain

$$T_{m_i,m_f} = \sum_{K,L_i,L_f} \langle L_i\ 0\ K\ M|L_f\ M\rangle \times \langle J_i\ m_i\ K\ M|J_f\ m_f\rangle Y_{-M}^{L_f}(\hat{k}_f) I(K,L_i,L_f), \tag{6.13}$$

with $I(K, L_i, L_f)$ defined as,

$$\begin{aligned} I(K, L_i, L_f) &= 2\pi^{1/2} i^{L_i - L_f} e^{i(\sigma_i^{L_i} + \sigma_i^{L_f})} \\ &\times (2L_i + 1)^{3/2}(2K + 1)(2\ell_i + 1) \\ &\times \sqrt{(2J_i + 1)(2\ell_f + 1)} \begin{Bmatrix} \ell_i & J_{\text{frag}} & J_i \\ J_f & K & \ell_f \end{Bmatrix} \\ &\times \langle L_i\ 0\ K\ 0 | L_f\ 0\rangle \langle \ell_i\ 0\ K\ 0 | \ell_f\ 0\rangle, \\ &\times \int f_{L_i}(R)\, g_{L_f}(R) \rho_K(R)\, dR. \end{aligned} \tag{6.14}$$

If the beam energy and/or the reduced mass of the colliding systems is large, the process is rather well localized in space. Due to the absorptive nature of the optical potential, the main contribution to the inelastic process comes from the nuclear surfaces (peripheral collisions). In this situation, the partial waves contributing to the cross section are large compared to the multipolarity of the transition, and are narrowly peaked around the grazing angular momentum, $L_{\text{graz}} \gg K$. Above the grazing angular momentum, the partial wave contribution to the total reaction cross sections drops steeply.

Assuming there is one dominant multipolarity, K', and if only processes where $L_i = L_f$ are considered (employing the angular-momentum-excitation-energy matching argument) we can take advantage of the fact that as $L \to \infty$ the first Clebsch-Gordan coefficient in Eq. (6.13) is independent of L. Since only L around L_{graz}, which is large at intermediate energies, will contribute to the cross section, the Clebsch-Gordan coefficents in Eq. (6.13) can be factored out resulting in the expression,

$$\begin{aligned} T_{m_i, m_f} \approx \langle L_{\text{graz}}\ 0\ K'\ M | L_{\text{graz}}\ M\rangle\ \langle J_i\ m_i\ K'\ M | J_f\ m_f\rangle \\ \times \sum_L Y^L_{-M}(\hat{k}_f) I(K', L, L). \end{aligned} \tag{6.15}$$

The angle dependence and implicit energy dependence of the T matrix is represented in the

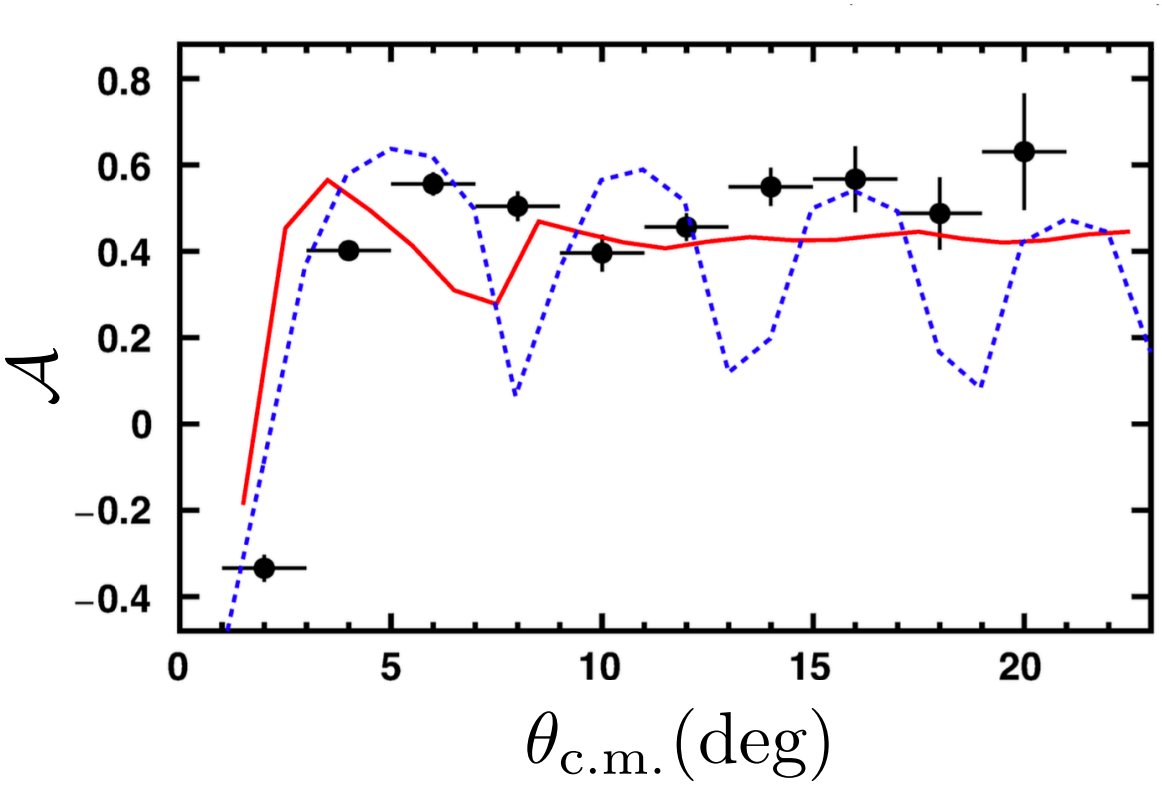

Figure 6.6: The measurements of spin alignment of ^{7}Li*[4.6 MeV] as a function of scattering angle are shown as the black circles. A DWBA calculation using all of the relevant partial waves is shown as the red solid line. A DWBA calculation for a single $\mathcal{J} = 35.5$ is shown as the blue dashed line.

sum over L in Eq. (6.15).

Oscillations in alignment with angle are expected from the high-order spherical harmonics required for the target-projectile motion in the wavefunction, although, at larger angles the alignment should become fairly constant. This is due to the mixing of several L waves about L_{graz}, which is taken into account by the sum, $\sum_L Y^L_{-M}(\hat{k_f})I(K', L, L)$, in Eq. (6.15). If the angle dependence of the T matrix is integrated over (i.e. angle averaged), then the magnetic-substate distribution of inelastically excited species should show large longitudinal alignment at beam energies above the mismatch threshold, when the reaction partner remains in its ground state. In fact, the observed alignment should be very similar to the Clebsch-Gordan coefficents presented in Eq. (6.15).

The effect on L wave mixing on the observed alignment mechanism was demonstrated

by comparing measurements of ^{7}Li* spin alignment with respect to scattering angle to the presented DWBA calculations [95], with the data shown in Fig. 6.6 as the black circles. The blue dashed line shows the DWBA calculations for a single $\mathcal{J} = 35.5$. For a single/few partial waves there are large oscillations in the observed alignment. The red solid line corresponds to DWBA calculations with all of the relevant partial waves, showing the smoothing of the alignment as a function of angle for angles well above the grazing angle. .

6.5.3 Spin-Orbit Effects on Alignment

When spin-orbit effects are introduced to the effective potential, spin-flip processes become possible. These spin-flips are accompanied by a tilt of the orbit between the projectile and target [118]. This spin-orbit tilting can potentially diminish or destroy the overall alignment generated from an angular-momentum-excitation-energy mismatch. This should be a miniscule effect due to the typically small coupling strength of the spin-orbit potential. However, small spin-orbit couplings can have a large effect on the resulting angular correlations. Figure 6.7(a) shows the predicted $\psi - \chi$ correlations from a DWBA cluster-model calculation for inelastically excited ^{7}Li* [4.63 MeV] after interacting with a ^{12}C target, at a beam energy of $E/A = 24$ MeV, with no spin-orbit potential (in the angular range of $3^{o} < \theta_{\mathrm{c.m.}} < 23^{o}$). The pattern of the calculated correlations is very similar to the data [Fig. 6.7(e)] although the centroid of the central ridge is shifted to negative $\cos(\psi)$ values, as opposed to the positive values in the experiment. It was found that the the inclusion of a small complex spin-orbit coupling for the projectile resulted in an angular correlation pattern [Fig. 6.7(b)] much more consistent with the data. Small spin-orbit couplings do not affect the alignment (i.e. the magnetic-substate distribution). Increasing the real spin-orbit coupling strength to $V_{SO} = 3.0$ MeV distorts the angular correlations but also preserves the alignment [Fig. 6.7(c)]. The angular correlations, and differential cross sections, are even more sensitive to further increases of the complex spin-orbit strength. Figure 6.7(d) shows the predicted correlations with $W_{SO} = 1.44$ MeV, at which point the pattern of the corre-

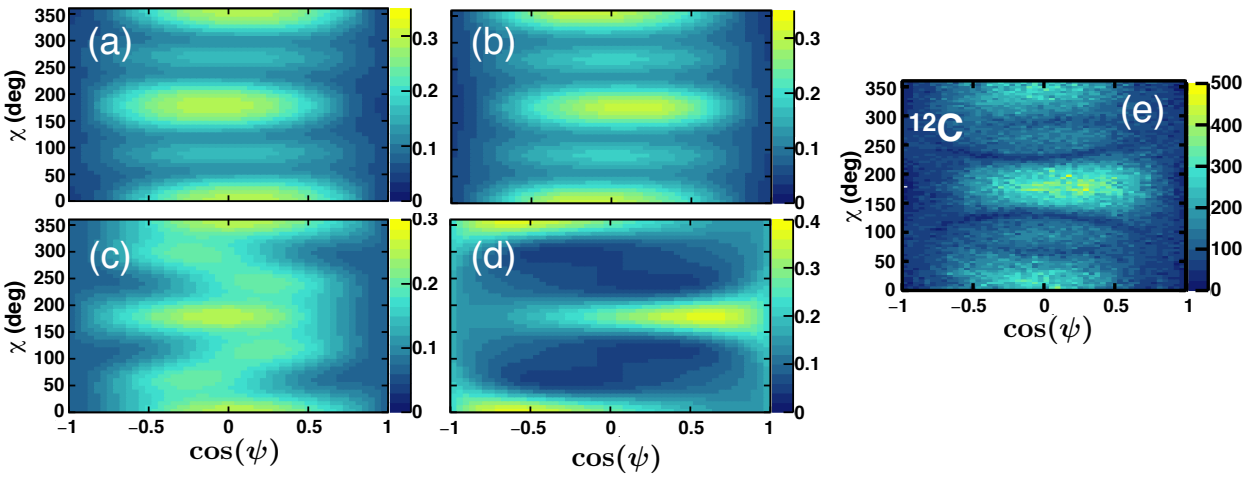

Figure 6.7: Angular correlations from DWBA cluster-model calculations of ^{7}Li* [4.63 MeV] breakup after interaction with a ^{12}C target, which remains in its ground state, with : (a) no spin-orbit term, (b) $V_{SO} = 0.55$ and $W_{SO} = 0.72$ MeV, (c) $V_{SO} = 3.0$ MeV and $W_{SO} = 0.72$, and (d) $V_{SO} = 0.55$ MeV and $W_{SO} = 1.44$. (e) For comparison, the measured angular correlations for the breakup of ^{7}Li* after interacting with the ^{12}C target.

lations is completely distorted and the longitudinal alignment is destroyed. In fact, larger increases of W_{SO} result in spin alignment transverse to the beam axis. This study suggests that angular correlation measurements, in concordance with differential cross section data, can put a constraint on the strength of spin-orbit effects in reactions. These constraints are analogous to those made by analyzing power measurements [24]. However, these alignment effects do not require a polarized beam.

6.5.4 Other Cases for Large Longitudinal Spin Alignment

Large longitudinal spin alignments were observed in the inelastic excitation of ^{7}Be and ^{6}Li to particle-decaying states [48]. ^{6}Li is modeled well by an $\alpha + d$, and ^{7}Be by an α+^{3}He, cluster structure, so the manifestation of this alignment mechanism in the cluster-model directly applies to these nuclei. Another example for this large longitudinal spin alignment is the inelastic excitation of ^{17}Ne to the 1.76 MeV state ($J^{\pi} = 5/2^{-}$), which subsequently $2p$ decays to ^{15}O. The decay is purely sequential, and in the first step, ^{17}Ne decays directly to the ground state of ^{16}F ($J^{\pi} = 0^{-}$) [119]. At sufficiently high beam-energies, the first proton is preferentially emitted perpendicular to the beam-axis indicating large longitudinal

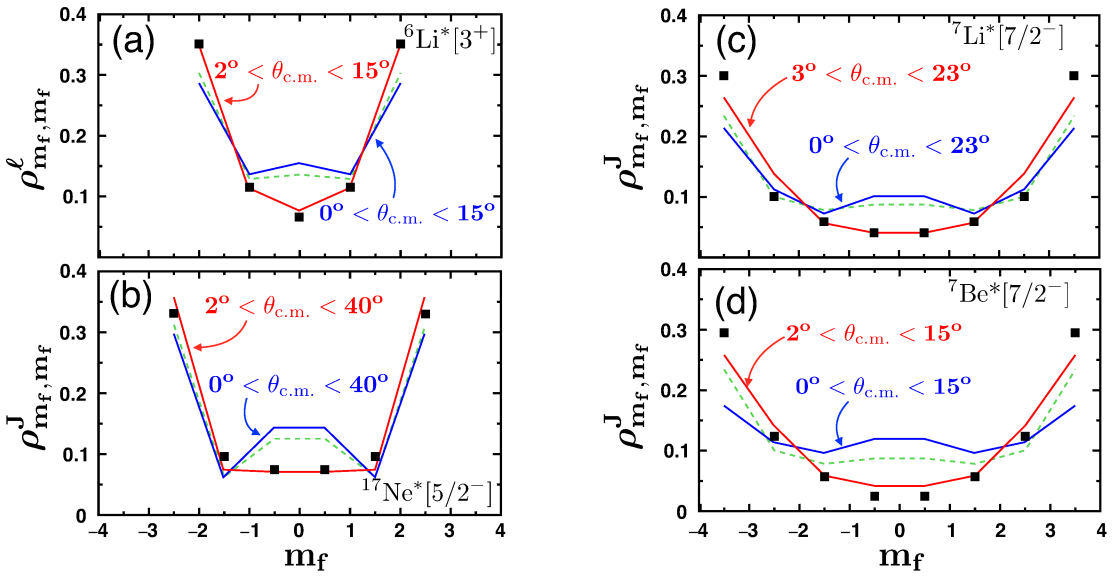

Figure 6.8: Magnetic-substate distributions extracted from the data (solid squares) and predicted by DWBA (lines) for single inelastic excitation to particle-decaying states in (a) ^{6}Li, (b) ^{17}Ne, (c) ^{7}Li, and (d) ^{7}Be. Note for (a) ^{6}Li the magnetic-substate distribution is for the decay angular momentum ($\ell_{\rm decay} = 2$). The blue and red solid lines are the DWBA predictions for angular regions including and excluding small angles, respectively. The green dashed lines are predictions from the Clebsch-Gordan coefficents in Eq. (6.15), omitting the energy and angle dependence. The black squares are data from this and other works.

spin alignment of ^{17}Ne* [51]. This observation of alignment illustrates that the alignment mechanism outlined is not a consequence of cluster structure.

Using the same breakup model and optical-model potential parameters for ^{7}Li (changing the fragment and core for each case), DWBA calculations were performed for the inelastic excitations to particle-decaying states of ^{6}Li, ^{17}Ne, and ^{7}Be at the appropriate experimental energies (E/A = 36.6, 58.5, and 65.5 MeV, respectively) and angular regions [48, 51, 119]. The experiments show, and the calculations predict, that the alignment produced is fairly constant above the grazing angle. However the calculations indicate that transverse alignments must be present at small scattering angles due to the inclusion of the spherical harmonics Y_0^L in the wavefunction. Indeed at $\theta_{\rm c.m.} = 0^o$, the only contribution to the alignment is from $M = 0$ (no tilting), and thus $m_f = m_i$ meaning no longitudinal alignment is possible. The green dashed lines in Fig. 6.8 correspond to the squared T matrix predictions from Eq. (6.15) for a single L (equal to $L_{\rm graz}$) and omitting the angle and implicit energy

dependence. These lines are in remarkable agreement with the solid blue line obtained from the T matrix integrated over the entire angular region. If small-angle scattering is removed, the T matrix calculations (solid red lines) show significant enhancement to the alignment due to the suppression of $M = 0$ transitions (non-tilting). This feature of the alignment mechanism was observed for ^{7}Be [48]. The experimental magnetic-substate distributions for ^{6}Li*[3^{+}], ^{7}Li*[7/2^{-}], ^{17}Ne*[5/2^{-}], and ^{7}Be*[7/2^{-}] are shown as black squares in Fig. 6.8. The data for ^{6}Li, ^{17}Ne, and ^{7}Be are from Refs. [48, 51]. The agreement between the data and the DWBA predictions, excluding small angles, is remarkable for several of the cases, and demonstrates the limited acceptance of the detector arrays for small angles. There is a small discrepancy in the predicted alignment for ^{7}Be. Although the optical potential parameters found for ^{7}Li + ^{12}C should be more reasonably suited for the ^{7}Be + ^{9}Be system than the other presented systems (since the projectiles are isobaric analogs), the ^{7}Be experiment was performed at a much larger beam energy ($E/A = 65.5$ MeV) and so the phenomenological optical potentials used may not be as representative of the ^{7}Be + ^{9}Be system due to the implicit energy dependence of the potentials.

It should be noted that the predictions and data for ^{6}Li* in Fig. 6.8 are for magnetic-substate populations of the decay-channel angular momentum. In principle, one can reconstruct the final angular momentum state, J_f, from the relationship $J_f = \ell_{\rm decay} + s_{\rm core} + s_{\rm frag}$, assumming there is only one decay channel angular momentum. However, only systems where $s_{\rm core} = 0$ and $s_{\rm frag} = 1/2$, or vice-versa, are completely constrained and allow for the extraction of $\rho^{J}_{m_f,m_f}$. In the ^{6}Li case, the measured magnetic-substates of the decay angular momentum indicate large longitudinal alignment, but the magnetic-substate populations of the excited projectile cannot be extracted, due to the deuteron fragment carrying spin-1 in its ground state.

Figure 6.9 shows an energy level diagram for ^{6}Li, and highlights the particular inelastic excitation of interest. For ^{6}Li, the ground and first excited state can be thought of as being the result of an α+d cluster structure, since they are near the particle decay threshold. These

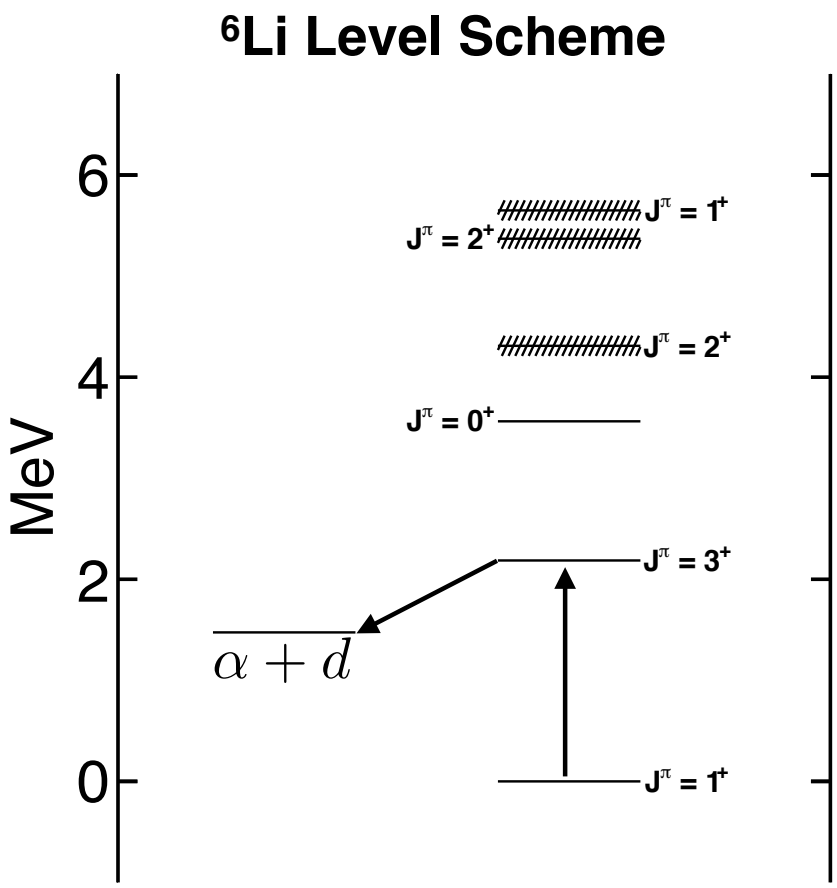

Figure 6.9: A energy level diagram for ^{6}Li. Near the particle-decay threshold to $\alpha + d$, the ground and first excited state can treated by a cluster model with internal angular momenta, $\ell = 0$ and $\ell = 2$, respectively, coupled to the spin-1 of the deuteron. The first excited state then has the deuteron spin parallel to the internal angular momentum.

states are then treated as having internal angular momenta, $\ell = 0$ and $\ell = 2$, respectively. In the case of the first excited state, the deuteron has its spin parallel to the internal angular momentum. Of the higher-lying states, only the $J^\pi = 1^+$ state is predicted by this cluster model, where the deuteron has its spin anti-parallel to the internal angular momentum. The rest of the higher-lying states require other models, but for the considerations here the cluster model is appropriate.

The fact that the final magnetic substates cannot be extracted is made clear by repeating the density matrix analysis in Ref. [48] for the ^{6}Li case ($J_f = 3, \ell_{\text{decay}} = 2, s_{\text{core}} = 0, s_{\text{frag}} = 1$)

resulting in the set of equations,

$$\rho^{\ell}_{2,2} = \rho^{J}_{3,3} + \tfrac{1}{3}\rho^{J}_{2,2} + \tfrac{1}{15}\rho^{J}_{1,1} \tag{6.16}$$

$$\rho^{\ell}_{1,1} = \tfrac{2}{3}\rho^{J}_{2,2} + \tfrac{8}{15}\rho^{J}_{1,1} + \tfrac{1}{5}\rho^{J}_{0,0} \tag{6.17}$$

$$\rho^{\ell}_{0,0} = \tfrac{4}{5}\rho^{J}_{1,1} + \tfrac{3}{5}\rho^{J}_{0,0}. \tag{6.18}$$

There is no fully-constrained solution for the final magnetic-substate populations for J given the measurement of magnetic-substate populations for ℓ_{decay}. If ^{6}Li decayed with a smaller ℓ_{decay}, then almost no alignment information would be recoverable.

6.5.5 Predictions for ^{12}C + ^{12}C

The ^{12}C + ^{12}C system is simpler than ^{7}Li + ^{12}C as there are no spin-spin or spin-orbit interactions. Extensive studies measuring the spin alignment of a single 2^{+} [4.44 MeV] inelastic excitation of ^{12}C have been performed at low energies [89, 92, 116]. These studies were focused on correlating gross structures in the alignment with intermediate structures in the excitation function of the reaction cross section. While no strong correlation was found, these studies were consistent with the reduction in magnitude of the incoming partial wave by $2\hbar$. Furthermore, these studies suggest the reaction is dominated by only one incoming partial wave due to molecular-like resonances in the experimental energy regime. Without the smoothing effect produced by a range of partial waves, a single partial wave will produce large oscillations in the alignment with angle.

To effectively measure the gross structure in alignment (because of these oscillations) the alignment measurements need to be angle-averaged and weighted by the differential cross section [92]. All of the previously mentioned studies restricted themselves to center-of-mass angles $\theta_{\text{c.m.}} > 30^{o}$, and thus a large portion of the reaction yield, and resulting alignment, was missed.

Even still, the transfer of angular momentum generated in the reaction to the intrinsic

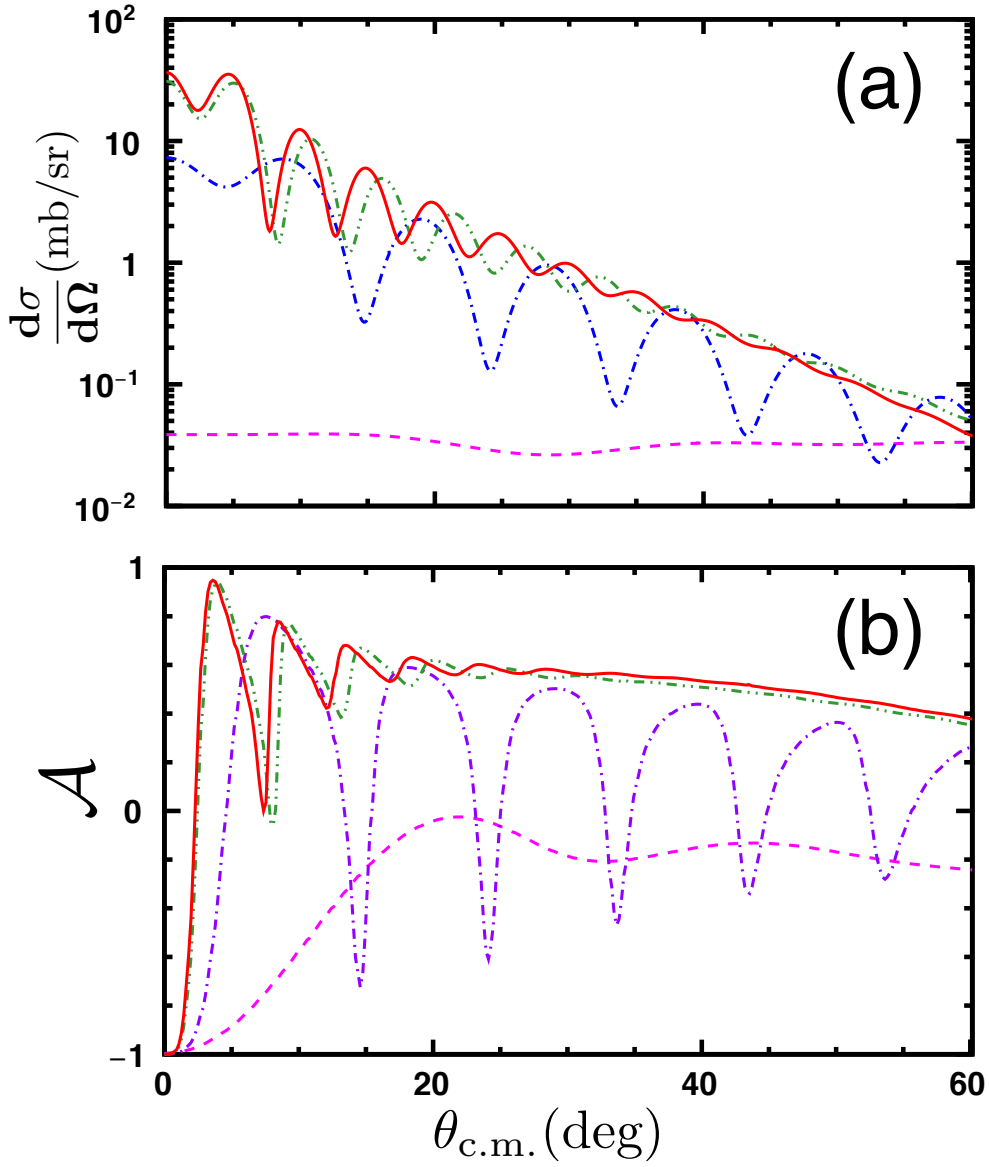

Figure 6.10: (a) Differential cross sections for the single inelastic excitation of ^{12}C* [4.44 MeV] predicted by a DWBA soft-rotator model for the beam energies E/A = 2.0, 5.8, 12.0, and 17.0 MeV (purple dashed, blue dot-dashed, green dot-dot-dashed, and red solid line, respectively). (b) A coarse excitation function of the spin alignment for ^{12}C*, as a function of scattering angle, for the same beam energies.

spin of ^{12}C* is consistent with the alignment mechanism outlined in this work, and at larger beam energies tilting of the exit-channel reaction plane should occur resulting in a longitudinal spin alignment of ^{12}C*. Predictions for the spin alignment of ^{12}C* [4.44 MeV] have been made previously using a variety of models including DWBA predictions [117], but these studies focused on the previously mentioned low-energy data sets.

The proposed alignment mechanism can be tested by measuring a coarse excitation function of the generated spin alignment as a function of scattering angle. These measurements of the coarse excitation function would allow one to probe the predicted threshold of the alignment mechanism. By measuring the spin alignment over a large portion of the reaction yield (i.e. scattering angles around the grazing angle) the gross structure of the alignment can be found and compared to theoretical predictions. Figure 6.10(a) shows the differential cross sections predicted by a DWBA soft-rotator model for the beam energies $E/A =$ 2.0, 5.8, 12.0, and 17.0 MeV (purple dashed, blue dot-dashed, orange dot-dot-dashed, and red solid line, respectively), while Fig. 6.10(b) shows the corresponding alignments. The optical-potential parameters employed came from the literature [120]. In order to do a proper phenomenological optical-model analysis, the optical potential parameters should be fit to differential elastic and inelastic cross section data at each energy because of the implicit energy dependence of phenomenological optical potentials.

Well below the angular-momentum-excitation-energy mismatch threshold, around $E/A =$ 5 MeV (deduced from semi-classical calculations), the overall alignment should be transverse to the beam axis ($\mathcal{A} < 0$). This is predicted for measurements at a beam energy of $E/A = 2.0$ MeV. Larger longitudinal alignment should be observed after passing this threshold (this is seen for the $E/A = 5.8$ MeV prediction in Fig. 6.10). Interestingly, the minima in the alignment correspond with diffraction minima in the differential scattering cross section. This a consequence of the fact that the same spherical harmonics are responsible for the diffraction minima in the differential cross section and angular distributions for the alignment. Therefore, these minima in alignment will not be observed in the angle-averaged

alignment because it is weighted by the differential cross section. Well above this threshold, the generated alignment does not vary significantly with energy (comparing $E/A = 12.0$ and 17.0 MeV) and the gross structure of alignment should be similar to the Clebsch-Gordan coefficents in Eq. (6.15). Also, the contribution of many partial waves to the cross section result in a spin alignment that is fairly constant at large scattering angles. Since the overall yield of the alignment has to be weighted by the differential cross section, the overall (i.e. gross) alignment will be largely longitudinal at intermediate energies.

Chapter 7

Conclusion

"There are two possible outcomes: if the result confirms the hypothesis, then you've made a measurement. If the result is contrary to the hypothesis, then you've made a discovery."

—Enrico Fermi

The results found for the experiment presented in this dissertation, involving inelastic scattering of ^{7}Li projectiles at intermediate energies, were entirely contrary to the proposed hypothesis of spin alignment generated from spin-flips of the target. Therefore, in-line with Fermi, a phenomenon where longitudinal spin alignment is generated in inelastic processes, that is present in many nuclear systems, was discovered. Large longiditudinal spin alignment of inelastically excited projectiles resulting from an angular-momentum-excitation-energy mismatch has now been observed in the nuclei, ^{6}Li, ^{7}Li, ^{7}Be, ^{17}Ne, and ^{13}O [48, 51, 95, 121], and this phenomenon is expected to be observed in many more systems. Even with these observations, an experiment with the express purpose of studying the angular-momentum-excitation-energy mismatch should be performed, and such an experiment will be discussed in the following section. The features of the proposed alignment mechanism suggest that the resulting spin alignment can be reliably generated and make it applicable for use in other experiments. In particular, g-factor measurements of short-lived excited nuclei require

a reliable method for generating spin polarized or aligned states. Generating such populations in the reaction used to create the state is, perhaps, the best way to perform such measurements. In fact, this phenomenon may have already been observed and used in g-factor measurements utilizing Coulomb excitation. The nature of the alignment mechanism also suggests it is a general phenomenon, and should even be observed in atomic collisions performed at intermediate energies. Such a case for atomic Coulomb excitation will be presented.

7.1 Test of Spin Alignment Mechanism

To obtain a good test of the proposed reaction mechanism an excitation function for the generated spin alignment, over many scattering angles, needs to be measured. Since the proposed mechanism should be present in any single inelastic excitation we can use a much simpler system that ^{7}Li + X. The ^{12}C+^{12}C system is one such system and has many advantages over the system studied in this dissertation. Because ^{7}Li has non-zero spin in its ground state, there is a coupling between its spin and the orbit of the collision, and this has effects on ther resulting decay correlations. In the case of ^{12}C + ^{12}C, both the projectile and target have spin-zero in their ground state, and thus the effect of spin-orbit coupling on the resulting alignment is removed. Furthermore, ^{7}Li*[4.6 MeV] decays by particle emission, and thus the resulting alignment has to be extracted via particle-particle correlations, which have their own host of problems. One being that it is difficult to measure all 4π of the reaction, and the spectra have to be efficiency corrected by a rather complicated scheme. The ^{12}C*[4.4 MeV] state is bound with respect to particle emission but decays via γ-ray emission. Sophisticated 4π detectors for measuring γ-ray angular correlations exist, such as the GAMMASPHERE array, where the photopeak efficiency is very well known. The 4.4 MeV state is the first excited state in ^{12}C, and with such a large energy separation between the ground state and other excited states it is relatively easy to distinguish the 4.4 MeV γ-ray emitted by ^{12}C* from other products generated in ^{12}C + ^{12}C collisions, allowing for concrete

determination of the populated excited state. Furthermore, because the constituents of the reaction are identical, they have the same center-of-mass scattering angle. This makes the data analysis much simpler, as it is not required to differentiate between which ^{12}C was excited, and both should exhibit large longitudinal spin alignment.

An experiment using the ^{12}C + ^{12}C system for such a test of the proposed reaction mechanism has already been approved (and given the highest priority) at the ATLAS facility at Argonne National Laboratory and will likely be performed in early 2019. The accepted proposal is presented in Appendix B.

7.2 Applications of Spin Alignment Mechanism

7.2.1 Coulomb Excitation at Intermediate Energies

As it was shown in the previous chapter, the generated alignment from an angular-momentum-excitation-energy mismatch is largely independent of the scattering potential. Thus, this mechanism should be present for scattering experiments only utilizing the Coulomb potential for excitations. Coulomb excitations occur in very peripheral collisions, and so a similar argument for angular-momentum-excitation-energy matching can be made for such reactions. In fact, studies of inelastic scattering through Coulomb excitation are consistent with the alignment mechanism arising from an angular-momentum-excitation-energy mismatch, which should occur provided $E^* \ll E_{\text{c.m.}}$. Figure 7.1 shows the prediction [114] for the γ-ray angular distributions, in the laboratory frame, for electric quadrupole excitation of ^{56}Ni ($J_i = 0 \rightarrow J_f = 2$) bombarding ^{209}Bi at $E/A = 85$ MeV for several different excitation energies. As the excitation energy is reduced, the alignment increases. This is consistent with an angular-momentum-excitation-energy mismatch. The proposed mechanism of spin alignment generation provides a qualitative description for all of the features of alignment predicted in this theoretical study. However, if one were to compare the predictions in Ref. [114] with the Clebsch-Gordon coefficient predictions from Eq. (6.15), the aforementioned

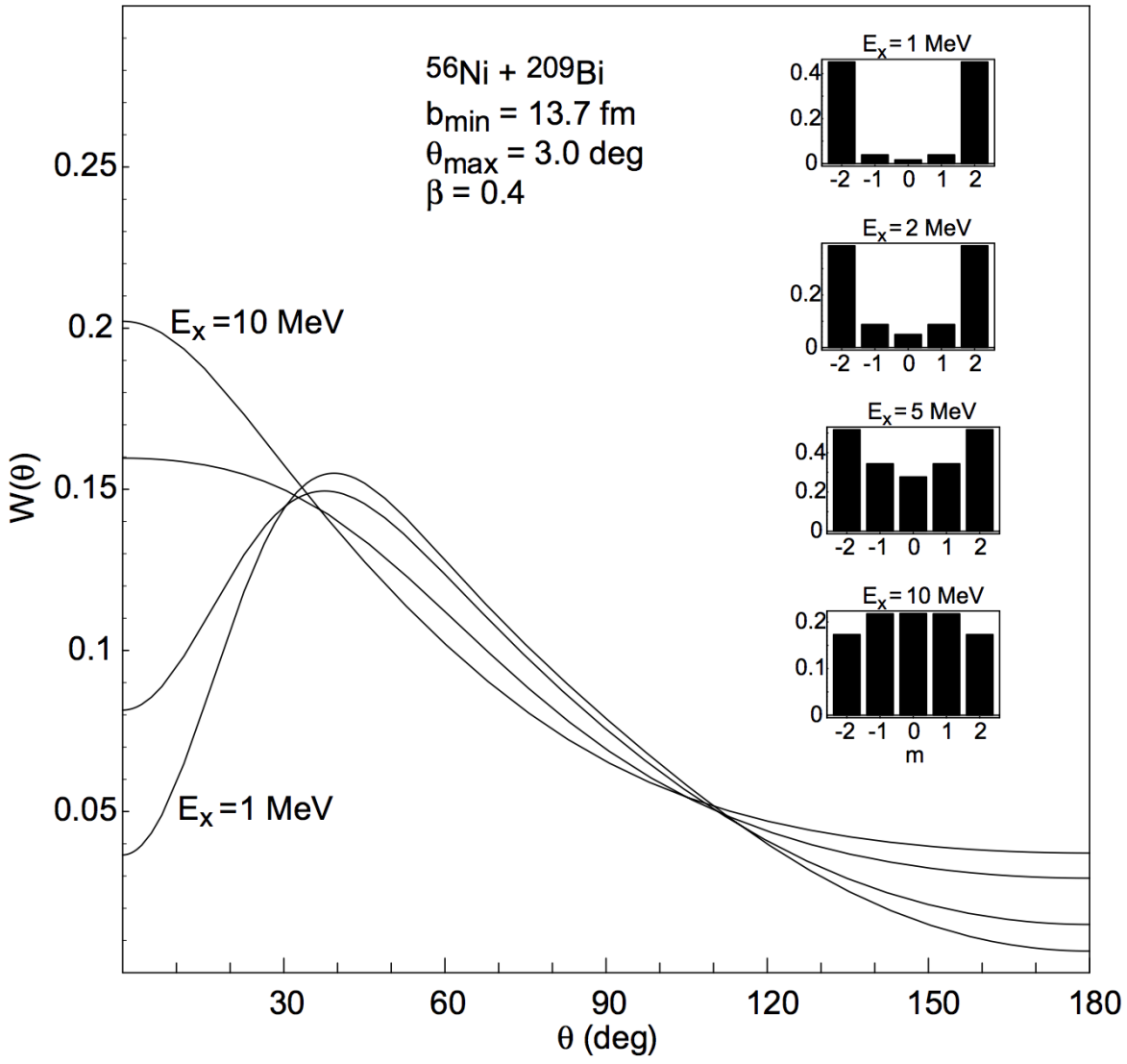

Figure 7.1: Figure 13 from Ref. [114]. Decay angular distribution of γ-rays in the laboratory frame for quadrupole coulomb excitation ($J_i \rightarrow J_f = 2$) to different excitation energies of ^{56}Ni, for ^{56}Ni scattering off ^{209}Bi at $E/A = 85$ MeV.

studies should be extended over a range of scattering angles.

Transient-Field Method

The decay correlations of ^{38}S$^{*}(J^{\pi} = 2^{+})$ and ^{40}S$^{*}(J^{\pi} = 2^{+})$ Coulomb excited at bombarding energies of $E/A = 40$ MeV were consistent with large longitudinal spin alignment [1]†. This longitudinal spin alignment resulting from Coulomb excitation at intermediate energies was used to determine g-factors of excited states of nuclei through the transient-field method. While the observation of large longitudinal alignment generated from inelastic nuclear transitions suggests that these types of experiments don't have to restrict themselves to Coulomb excitation, there is a caveat. The magnitude of generated alignment is largely independent of potential, however, there are still ambiguities in the the final magnetic-substate populations because of the angle-averaging that is weighted by the differential cross section. Thus it is necessary to have the differential cross section measured, or be in a regime well above the grazing angle where the alignment produced is rather independent of angle. Calculations of Coulomb excitation do not have ambiguities, as the potentials are already well defined. However, Coulomb excitation experiments must restrict themselves to small angle scattering to only consider impact parameters $b > b_{\text{graz}}$. At small scattering angles the resulting alignment quickly switches from $\mathcal{A} < 0$ to $\mathcal{A} > 0$, and thus the scattering angle must be measured precisely to constrain the generated alignment. If one were to use a nuclear excitation, the error on the scattering angle is not as much of an issue, so long as the experiment is performed well above the grazing angle or the alignment is measured over a sufficient angular range that the generated alignment follows the Clebsch-Gordan coefficents in Eq. (6.15). In summary, although the contrainsts on what reaction is necessary for generating alignment to perform g-factor measurements through the transient-field method is relaxed, it appears that safe Coulomb excitation may still be the preferred method for precision measurements, as these transitions can be calculated exactly.

†Although the magnetic-substate populations weren't explicitly given in this work, they can be inferred from the published data of the decay correlations.

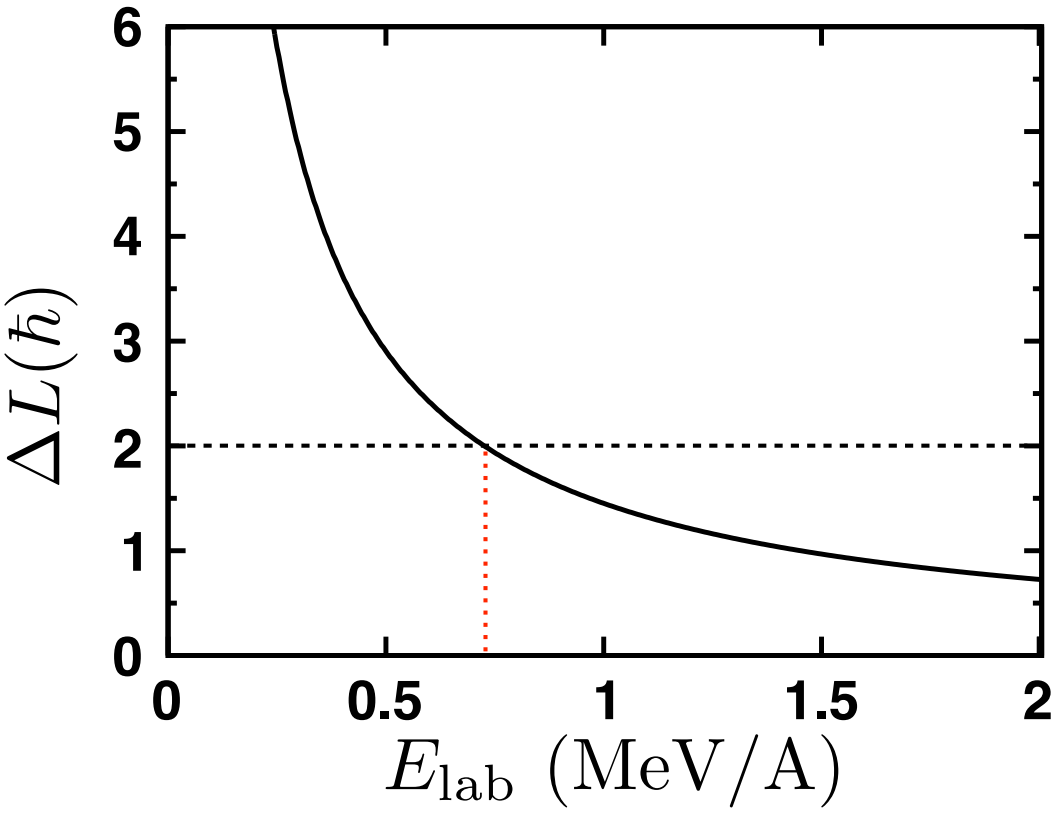

Figure 7.2: Equation (6.1) is plotted for $E^* = 0.05$ eV and $R = 18$ Å for H_2 projectiles impinging on a N_2 target. At bombarding energies $> E/A = 0.7$ MeV the resulting $J = 2$ state should begin to be aligned with the beam axis.

Although, there may be instances where inelastic scattering through nuclear excitation may be preferable for g-factor measurements. If the charge of the system of interest is rather small, then the cross section for nuclear scattering may be much larger than for Coulomb excitation, making the experiment possible. Such would be the case for low-mass neutron-rich isotopes, which are of considerable interest for nuclear astrophysics. The structure of such nuclei influence the r-process and thus the nucleosynthesis of heavier elements.

7.2.2 Atomic Collisions

This spin alignment mechanism arising from an angular-momentum-excitation-energy mismatch should also appear in atomic collisions. As an example, one can apply Eq. (6.1) to the case of H_2 inelastically scattering off N_2. The first $J = 2$ rotational state of H_2 is at $\sim$

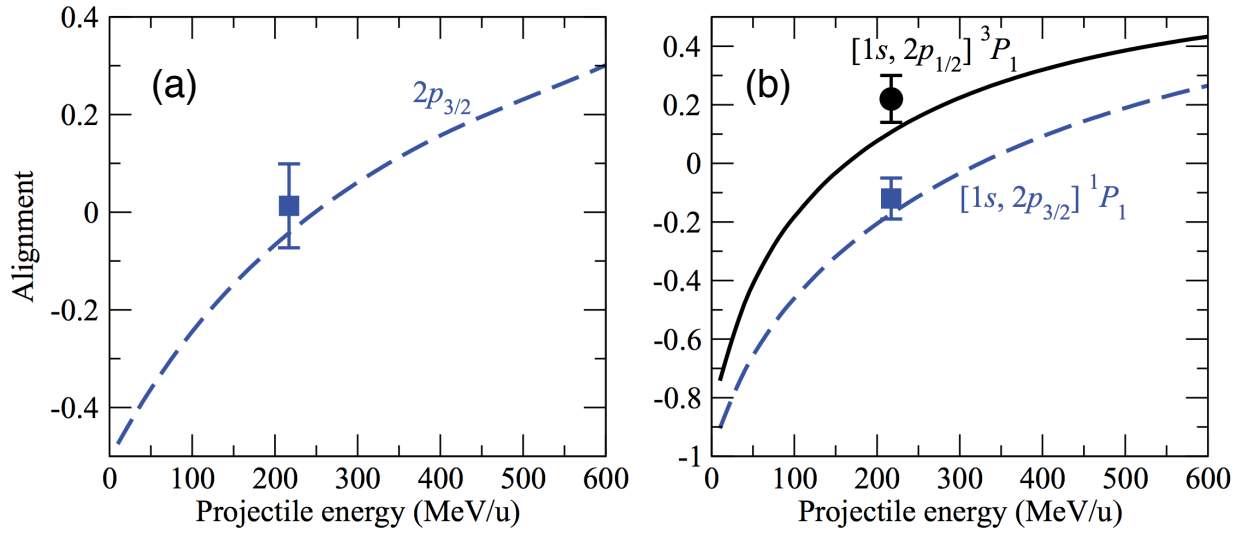

Figure 7.3: Figure 4 from Ref. [33]. The predicted alignments are shown as the lines, while the points show measurements, for hydrogen-like (a) and helium-like (b) uranium ions.

50 meV, and assuming a grazing collision with radius of interaction $R = r_{H_2} + r_{N_2} = 2.5 + 15.5$ Å, we obtain the curve presented in Fig. 7.2. Above a bombarding energy of $E/A = 0.7$ MeV (indicated by the red dotted line in Fig. 7.2), $\Delta L = 2\hbar$ transfers are no longer allowed and the resulting state in H_2 should begin to be aligned with the beam axis. Atomic or molecular scattering experiments are not typically performed at such large bombarding energies, although there are a handful of facilities around the world that can and do perform such experiments.

For example, such longitudinal alignment phenomena have been predicted and observed for hydrogren-like and helium-like uranium ions at intermediate energies [122, 33]. Figure 7.3(a) shows the predicted and measured alignment of hydrogren-like uranium ions, while Fig. 7.3(b) shows the same quantities for helium-like uranium ions from Ref. [33]. These experiments were performed at the experimental storage ring at GSI, a facility in Germany. The predicted features of the excitation functions of alignment are similar to those predicted by DWBA calculations of nuclear scattering, where the alignment takes negative values at small bombarding energies and starts to plateau above a certain energy (i.e. the phenomenon

has a threshold). Furthermore, if the excitation energy of the state is lowered then it should be more aligned at a particular bombarding energy. This feature can be seen by comparing the curves and measurements for the states $^3P_1$ and $^1P_1$, which have excitation energies of 180 and 190 keV, respectively. In these cases, the smaller excitation energy has a larger mismatch and so alignment begins at a smaller bombarding energy. Thus the lower energy state will be more aligned than the higher energy state at a given bombarding energy. Furthermore, the magnitude of alignment is largely independent of the target. In fact, Surzhykov et al. claim that, "[...] the alignment parameters [...] do not depend on the charge of the target nucleus" [122]. These combined features of the alignment phenomenon are suggestive of an angular-momentum-excitation-energy mismatch.

With this observation of large longitudinal spin alignment generated in inelastic atomic collisions, it appears that the proposed mechanism for generating spin alignment has applications even beyond that of nuclear science.

Bibliography

[1] A. D. Davies, A. E. Stuchbery, P. F. Mantica, P. M. Davidson, A. N. Wilson, A. Becerril, B. A. Brown, C. M. Campbell, J. M. Cook, D. C. Dinca, A. Gade, S. N. Liddick, T. J. Mertzimekis, W. F. Mueller, J. R. Terry, B. E. Tomlin, K. Yoneda, and H. Zwahlen. Probing shell structure and shape changes in neutron-rich sulfur isotopes through transient-field g-factor measurements on fast radioactive beams of ^{38}S and ^{40}S. *Phys. Rev. Lett.*, 96:112503, Mar 2006.

[2] B.P. Abbott et al. Multi-messenger observations of a binary neutron star merger. *The Astrophysical Journal Letters*, 848(2):L12, 2017.

[3] V.M. Strutinsky. Shell effects in nuclear masses and deformation energies. *Nuclear Physics A*, 95(2):420 – 442, 1967.

[4] Walther Gerlach and Otto Stern. Das magnetische moment des silberatoms. *Zeitschrift für Physik*, 9(1):353–355, Dec 1922.

[5] George E Uhlenbeck and Samuel Goudsmit. Spinning electrons and the structure of spectra. *Nature*, 117(2938):264, 1926.

[6] I Estermann and O Stern. Über die magnetische ablenkung von isotopen wasserstoffmolekülen und das magnetische moment des „deutons “. *Zeitschrift für Physik*, 86(1-2):132–134, 1933.

[7] R. Frisch and O. Stern. Über die magnetische ablenkung von wasserstoffmolekülen und das magnetische moment des protons. *Zeitschrift für Physik*, 85(1):4–16, Jan 1933.

[8] F. R. S. J. Chadwick. The existence of a neutron. *Proceedings of the Royal Society of London A: Mathematical, Physical and Engineering Sciences*, 136(830):692–708, 1932.

[9] Luis W. Alvarez and F. Bloch. A quantitative determination of the neutron moment in absolute nuclear magnetons. *Phys. Rev.*, 57:111–122, Jan 1940.

[10] E. D. Bloom, D. H. Coward, H. DeStaebler, J. Drees, G. Miller, L. W. Mo, R. E. Taylor, M. Breidenbach, J. I. Friedman, G. C. Hartmann, and H. W. Kendall. High-energy inelastic $e - p$ scattering at 6° and 10°. *Phys. Rev. Lett.*, 23:930–934, Oct 1969.

[11] M. Breidenbach, J. I. Friedman, H. W. Kendall, E. D. Bloom, D. H. Coward, H. DeStaebler, J. Drees, L. W. Mo, and R. E. Taylor. Observed behavior of highly inelastic electron-proton scattering. *Phys. Rev. Lett.*, 23:935–939, Oct 1969.

[12] Constantia Alexandrou, Martha Constantinou, Giannis Koutsou, Konstantin Ottnad, and Marcus Petschlies. Position space method for the nucleon magnetic moment in lattice QCD. *Phys. Rev. D*, 94:074508, Oct 2016.

[13] Assumpta Parreño, Martin J. Savage, Brian C. Tiburzi, Jonas Wilhelm, Emmanuel Chang, William Detmold, and Kostas Orginos. Octet baryon magnetic moments from lattice QCD: Approaching experiment from a three-flavor symmetric point. *Phys. Rev. D*, 95:114513, Jun 2017.

[14] Eugene P Wigner and Eugene Feenberg. Symmetry properties of nuclear levels. *Reports on Progress in Physics*, 8(1):274, 1941.

[15] R. G. Sachs. On the magnetic moment of the deuteron. *Phys. Rev.*, 72:91–98, Jul 1947.

[16] P. L. Chung, B. D. Keister, and F. Coester. Relativistic calculation of the deuteron quadrupole and magnetic moments. *Phys. Rev. C*, 39:1544–1549, Apr 1989.

[17] Toshitaka Kajino, Takehiro Matsuse, and Akito Arima. Electromagnetic properties of ^{7}Li and ^{7}Be in a cluster model. *Nuclear Physics A*, 413(2):323 – 352, 1984.

[18] S. Pastore, Steven C. Pieper, R. Schiavilla, and R. B. Wiringa. Quantum monte carlo calculations of electromagnetic moments and transitions in $a \leq 9$ nuclei with meson-exchange currents derived from chiral effective field theory. *Phys. Rev. C*, 87:035503, Mar 2013.

[19] Steven C. Pieper, , and R. B. Wiringa. Quantum monte carlo calculations of light nuclei. *Annual Review of Nuclear and Particle Science*, 51(1):53–90, 2001.

[20] W. Gruebler, W. Haeberli, and P. Schwandt. Production of a beam of polarized negative hydrogen ions. *Phys. Rev. Lett.*, 12:595–597, May 1964.

[21] W. Haeberli, W. Gruebler, P. Extermann, and P. Schwandt. Acceleration of polarized protons and deuterons in a tandem accelerator. *Phys. Rev. Lett.*, 15:267–268, Aug 1965.

[22] I.C. Girit. The unisor nuclear orientation facility. *Nuclear Instruments and Methods in Physics Research Section B: Beam Interactions with Materials and Atoms*, 40-41:423 – 428, 1989.

[23] B. E. Zimmerman, W. B. Walters, P. F. Mantica, H. K. Carter, M. G. Booth, J. Rikovska, and N. J. Stone. Determination of the magnetic dipole moment of ^{114}Sb via on-line nuclear orientation. *Hyperfine Interactions*, 75(1):117–124, Nov 1992.

[24] K. Sekiguchi, H. Sakai, H. Witała, W. Glöckle, J. Golak, M. Hatano, H. Kamada, H. Kato, Y. Maeda, J. Nishikawa, A. Nogga, T. Ohnishi, H. Okamura, N. Sakamoto, S. Sakoda, Y. Satou, K. Suda, A. Tamii, T. Uesaka, T. Wakasa, and K. Yako. Complete set of precise deuteron analyzing powers at intermediate energies: Comparison with modern nuclear force predictions. *Phys. Rev. C*, 65:034003, Feb 2002.

[25] U. Köpf, H. J. Besch, E. W. Otten, and Ch. von Platen. Optical pumping of short lived β-radioactive isotopes and the magnetic moment of ^{37}K. *Zeitschrift für Physik A Hadrons and nuclei*, 226(4):297–327, Aug 1969.

[26] W. Geithner, S. Kappertz, M. Keim, P. Lievens, R. Neugart, L. Vermeeren, S. Wilbert, V. N. Fedoseyev, U. Köster, V. I. Mishin, V. Sebastian, and ISOLDE Collaboration. Measurement of the magnetic moment of the one-neutron halo nucleus ^{11}Be. *Phys. Rev. Lett.*, 83:3792–3795, Nov 1999.

[27] C.D.P. Levy, A. Hatakeyama, Y. Hirayama, R.F. Kiefl, R. Baartman, J.A. Behr, H. Izumi, D. Melconian, G.D. Morris, R. Nussbaumer, M. Olivo, M. Pearson, R. Poutissou, and G.W. Wight. Polarized radioactive beam at isac. *Nuclear Instruments and Methods in Physics Research Section B: Beam Interactions with Materials and Atoms*, 204:689 – 693, 2003. 14th International Conference on Electromagnetic Isotope Separators and Techniques Related to their Applications.

[28] M. Huhta, P. F. Mantica, D. W. Anthony, B. A. Brown, B. S. Davids, R. W. Ibbotson, D. J. Morrissey, C. F. Powell, and M. Steiner. Anomalous p-shell isoscalar magnetic moments: Remeasurement of ^{9}C and the influence of isospin nonconservation. *Phys. Rev. C*, 57:R2790–R2793, Jun 1998.

[29] K Matsuta, M Fukuda, M Tanigaki, T Minamisono, Y Nojiri, M Mihara, T Onishi, T Yamaguchi, A Harada, M Sasaki, et al. Magnetic moment of proton drip-line nucleus ^{9}C. *Nuclear Physics A*, 588(1):c153–c156, 1995.

[30] K. Varga, Y. Suzuki, and I. Tanihata. Microscopic four-cluster description of the mirror nuclei ^{9}Li and ^{9}C. *Phys. Rev. C*, 52:3013–3025, Dec 1995.

[31] J. Wilczyński. Nuclear molecules and nuclear friction. *Physics Letters B*, 47(6):484 – 486, 1973.

[32] W Trautmann, J De Boer, W Dünnweber, G Graw, R Kopp, C Lauterbach, H Puchta, and U Lynen. Evidence for negative deflection angles in ^{40}Ar+ Ag deep-inelastic reactions from γ-ray circular polarization measurements. *Physical Review Letters*, 39(17):1062, 1977.

[33] A. Gumberidze, S. Fritzsche, S. Hagmann, C. Kozhuharov, X. Ma, M. Steck, A. Surzhykov, A. Warczak, and Th. Stöhlker. Magnetic-sublevel population and alignment for the excitation of h- and he-like uranium in relativistic collisions. *Phys. Rev. A*, 84:042710, Oct 2011.

[34] Z. Majka, D. G. Sarantites, L. G. Sobotka, K. Honkanen, E. L. Dines, L. A. Adler, Li Ze, M. L. Halbert, J. R. Beene, D. C. Hensley, R. P. Schmitt, and G. Nebbia. Nuclear shapes from $\alpha + \gamma$-ray angular correlations. *Phys. Rev. Lett.*, 58:322–325, Jan 1987.

[35] A. H. Wuosmaa, R. W. Zurmühle, P. H. Kutt, S. F. Pate, S. Saini, M. L. Halbert, and D. C. Hensley. Single and correlated spin alignments for resonances in ^{24}Mg + ^{24}Mg inelastic scattering. *Phys. Rev. Lett.*, 58:1312–1315, Mar 1987.

[36] F. A. Dilmanian, D. G. Sarantites, M. Jääskeläinen, H. Puchta, R. Woodward, J. R. Beene, D. C. Hensley, M. L. Halbert, R. Novotny, L. Adler, R. K. Choudhury, M. N. Namboodiri, R. P. Schmitt, and J. B. Natowitz. α-particle angular distributions with respect to spin direction. *Phys. Rev. Lett.*, 49:1909–1912, Dec 1982.

[37] N. G. Nicolis, D. G. Sarantites, L. A. Adler, F. A. Dilmanian, K. Honkanen, Z. Majka, L. G. Sobotka, Z. Li, T. M. Semkow, J. R. Beene, M. L. Halbert, D. C. Hensley, J. B. Natowitz, R. P. Schmitt, D. Fabris, G. Nebbia, and G. Mouchaty. Deformation effects in the compound nucleus decay using the spin-alignment method. *Phys. Rev. C*, 41:2118–2133, May 1990.

[38] R.J. Puigh, P. Dyer, R. Vandenbosch, T.D. Thomas, L. Nunnelley, and M.S. Zisman. Magnitude and alignment of transferred angular momentum in both quasi and deeply inelastic scattering. *Physics Letters B*, 86(1):24 – 28, 1979.

[39] Dieter Fick. Polarization in heavy ion reactions. *Annual Review of Nuclear and Particle Science*, 31(1):53–74, 1981.

[40] G. J. Wozniak, R. J. McDonald, A. J. Pacheco, C. C. Hsu, D. J. Morrissey, L. G. Sobotka, L. G. Moretto, S. Shih, C. Schück, R. M. Diamond, H. Kluge, and F. S. Stephens. Rise and fall of the spin alignment in deep-inelastic reactions. *Phys. Rev. Lett.*, 45:1081–1084, Sep 1980.

[41] L. G. Sobotka, C. C. Hsu, G. J. Wozniak, D. J. Morrissey, and L. G. Moretto. Angular momentum transfer and partition in the deep-inelastic reaction 664 MeV ^{84}Kr + $^{\text{nat}}$Ag. *Nuclear Physics A*, 371(3):510 – 532, 1981.

[42] D. J. Morrissey, G. J. Wozniak, L. G. Sobotka, R. J. McDonald, A. J. Pacheco, and L. G. Moretto. Sequential fission angular distributions from mass-asymmetric heavy-ion reactions. *Nuclear Physics A*, 442(3):578 – 604, 1985.

[43] P. Dyer, R.J. Puigh, R. Vandenbosch, T.D. Thomas, M.S. Zisman, and L. Nunnelley. Q- and z-dependence of angular momentum transfer in deeply inelastic collisions of ^{86}Kr with ^{209}Bi. *Nuclear Physics A*, 322(1):205 – 236, 1979.

[44] D.J. Morrissey, G.J. Wozniak, L.G. Sobotka, A.J. Pacheco, R.J. McDonald, C.C. Hsu, and L.G. Moretto. Intrinsic fragment spins generated in the reactions of ^{20}Ne with ^{197}Au and ^{238}U at 12.6 MeV/nucleon. *Nuclear Physics A*, 389(1):120 – 140, 1982.

[45] Y. Ichikawa, H. Ueno, Y. Ishii, T. Furukawa, A. Yoshimi, D. Kameda, H. Watanabe, N. Aoi, K. Asahi, D. L. Balabanski, R. Chevrier, J.-M. Daugas, N. Fukuda, G. Georgiev, H. Hayashi, H. Iijima, N. Inabe, T. Inoue, M. Ishihara, T. Kubo, T. Nanao, T. Ohnishi, K. Suzuki, M. Tsuchiya, H. Takeda, and M. M. Rajabali. Production of spin-controlled rare isotope beams. *Nat. Phys.*, 8:918–922, 2012.

[46] M. Kmiecik, A. Maj, J. Gerl, G. Neyens, L. Atanasova, D.L. Balabanski, F. Becker, P. Bednarczyk, G. Benzoni, N. Blasi, A. Bracco, S. Brambilla, L. Caceres, F. Camera, M. Ciemała, F.C.L. Crespi, S.K. Chamoli, S. Chmel, J.M. Daugas, P. Detistov, P. Doornenbal, G. Georgiev, K. Gladnishki, M. Górska, H. Grawe, J. Grębosz, M. Hass, R. Hoischen, G. Ilie, M. Ionescu-Bujor, J. Jolie, I. Kojuharov, A. Krasznahorkay, R. Kulessa, M. Lach, S. Lakshmi, S. Leoni, G. Lo Bianco, R. Lozeva, K.H. Maier, S. Mallion, K. Mazurek, W. Męczński, B. Million, D. Montanari, S. Myalski, C. Petrache, M. Pfützner, S. Pietri, Zs. Podolyák, W. Prokopowicz, D. Rudolph, N. Saito, T.R. Saito, A. Saltarelli, G.S. Simpson, J. Styczeń, N. Vermeulen, E. Werner-Malento, O. Wieland, H.J. Wollersheim, and Zięblíński. Spin-alignment and g-factor measurement of the $I^{\pi} = 12^{+}$ isomer in ^{192}Pb produced in the relativistic-energy fragmentation of a ^{238}U beam. *Eur. Phys. J. A*, 45(2):153–158, 2010.

[47] W.-D. Schmidt-Ott, K. Asahi, Y. Fujita, H. Geissel, K.-D. Gross, T. Hild, H. Irnich, M. Ishihara, K. Krumbholz, V. Kunze, A. Magel, F. Meissner, K. Muto, H. Okuno, M. Pfützner, C. Scheidenberger, K. Suzuki, M. Weber, and C. Wennemann. Spin alignment of ^{43}Sc produced in the fragmentation of 500 MeV/u ^{46}Ti. *Z. Phys. A*, 350:215–219, 1994.

[48] R. J. Charity, J. M. Elson, J. Manfredi, R. Shane, L. G. Sobotka, Z. Chajecki, D. Coupland, H. Iwasaki, M. Kilburn, Jenny Lee, W. G. Lynch, A. Sanetullaev, M. B. Tsang, J. Winkelbauer, M. Youngs, S. T. Marley, D. V. Shetty, and A. H. Wuosmaa. Spin alignment of excited projectiles due to target spin-flip interactions. *Phys. Rev. C*, 91:024610, Feb 2015.

[49] J. Ritman, F.-D. Berg, W. Kühn, V. Metag, R. Novotny, M. Notheisen, P. Paul, M. Pfeiffer, O. Schwalb, H. Löhner, L. Venema, A. Gobbi, N. Herrmann, K. D. Hildenbrand, J. Mösner, R. S. Simon, K. Teh, J. P. Wessels, and T. Wienold. First observation of the coulomb-excited double giant dipole resonance in ^{208}Pb via double-γ decay. *Phys. Rev. Lett.*, 70:533–536, Feb 1993.

[50] Carlos A. Bertulani and Gerhard Baur. Electromagnetic processes in relativistic heavy ion collisions. *Physics Reports*, 163(5):299 – 408, 1988.

[51] R. J. Charity, K. W. Brown, J. Okołowicz, M. Płoszajczak, J. M. Elson, W. Reviol, L. G. Sobotka, W. W. Buhro, Z. Chajecki, W. G. Lynch, J. Manfredi, R. Shane, R. H. Showalter, M. B. Tsang, D. Weisshaar, J. R. Winkelbauer, S. Bedoor, and A. H. Wuosmaa. Spin alignment following inelastic scattering of ^{17}Ne, lifetime of ^{16}F, and its constraint on the continuum coupling strength. *Phys. Rev. C*, 97:054318, May 2018.

[52] D. E. M. Hoff, G. Potel, K. W. Brown, R. J. Charity, C. D. Pruitt, L. G. Sobotka, T. B. Webb, B. Roeder, and A. Saastamoinen. Large longitudinal spin alignment generated in inelastic nuclear reactions. *Phys. Rev. C*, 97:054605, May 2018.

[53] B. M. Axilrod and E. Teller. Interaction of the van der waals type between three atoms. *The Journal of Chemical Physics*, 11(6):299–300, 1943.

[54] John David Jackson. *Classical electrodynamics*. Wiley, 1999.

[55] Kazuhiko Andō and Hiroharu Bandō. Single-particle spin-orbit splittings in nuclei. *Progress of Theoretical Physics*, 66(1):227–250, 1981.

[56] Steven C. Pieper and V. R. Pandharipande. Origins of spin-orbit splitting in ^{15}N. *Phys. Rev. Lett.*, 70:2541–2544, Apr 1993.

[57] K. Bennaceur, F. Nowacki, J. Okołowicz, and M. Płoszajczak. Study of the ^{7}Be$(p,\gamma)^{8}$B and ^{7}Li$(n,\gamma)^{8}$Li capture reactions using the shell model embedded in the continuum. *Nuclear Physics A*, 651(3):289 – 319, 1999.

[58] J. Rotureau, J. Okołowicz, and M. Płoszajczak. Theory of the two-proton radioactivity in the continuum shell model. *Nuclear Physics A*, 767:13 – 57, 2006.

[59] J. Okołowicz, M. Płoszajczak, and I. Rotter. Dynamics of quantum systems embedded in a continuum. *Physics Reports*, 374(4):271 – 383, 2003.

[60] Josef Paldus. Correlation problems in atomic and molecular systems. v. spin-adapted coupled cluster many-electron theory. *The Journal of Chemical Physics*, 67(1):303–318, 1977.

[61] Yingbin Ge, Mark S. Gordon, and Piotr Piecuch. Breaking bonds with the left eigenstate completely renormalized coupled-cluster method. *The Journal of Chemical Physics*, 127(17):174106, 2007.

[62] Ryan M. Olson, Sergey Varganov, Mark S. Gordon, Horia Metiu, Steeve Chretien, Piotr Piecuch, Karol Kowalski, Stanislaw A. Kucharski, and Monika Musial. Where does the planar-to-nonplanar turnover occur in small gold clusters? *Journal of the American Chemical Society*, 127(3):1049–1052, 2005. PMID: 15656643.

[63] D.J. Thouless. Stability conditions and nuclear rotations in the hartree-fock theory. *Nuclear Physics*, 21:225 – 232, 1960.

[64] J. Rotureau, P. Danielewicz, G. Hagen, F. M. Nunes, and T. Papenbrock. Optical potential from first principles. *Phys. Rev. C*, 95:024315, Feb 2017.

[65] J. Emiliano Deustua, Jun Shen, and Piotr Piecuch. Converging high-level coupled-cluster energetics by monte carlo sampling and moment expansions. *Phys. Rev. Lett.*, 119:223003, Nov 2017.

[66] Sven Gösta Nilsson. Binding states of individual nucleons in strongly deformed nuclei. *Dan. Mat. Fys. Medd.*, 29(CERN-55-30):1–69, 1955.

[67] M. Ionescu-Bujor, A. Iordachescu, D. L. Balabanski, S. Chmel, G. Neyens, G. Baldsiefen, D. Bazzacco, F. Brandolini, D. Bucurescu, M. Danchev, M. De Poli, G. Georgiev, A. Görgen, H. Haas, H. Hübel, G. Ilie, N. Marginean, R. Menegazzo, P. Pavan, G. Rainovski, R. V. Ribas, C. Rossi Alvarez, C. A. Ur, K. Vyvey, and S. Frauendorf. Quadrupole moments and g factors for high-spin neutron isomers in ^{193}Pb. *Phys. Rev. C*, 70:034305, Sep 2004.

[68] K. Vyvey, G. D. Dracoulis, A. N. Wilson, P. M. Davidson, A. E. Stuchbery, G. J. Lane, A. P. Byrne, and T. Kibédi. g factors of the 9^- and 11^- isomers in ^{194}Pb and ^{196}Pb: Configuration mixing and deformation. *Phys. Rev. C*, 69:064318, Jun 2004.

[69] C. Teich, A. Jungclaus, V. Fischer, D. Kast, K. P. Lieb, C. Lingk, C. Ender, T. Härtlein, F. Köck, D. Schwalm, J. Billowes, J. Eberth, and H. G. Thomas. Measurement of g factors in ^{84,86}Zr and ^{87}Nb by the recoil distance transient field γ-γ coincidence technique. *Phys. Rev. C*, 59:1943–1955, Apr 1999.

[70] R. B. Wiringa, Steven C. Pieper, J. Carlson, and V. R. Pandharipande. Quantum monte carlo calculations of A = 8 nuclei. *Phys. Rev. C*, 62:014001, Jun 2000.

[71] G.P. Mueller and J.W. Clark. Ground state properties of alpha matter. *Nuclear Physics A*, 155(2):561 – 581, 1970.

[72] R. W. Finlay, W. P. Abfalterer, G. Fink, E. Montei, T. Adami, P. W. Lisowski, G. L. Morgan, and R. C. Haight. Neutron total cross sections at intermediate energies. *Phys. Rev. C*, 47:237–247, Jan 1993.

[73] W. P. Abfalterer, F. B. Bateman, F. S. Dietrich, R. W. Finlay, R. C. Haight, and G. L. Morgan. Measurement of neutron total cross sections up to 560 MeV. *Phys. Rev. C*, 63:044608, Mar 2001.

[74] R. Shane, R.J. Charity, J.M. Elson, L.G. Sobotka, M. Devlin, N. Fotiades, and J.M. O'Donnell. Total neutron cross-sections for rare isotopes using a digital-signal-processing technique: Case study ^{48}Ca. *Nuclear Instruments and Methods in Physics Research Section A: Accelerators, Spectrometers, Detectors and Associated Equipment*, 614(3):468 – 474, 2010.

[75] W. Nörenberg and H. Weidenmüller. *Introduction to the Theory of Heavy-Ion Collisions*. Springer, New York, 1976.

[76] Ian J. Thompson. Coupled reaction channels calculations in nuclear physics. *Computer Physics Reports*, 7(4):167 – 212, 1988.

[77] G. R. Satchler. *Direct Nuclear Reactions*. Oxford University Press, Oxford, 1983.

[78] N. Austern. *Direct nuclear reaction theories*. Interscience monographs and texts in physics and astronomy. Wiley-Interscience, 1970.

[79] Roger G Newton. Optical theorem and beyond. *American Journal of Physics*, 44(7):639–642, 1976.

[80] J. M. Mueller, R. J. Charity, R. Shane, L. G. Sobotka, S. J. Waldecker, W. H. Dickhoff, A. S. Crowell, J. H. Esterline, B. Fallin, C. R. Howell, C. Westerfeldt, M. Youngs, B. J. Crowe, and R. S. Pedroni. Asymmetry dependence of nucleon correlations in spherical nuclei extracted from a dispersive-optical-model analysis. *Phys. Rev. C*, 83:064605, Jun 2011.

[81] M. H. Mahzoon, R. J. Charity, W. H. Dickhoff, H. Dussan, and S. J. Waldecker. Forging the link between nuclear reactions and nuclear structure. *Phys. Rev. Lett.*, 112:162503, Apr 2014.

[82] M. H. Mahzoon, M. C. Atkinson, R. J. Charity, and W. H. Dickhoff. Neutron skin thickness of ^{48}Ca from a nonlocal dispersive optical-model analysis. *Phys. Rev. Lett.*, 119:222503, Nov 2017.

[83] A. Strazzeri. On the general form of the particle angular correlation following the sequential decay of the heavy reaction product in one-level excitation hypothesis.-(i). double angular correlation. Report CRN-PN-78-15, Center de Recherches Nucléaires, Strasbourg, France, 1978. Also available on the internet from the International Nuclear Information System, Ref. number 10481601.

[84] E. P. Wigner and L. Eisenbud. Higher angular momenta and long range interaction in resonance reactions. *Phys. Rev.*, 72:29–41, Jul 1947.

[85] O.B. Tarasov and D. Bazin. Lise++ : design your own spectrometer. *Nuclear Physics A*, 746:411 – 414, 2004. Proceedings of the Sixth International Conference on Radioactive Nuclear Beams (RNB6).

[86] J. F. Ziegler, J. P. Biersack, and U. Littmark. *The Stopping and Range of Ions in Solids*. Pergamon Press, New York, 1985. The code SRIM can be found at www.srim.org.

[87] Romualdo deSouza. Zepto systems inc. *3110 S Mulberry Ln, Bloomington, IN 47401*.

[88] Jonathan Elson. Pico systems. *543 Lindeman Rd. Kirkwood, MO 63122*.

[89] S. J. Willett, S. K. Korotky, R. L. Phillips, D. A. Bromley, and K. A. Erb. Spin alignment and phase angles in ^{12}C+^{12}C inelastic scattering. *Phys. Rev. C*, 28:1986–2000, Nov 1983.

[90] J. J. Kolata, R. Auble, and A. Galonsky. Excitation energy of the first excited state of ^{12}C, and observation of a coherent doppler effect. *Phys. Rev.*, 162:957–962, Oct 1967.

[91] Andrew E. Stuchbery. γ-ray angular distributions and correlations after projectile-fragmentation reactions. *Nuclear Physics A*, 723(1):69 – 92, 2003.

[92] W. Trombik, W. Trautmann, F. Krug, W. Dünnweber, D. Konnerth, W. Hering, R. Singh, and D. Zeppenfeld. Alignment and resonances in ^{12}C+^{12}C inelastic scattering. *Physics Letters B*, 135(4):271 – 274, 1984.

[93] A. H. Wuosmaa, R. W. Zurmühle, P. H. Kutt, S. F. Pate, S. Saini, M. L. Halbert, and D. C. Hensley. Spin alignment and resonance behavior in the ^{24}Mg+^{24}Mg system. *Phys. Rev. C*, 41:2666–2680, Jun 1990.

[94] N. Kato, K. Anai, T. Tachikawa, H. Fujita, K. Kimura, T. Sugimitsu, and Y. Nakajima. Spin alignment in resonant ^{12}C+^{16}O inelastic scattering. *Physics Letters B*, 120(4):314 – 318, 1983.

[95] D. E. M. Hoff, R. J. Charity, K. W. Brown, C. D. Pruitt, L. G. Sobotka, T. B. Webb, G. Potel, B. Roeder, and A. Saastamoinen. Large longitudinal spin alignment of excited projectiles in intermediate energy inelastic scattering. *Phys. Rev. Lett.*, 119:232501, Dec 2017.

[96] ATLAS Collaboration. Measurement of higgs boson production in the diphoton decay channel in *pp* collisions at center-of-mass energies of 7 and 8 TeV with the ATLAS detector. *Phys. Rev. D*, 90:112015, Dec 2014.

[97] J. Pochodzalla, C. K. Gelbke, W. G. Lynch, M. Maier, D. Ardouin, H. Delagrange, H. Doubre, C. Grégoire, A. Kyanowski, W. Mittig, A. Péghaire, J. Péter, F. Saint-Laurent, B. Zwieglinski, G. Bizard, F. Lefèbvres, B. Tamain, J. Québert, Y. P. Viyogi, W. A. Friedman, and D. H. Boal. Two-particle correlations at small relative momenta for ^{40}Ar induced reactions on ^{197}Au at E/A = 60MeV. *Phys. Rev. C*, 35:1695–1719, May 1987.

[98] A. H. Wuosmaa, S. Bedoor, K. W. Brown, W. W. Buhro, Z. Chajecki, R. J. Charity, W. G. Lynch, J. Manfredi, S. T. Marley, D. G. McNeel, A. S. Newton, D. V. Shetty, R. H. Showalter, L. G. Sobotka, M. B. Tsang, J. R. Winkelbauer, and R. B. Wiringa. Ground-state properties of ^{5}H from the ^{6}He(d,^{3} He)^{5}H reaction. *Phys. Rev. C*, 95:014310, Jan 2017.

[99] C. M. Perey and F. G. Perey. Compilation of phenomenological optical-model parameters 1954-1975. *Atomic Data and Nuclear Data Tables*, 17(1):1 – 101, 1976.

[100] M.-J van Goethem, M.S Wallace, B.E Nett, M.A Famiano, K.R Herner, D.J Oostdyk, M Mocko, W.G Lynch, M.B Tsang, P Schotanus, J Telfer, H.L Clark, A Moroni, R de Souza, and L.G Sobotka. Investigations and corrections of the light output uniformity of CsI(Tl) crystals. *Nuclear Instruments and Methods in Physics Research Section A: Accelerators, Spectrometers, Detectors and Associated Equipment*, 526(3):455 – 476, 2004.

[101] FS Stephens and RS Simon. Coriolis effects in the yrast states. *Nuclear Physics A*, 183(2):257–284, 1972.

[102] K.J. Honkanen, F.A. Dilmanian, D.G. Sarantites, and S.P. Sorensen. Determination of the spin alignment in heavy-ion reactions with the spin spectrometer. *Nuclear Instruments and Methods in Physics Research Section A: Accelerators, Spectrometers, Detectors and Associated Equipment*, 257(2):233 – 243, 1987.

[103] M. L. Halbert, J. R. Beene, D. C. Hensley, K. Honkanen, T. M. Semkow, V. Abenante, D. G. Sarantites, and Z. Li. Angular momentum effects in subbarrier fusion of ^{64}Mo. *Phys. Rev. C*, 40:2558–2575, Dec 1989.

[104] D. G. Sarantites, C. Baktash, N. G. Nicolis, G. Garcia-Bermudez, V. Abenante, J. R. Beene, N. R. Johnson, M. L. Halbert, D. C. Hensley, F. K. McGowan, H. C. Griffin, I. Y. Lee, Z. Majka, M. A. Riley, T. M. Semkow, D. W. Stracener, and A. Virtanen. Nuclear-structure effects in proton evaporation spectra. *Phys. Rev. Lett.*, 64:2129–2132, Apr 1990.

[105] J. L. Barreto, N. G. Nicolis, D. G. Sarantites, R. J. Charity, L. G. Sobotka, D. W. Stracener, D. C. Hensley, J. R. Beene, C. Baktash, M. L. Halbert, and M. Thoennessen. Decay of ^{160}Er* in ^{16}O+^{144}Nd and ^{64}Ni+^{96}Zr fusion reactions. *Phys. Rev. C*, 51:2584–2591, May 1995.

[106] P. Reiter, T. L. Khoo, C. J. Lister, D. Seweryniak, I. Ahmad, M. Alcorta, M. P. Carpenter, J. A. Cizewski, C. N. Davids, G. Gervais, J. P. Greene, W. F. Henning, R. V. F. Janssens, T. Lauritsen, S. Siem, A. A. Sonzogni, D. Sullivan, J. Uusitalo, I. Wiedenhöver, N. Amzal, P. A. Butler, A. J. Chewter, K. Y. Ding, N. Fotiades, J. D. Fox, P. T. Greenlees, R.-D. Herzberg, G. D. Jones, W. Korten, M. Leino, and K. Vetter. Ground-state band and deformation of the $Z = 102$ isotope ^{254}No. *Phys. Rev. Lett.*, 82:509–512, Jan 1999.

[107] PH Regan, AE Stuchbery, and SS Anderssen. Measurement of the g-factor of the yrast 10^{+} state in ^{110}Cd. *Nuclear Physics A*, 591(3):533–547, 1995.

[108] J. Billowes, K. P. Lieb, J. W. Noé, W. F. Piel, S. L. Rolston, G. D. Sprouse, O. C. Kistner, and F. Christancho. Lifetime and g-factor measurements of yrast states in ^{134}Nd and ^{136}Nd. *Phys. Rev. C*, 36:974–985, Sep 1987.

[109] W. Reviol, C. J. Chiara, O. Pechenaya, D. G. Sarantites, P. Fallon, and A. O. Macchiavelli. Spectroscopy of ^{186}Pb and ^{186}Tl via evaporation residue detection. *Phys. Rev. C*, 68:054317, Nov 2003.

[110] H. J. Chantler, E. S. Paul, A. J. Boston, M. P. Carpenter, R. Charity, C. J. Chiara, P. T. W. Choy, C. N. Davids, M. Devlin, A. M. Fletcher, D. B. Fossan, D. G. Jenkins, N. S. Kelsall, T. Koike, D. R. LaFosse, P. J. Nolan, D. G. Sarantites, D. Seweryniak, J. F. Smith, K. Starosta, R. Wadsworth, and A. N. Wilson. Signature inversion in doubly odd ^{124}La. *Phys. Rev. C*, 66:014311, Jul 2002.

[111] D. A. Torres, F. Cristancho, L.-L. Andersson, E. K. Johansson, D. Rudolph, C. Fahlander, J. Ekman, R. du Rietz, C. Andreoiu, M. P. Carpenter, D. Seweryniak, S. Zhu, R. J. Charity, C. J. Chiara, C. Hoel, O. L. Pechenaya, W. Reviol, D. G. Sarantites, L. G. Sobotka, C. Baktash, C.-H. Yu, B. G. Carlsson, and I. Ragnarsson. Deformations and magnetic rotations in the ^{60}Ni nucleus. *Phys. Rev. C*, 78:054318, Nov 2008.

[112] K. Van Bibber, R. Ledoux, S. G. Steadman, F. Videbæk, G. Young, and C. Flaum. Fragment spin orientation following deep-inelastic scattering. *Phys. Rev. Lett.*, 38:334–337, Feb 1977.

[113] A.S. Goldhaber. Statistical models of fragmentation processes. *Physics Letters B*, 53(4):306 – 308, 1974.

[114] Heather Olliver, Thomas Glasmacher, and Andrew E. Stuchbery. Angular distributions of γ rays with intermediate-energy beams. *Phys. Rev. C*, 68:044312, Oct 2003.

[115] ATLAS collaboration et al. Evidence for light-by-light scattering in heavy-ion collisions with the ATLAS detector at the LHC. *Nature Physics*, 13(9):852–858, 2017.

[116] D. P. Balamuth, L. E. Cannell, and R. W. Zurmühle. Use of particle-γ angular correlations to study gross structure in the inelastic scattering of ^{12}C on ^{12}C. *Phys. Rev. C*, 23:2492–2502, Jun 1981.

[117] O. Tanimura and U. Mosel. Comparison of predictions for alignment in inelastic scattering of $^{12}\mathrm{C} + {}^{12}\mathrm{C}$. *Physics Letters B*, 114(1):7 – 10, 1982.

[118] G. R. Satchler. *Nucl. Phys.*, 55:1, 1964.

[119] K. W. Brown, R. J. Charity, J. M. Elson, W. Reviol, L. G. Sobotka, W. W. Buhro, Z. Chajecki, W. G. Lynch, J. Manfredi, R. Shane, R. H. Showalter, M. B. Tsang, D. Weisshaar, J. R. Winkelbauer, S. Bedoor, and A. H. Wuosmaa. Proton-decaying states in light nuclei and the first observation of ^{17}Na. *Phys. Rev. C*, 95:044326, Apr 2017.

[120] Isao Kohno. Elastic and inelastic scattering of ^{14}N and ^{12}C projectiles by ^{12}C and ^{28}Si. *Journal of the Physical Society of Japan*, 38(4):945–953, 1975.

[121] Robert Charity et al. *In preparation*, 2018.

[122] Andrey Surzhykov, Ulrich D. Jentschura, Thomas Stöhlker, Alexandre Gumberidze, and Stephan Fritzsche. Alignment of heavy few-electron ions following excitation by relativistic coulomb collisions. *Phys. Rev. A*, 77:042722, Apr 2008.

[123] N.W. Ashcroft and N.D. Mermin. *Solid State Physics*. Saunders College, Philadelphia, 1976.

[124] M. Buenerd, A. Lounis, J. Chauvin, D. Lebrun, P. Martin, G. Duhamel, J.C. Gondrand, and P. De Saintignon. Elastic and inelastic scattering of carbon ions at intermediate energies. *Nuclear Physics A*, 424(2):313 – 334, 1984.

[125] H. G. Bohlen, X. S. Chen, J. G. Cramer, P. Fröbrich, B. Gebauer, H. Lettau, A. Miczaika, W. von Oertzen, R. Ulrich, and T. Wilpert. Refractive scattering and the nuclear rainbow in the interaction of ^{12,13}C with ^{12}C at 20 MeV/N. *Zeitschrift für Physik A Atoms and Nuclei*, 322(2):241–261, Jun 1985.

[126] A. J. Cole, W. D. M. Rae, M. E. Brandan, A. Dacal, B. G. Harvey, R. Legrain, M. J. Murphy, and R. G. Stokstad. Elastic scattering of ^{12}C + ^{12}C between 121 and 290 MeV. *LBL*, (14550), 1982.

[127] T M Cormier. Resonances in heavy-ion nuclear reactions. *Annual Review of Nuclear and Particle Science*, 32(1):271–306, 1982.

[128] H. Morinaga and T. Yamazaki. *In-beam gamma-ray spectroscopy*. Elsevier North-Holland, Inc.,New York, Jan 1976.

Appendix A

Origin of the Band Gap

Perturbation theory has proved to be one of the most successful techniques for predicting quantum-mechanical phenomenon. In traditional quantum-mechanical perturbation theory, there are problems when handling degenerate energy solutions, as the energy corrections from other degenerate levels diverge. In these cases degenerate perturbation theory must be applied. A great case for seeing degenerate perturbation theory in action is applying it to the nearly-free electron model (NFE) in solids. Handling the problem in this way naturally shows the existence of the band gap, a phenomenon that is of great importance in solid-state physics and is the basis of the semiconductor industry. The presentation below is not a new solution of the band gap problem, but nonetheless arose from independent study, and could be presented as a problem in an upper-level quantum-mechanics course, as it was introduced to the author. The NFE model is discussed in much greater detail by Ashcroft and Mermin [123], where they also derive the band gap in the NFE model utilizing degenerate perturbation theory.

Now consider an electron in a solid with any given lattice structure (ignoring impurities, i.e. deviations from a lattice). We can write the Hamiltonian as,

$$H = E_{latt} + H_{ph} + T_{el} + V_{el-el} + V_{el-latt} + V_{el-ph}. \tag{A.1}$$

At T = 0^o K all phonon terms will drop out, and neglecting the electron-electron interaction we arrive at the Hamiltonian,

$$H = T_{el} + V_{el-latt}, \tag{A.2}$$

where $V_{el-latt}(\mathbf{r} + \mathbf{R}) = V_{el-latt}(\mathbf{r})$, a periodic potential, and $\mathbf{R}$ represents a lattice vector.

This leads to the Schrödinger equation,

$$\begin{aligned} H\left|\psi\right\rangle &= E\left|\psi\right\rangle \\ \frac{\hbar^2\mathbf{k}^2}{2m}\left|\psi\right\rangle + V_{el-latt}\left|\psi\right\rangle &= E\left|\psi\right\rangle. \end{aligned} \tag{A.3}$$

Let's assume that $V_{el-latt}(\mathbf{r})$ is a perturbation (it will be represented by $U(\mathbf{r})$). This assumption, coupled with ignoring electron-electron interactions, is known as the nearly-free electron (NFE) model in solid-state physics. The original Hamiltonian, H_0 is the same as that of the free electron gas, $\hbar^2\mathbf{k}^2/2m$, which has plane wave solutions. Projecting $|\mathbf{k}\rangle$ onto Schrödinger's equation we obtain,

$$\begin{aligned} \langle\mathbf{k}|\frac{\hbar^2\mathbf{k}^2}{2m}\left|\psi\right\rangle + \langle\mathbf{k}|U\left|\psi\right\rangle &= \langle\mathbf{k}|E\left|\psi\right\rangle \\ \frac{\hbar^2\mathbf{k}^2}{2m}\langle\mathbf{k}|\psi\rangle + \sum_{\mathbf{k}'}\langle\mathbf{k}|U\left|\mathbf{k}'\right\rangle\langle\mathbf{k}'|\psi\rangle &= E\langle\mathbf{k}|\psi\rangle \\ \epsilon(\mathbf{k})c_{\mathbf{k}} + \sum_{\mathbf{k}'}\langle\mathbf{k}|U\left|\mathbf{k}'\right\rangle c_{\mathbf{k}'} &= Ec_{\mathbf{k}} \end{aligned} \tag{A.4}$$

where the second to last line we have used the fact that $|\mathbf{k}\rangle$ is a complete basis for the original H_0 solutions. In the last line $c_{\mathbf{k}}$ is the particular plane-wave contribution to the final solution of the wavefunction. Also, the kinetic term is rewritten as $\epsilon(\mathbf{k})$. We now have to

evaluate the matrix elements $\langle \mathbf{k}| U |\mathbf{k}'\rangle$. Before we do this, let us understand the structure of momentum space after restricting ourselves to a lattice.

We define *reciprocal lattice vectors* which are the fourier transform of lattice vectors, $\mathbf{R}$. These exist in momentum space, or the *reciprocal space*, given by RS. The reciprocal lattice space is defined by,

$$\text{RL} = \{\mathbf{G} \in \text{RS} \mid e^{-i\mathbf{G}\cdot\mathbf{R}} = 1\} \tag{A.5}$$

We also define a potential for each $\mathbf{G} \in$ RS,

$$U(\mathbf{G}) = \frac{1}{V_{cell}} \int_{cell} U(\mathbf{r}) e^{-i\mathbf{G}\cdot\mathbf{r}} d^3\mathbf{r} = U(-\mathbf{G}). \tag{A.6}$$

Lemma A.0.1. *If $\mathbf{G} \notin$ RL then $U(\mathbf{G}) = 0$.*

Proof. Consider the definition of $\mathbf{G}$ above. If we shift all vectors, $\mathbf{r}$, by a lattice vector, $\mathbf{R}$, then we should arrive at the same value of the potential since the potential is periodic. Let us assume that $\mathbf{G} \notin$ RL and so $e^{-i\mathbf{G}\cdot\mathbf{R}} \neq 1$. Then we have,

$$\begin{aligned} U(\mathbf{G}) &= \frac{1}{V_{cell}} \int_{cell} U(\mathbf{r}+\mathbf{R}) e^{-i\mathbf{G}\cdot\mathbf{r}} e^{-i\mathbf{G}\cdot\mathbf{R}} d^3\mathbf{r} \\ &= \frac{1}{V_{cell}} \int_{cell} U(\mathbf{r}) e^{-i\mathbf{G}\cdot\mathbf{r}} e^{-i\mathbf{G}\cdot\mathbf{R}} d^3\mathbf{r} \\ &= e^{-i\mathbf{G}\cdot\mathbf{R}} U(\mathbf{G}) \Rightarrow U(\mathbf{G}) = 0 \end{aligned}$$

□

Let's replace the sum over $\mathbf{k}'$ in Eq. (A.4) by a sum over all $\mathbf{G} \in$ RS. The resulting equation is then,

$$\epsilon(\mathbf{k}) c_{\mathbf{k}} + \sum_{\mathbf{G}\in\text{RS}} \langle \mathbf{k}| U |\mathbf{k}-\mathbf{G}\rangle \, c_{\mathbf{k}-\mathbf{G}} = E c_{\mathbf{k}}. \tag{A.7}$$

Expanding $\langle \mathbf{k}| U |\mathbf{k}-\mathbf{G}\rangle$ in the $|\mathbf{r}\rangle$ basis over a unit cell we have (by completeness),

$$\begin{aligned}
\langle \mathbf{k}| U |\mathbf{k}-\mathbf{G}\rangle &= \int_{cell} \langle \mathbf{k}| U |\mathbf{r}\rangle \langle \mathbf{r} \mid \mathbf{k}-\mathbf{G}\rangle \, d^3\mathbf{r} \\
&= \int_{cell} U(\mathbf{r}) \langle \mathbf{k} \mid \mathbf{r}\rangle \langle \mathbf{r} \mid \mathbf{k}-\mathbf{G}\rangle \, d^3\mathbf{r} \\
&= \frac{1}{V_{cell}} \int_{cell} U(\mathbf{r}) e^{-i\mathbf{k}\cdot\mathbf{r}} e^{i(\mathbf{k}-\mathbf{G})\cdot\mathbf{r}} d^3\mathbf{r} \\
&= \frac{1}{V_{cell}} \int_{cell} U(\mathbf{r}) e^{-i\mathbf{G}\cdot\mathbf{r}} d^3\mathbf{r} \\
&= U(\mathbf{G}).
\end{aligned} \tag{A.8}$$

The results of **Lemma 0.1** imply that only $\mathbf{G} \in \mathrm{RL}$ will contribute. Thus we can rewrite the $|\mathbf{k}\rangle$ projected Schrödinger equation, (A.7), as,

$$\epsilon(\mathbf{k}) c_{\mathbf{k}} + \sum_{\mathbf{G}\in \mathrm{RL}} U(\mathbf{G}) c_{\mathbf{k}-\mathbf{G}} = E c_{\mathbf{k}}. \tag{A.9}$$

Separating out the $\mathbf{G} = 0$ term we have,

$$\epsilon(\mathbf{k}) c_{\mathbf{k}} + U(\mathbf{G}=0) c_{\mathbf{k}} + \sum_{\mathbf{G}\in \mathrm{RL}/\{0\}} U(\mathbf{G}) c_{\mathbf{k}-\mathbf{G}} = E c_{\mathbf{k}}. \tag{A.10}$$

But we note that,

$$U(\mathbf{G}=0) = \frac{1}{V_{cell}} \int_{cell} U(\mathbf{r}) d^3\mathbf{r}, \tag{A.11}$$

is the same $\forall \mathbf{G} \in \mathrm{RS}$. This term is added to $\epsilon(\mathbf{k})$ and the sum is denoted by $\tilde{\epsilon}(\mathbf{k})$. It should also be noted that this term is precisely the first order energy correction from perturbation theory.

By non-degenerate perturbation theory, the second order correction to the energy, $\Delta^{(2)}$, with a perturbation U is,

$$\Delta^{(2)}_{\mathbf{k}} = \Delta^{(1)}_{\mathbf{k}} + \sum_{G\in \mathrm{RL}/\{0\}} \frac{U(\mathbf{G})^2}{\epsilon(\mathbf{k}-\mathbf{G}) - \epsilon(\mathbf{k})}. \tag{A.12}$$

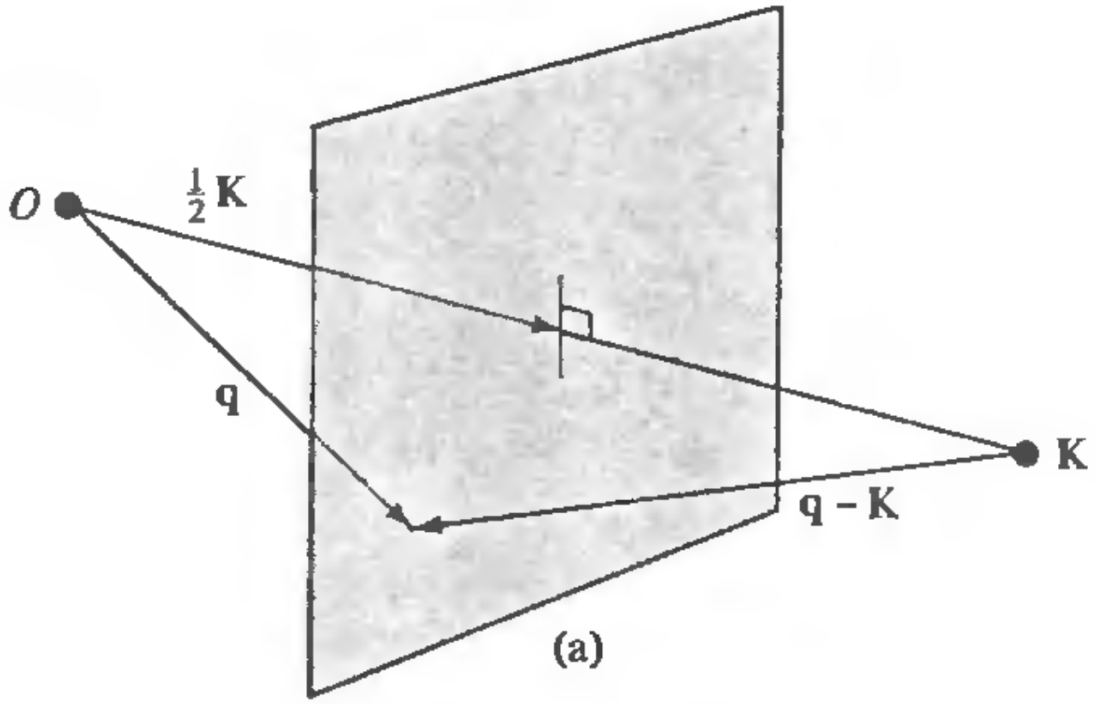

Figure A.1: Figure 9.2(a) from [123], which shows the degenerate energy solutions $|\mathbf{q}|$ and $|\mathbf{q}-\mathbf{K}|$, which lie in the Bragg plane defined by $\mathbf{K} \in \text{RL}$.

This equation would apply for $\mathbf{k}-\mathbf{G}$ such that $|\mathbf{k}-\mathbf{G}|$ is much different than $|\mathbf{k}|$ but there are some $\mathbf{k}-\mathbf{G}$ where this will not be the case; those that lie of the Bragg plane shown in Fig. A.1. For these problem $\mathbf{k}-\mathbf{G}$, succintly $|\mathbf{k}| \cong |\mathbf{k}-\mathbf{G}|$, we have to re-diagonalize the Hamiltonian. As Gottfried says on degenerate perturbation theory,

> *"One must first diagonalize H exactly in each of the degenerate subspaces, and use perturbation theory only to evaluate the effect of distance levels on the level in question." —Quantum Mechanics: Volume 1 (1989), pg. 363*

The first Brillouin zone (FBZ) is defined as,

$$FBZ = \{\mathbf{q} \in RS \mid |\mathbf{q}| < |\mathbf{q}-\mathbf{G}|, \forall \mathbf{G} \neq 0\} \tag{A.13}$$

A consequence of this definition is that $\forall \mathbf{q} \in \mathrm{RS}, \exists \mathbf{k} \in FBZ$ and $\exists \mathbf{G} \in RL$ such that $\mathbf{q} = \mathbf{k} + \mathbf{G}$. Now consider some point $\mathbf{q} \in \mathrm{RS}$, where the corresponding $\mathbf{G} \in \mathrm{RL}$ and $\mathbf{k} \in FBZ$ satisfy $|\mathbf{k}| \cong |\mathbf{k} - \mathbf{G}|$. Separating out the contributions from $\mathbf{k} - \mathbf{G}$ and $\mathbf{k}$ we can write a system of linear equations,

$$\begin{aligned} c_{\mathbf{k}}\tilde{\epsilon}(\mathbf{k}) + U(\mathbf{G})c_{\mathbf{k}-\mathbf{G}} + \sum_{\mathbf{G}' \in \mathrm{RL}/\{0\}} U(\mathbf{G}')c_{\mathbf{k}-\mathbf{G}'} &= Ec_{\mathbf{k}} \\ U(-\mathbf{G})c_{\mathbf{k}} + c_{\mathbf{k}-\mathbf{G}}\tilde{\epsilon}(\mathbf{k}-\mathbf{G}) + \sum_{\mathbf{G}' \in \mathrm{RL}/\{0\}} U(\mathbf{G}')c_{(\mathbf{k}-\mathbf{G})-\mathbf{G}'} &= Ec_{\mathbf{k}-\mathbf{G}}. \end{aligned} \tag{A.14}$$

In re-diagonalizing this problem part of the Hamiltonian we re-solve for the eigenvalues (remembering $U(-\mathbf{G}) = U(\mathbf{G})$),

$$\begin{vmatrix} E - \tilde{\epsilon}(\mathbf{k}) & U(\mathbf{G}) \\ U(\mathbf{G}) & E - \tilde{\epsilon}(\mathbf{k}-\mathbf{G}) \end{vmatrix} = 0 \tag{A.15}$$

Solving the resulting quadratic equation we get two solutions for the energy,

$$E_{\pm} = \frac{[\tilde{\epsilon}(\mathbf{k}) + \tilde{\epsilon}(\mathbf{k}-\mathbf{G})] \pm \sqrt{[\tilde{\epsilon}(\mathbf{k}) + \tilde{\epsilon}(\mathbf{k}-\mathbf{G})]^2 - 4[\tilde{\epsilon}(\mathbf{k})\tilde{\epsilon}(\mathbf{k}-\mathbf{G}) - U(\mathbf{G})^2]}}{2}. \tag{A.16}$$

In the special case that $\mathbf{k}$ lies on the Bragg plane, so $|\mathbf{k}| = |\mathbf{k} - \mathbf{G}|$, we arrive at the solution,

$$E_{\pm} = \tilde{\epsilon}(\mathbf{k}) \pm U(\mathbf{G}) \tag{A.17}$$

which is the band gap!

This formulation suggests the band gap is a topological quantum phenomenom that is a consequence of the electron being confined to a lattice.

Appendix B

Accepted Proposal for ATLAS

Reaction Mechanism for Large Longitudinal Spin Alignment

B.1 Motivation and Background

A reaction mechanism for generating large longitudinal spin alignment of inelastically scattered projectiles was recently proposed [95]. This mechanism explains the large longitudinal spin alignment exhibited by many different nuclei at intermediate energies, including: ^{6}Li*, ^{7}Be*, ^{7}Li*, and ^{17}Ne* [48, 51, 52]. The alignment mechanism stems from an angular-momentum-excitation-energy mismatch and thus has an implicit beam energy threshold that depends on the excitation energy and spin of the excited state. Above this threshold, a transfer of angular momentum from the reaction orbital angular momentum to the intrinsic spin of the nucleus will not conserve energy if the spin of the excited state is aligned with the orbital angular momentum. Thus the exit-channel reaction plane is forced to tilt, and as a consequence, the excited species tend to have their spin aligned with the beam axis. From semi-classical calculations, this threshold is around E/A = 5 MeV for the ^{12}C+^{12}C system.

By measuring the excitation function of spin alignment, this reaction mechanism can be tested further. We propose such a measurement using GAMMASPHERE coupled with a PID-capable charged-particle detector for measuring inelastically scattered ^{12}C*. This alignment mechanism could have future applications, such as measuring g-factors. In fact it may be the cause of large alignments already utilized for measuring g-factors at intermediate energies [1]. Thus it is important to establish the regime of bombarding energy over which this mechanism operates.

The ^{12}C + ^{12}C system is one of the most studied systems at low to intermediate energies. A summary of previous studies showing the relevant measured quantities is provided in Table B.1. Many of these studies measure the differential cross sections for elastic scattering and inelastic excitation to the $J^{\pi} = 2^{+}$ [4.4 MeV] state [124, 125, 126, 120]. Some are extremely comprehensive but still did not measure the spin alignment of ^{12}C* [127]. The few experiments that have measured the γ-ray angular distributions (required for extraction of magnetic-substate populations), were performed at low energies ($< E/A = 5.5$ MeV) [92, 89, 116]. These low-energy measurements of ^{12}C* spin alignment were consistent with a reduction in magnitude of the reaction angular momentum in order to compensate for the increase in spin of the system [117, 89]. These measurements were performed below our expected threshold for large alignment, and at higher beam energies ^{12}C* should switch over to large longitudinal spin alignment. These alignment studies also suggest that the scattering at specific resonance energies is dominated by one partial wave. If this were true, then large oscillations in alignment with scattering angle are expected due to the high-order spherical harmonic in the wavefunction. At higher energies, above the resonance region, there should be interference of partial waves resulting in a rather smooth function of alignment with scattering angle [95], which makes the alignment more suitable for g-factor measurements.

The previous studies of ^{12}C* spin alignment were focused on correlating gross structures of spin alignment with intermediate structures in the excitation function of the reaction cross section. None of the studies used a device comparable to GAMMASPHERE to determine

Table B.1: Experiments measuring properties of the $^{12}C + ^{12}C$ system at a range of beam energies and the relevant data measured.

Beam Energy [MeV/A]	$d\sigma_{elas}/d\Omega$	$d\sigma_{inel}/d\Omega$	Spin Alignment	Ref.
2.7-5.5	Yes	Yes	No	[127]
2.7-5.5	No	No	Yes	[92]
2.7-5.5	No	Yes	Yes	[89]
5.8	Yes	Yes	No	[120]
10-24	Yes	Yes	No	[126]
20	Yes	Yes	No	[125]
30	Yes	Yes	No	[124]
86	Yes	Yes	No	[124]

the magnetic-substate populations. These studies also restricted their measurements to scattering angles $> \theta_{c.m.} = 30^o$. The magnetic substate populations produced at a given scattering angle need to be weighted by the differential cross section for the process if a gross structure of the alignment is to be observed i.e. the alignment should be angle-averaged and weighted by the differential cross section. This was taken into account in one study [92]. The restriction of the measurements to larger scattering angles means a large portion of the reaction yield was missed, and in turn, the amount of alignment measured is a small portion of the actual alignment generated. We intend to measure the spin alignment of $^{12}C^*$ over many scattering angles, starting near the grazing angle of the reaction, allowing us to better understand the generation of spin alignment. We also want to extend the study of the spin alignment for $^{12}C^*$ to intermediate energies.

B.2 Objective and Beamtime Request

To effectively probe the proposed alignment mechanism for the 1st excited state of ^{12}C we need to measure γ-ray angular distributions at an energy near and above the beam-energy threshold for longitudinal spin alignment. The previous experiments measuring spin alignment suggest this threshold is around $E/A = 4$ MeV, however, because of the large variations in the cross section for this regime we want to perform our measurements above

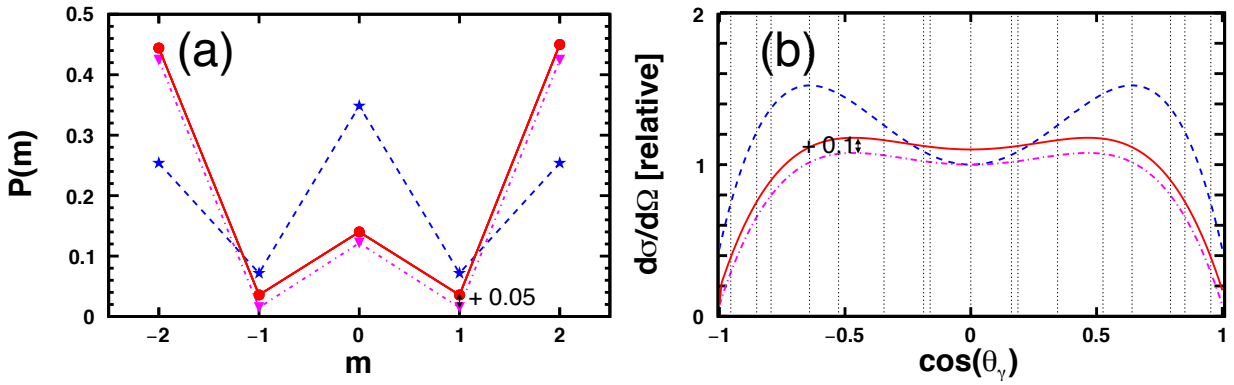

Figure B.1: (a) DWBA predictions (using a soft rotator model) of the magnetic substate distributions of ^{12}C(^{12}C,^{12}C)^{12}C* [4.4 MeV] inelastic scattering at E/A = 6, 12, & 17 MeV (blue dashed line, purple dot-dashed line, and red solid line) at their grazing angles of $\theta_{\rm c.m.} = 13.7^o, 6.5^o$, and 4.5^o, respectively. We have taken into account a $\pm 2^o$ resolution in center-of-mass angle. (b) The resulting γ-ray angular correlations for the three energies using the magnetic-substate populations in (a). We have used the beam-axis as the quantization-axis, and assume the transition is a pure E2. The dotted vertical lines show the detector positions of GAMMASPHERE in the laboratory frame. For comparison, the magnetic-substate populations and resulting angular distributions have been shifted for $E/A = 17$ MeV.

the resonance region. To get a coarse excitation function of spin alignment, we propose using E/A = 6, 12, & 17 MeV ^{12}C beams provided by ATLAS.

DWBA calculations employing a breakup model are consistent with the proposed alignment mechanism and largely reproduce the previously observed spin alignments. Large longitudinal spin alignments are also predicted by DWBA calculations using a soft-rotator model (which introduces a deformation parameter into the spherical optical potentials), and so this mechanism should be active for ^{12}C(^{12}C,^{12}C)^{12}C*[4.4 MeV] [52]. The predicted magnetic-substate distributions from the soft-rotator model (at the grazing angles) are shown in Fig. B.1(a) for beam energies of E/A = 6, 12, & 17 MeV (dashed blue line, dot-dash purple line, and solid red line, respectively). These calculations have included a resolution of $\pm 2^o$ in the center-of-mass frame, and use optical-potential parameters from the literature [120].

Measuring spin alignment for particle-bound states can be done by analyzing the angular distribution of the emitted γ rays [128]. We intend to measure these distributions with GAMMASPHERE enabled by its angular coverage at 17 laboratory angles. The deduced

angular distributions of γ rays from the predicted magnetic-substate populations are shown in Fig. B.1(b). To detect the inelastically scattered ^{12}C* [4.4 MeV] at the higher energies, we plan to use a Si-Si telescope. At the lowest energy, we will use a single-element Si detector backed by a fast-plastic detector (used as an α veto). These detectors will be mounted in the MICROBALL chamber. The particle identification of ^{12}C will allow us to exclude α events produced in the reaction ^{12}C(^{12}C,^{16}O*)^{8}Be, which will be in coincidence with some γ rays of $E_\gamma \geq 6.13$ MeV from ^{16}O* ($3^- \rightarrow 0^+$, $2^+ \rightarrow 0^+$). The charged-particle detector position will be remotely movable i.e. we will be able to change angles from outside the vault. Because the system of interest is composed of identical particles, the center-of-mass scattering angle of the target and projectile will be the same. Thus we are not required to differentiate whether the target or projectile emitted the γ ray and both should exhibit large longitudinal alignment. The ambiguity between projectile and target emission will need to be considered in a DWBA analysis.

For performing a proper DWBA optical model analysis it is necessary to have consistent phenomenological optical potentials. This requires fitting the parameters of the optical potentials with data of the elastic and inelastic differential cross sections. The energies of our coarse excitation function are chosen because the differential elastic and inelastic cross sections have been measured [ref. [120] for $E/A = 6$ MeV and ref. [126] for $E/A = 12$, & 17 MeV].

The overall spin alignment of a nucleus can be represented by the scalar,

$$A = \sum_m \frac{3m^2 - J(J+1)}{J(2J-1)} P(m), \tag{B.1}$$

where $P(m)$ is the normalized population of the m substate. A value of $A = 1$ corresponds to maximal alignment along the quantization axis, while $A = -1$ corresponds to maximal alignment transverse to the quantization axis. The level of alignment produced by single inelastic excitation can vary quite drastically with angle and beam energy (shown in Fig. 2), so it is essential to measure the spin alignment at many scattering angles to compare with

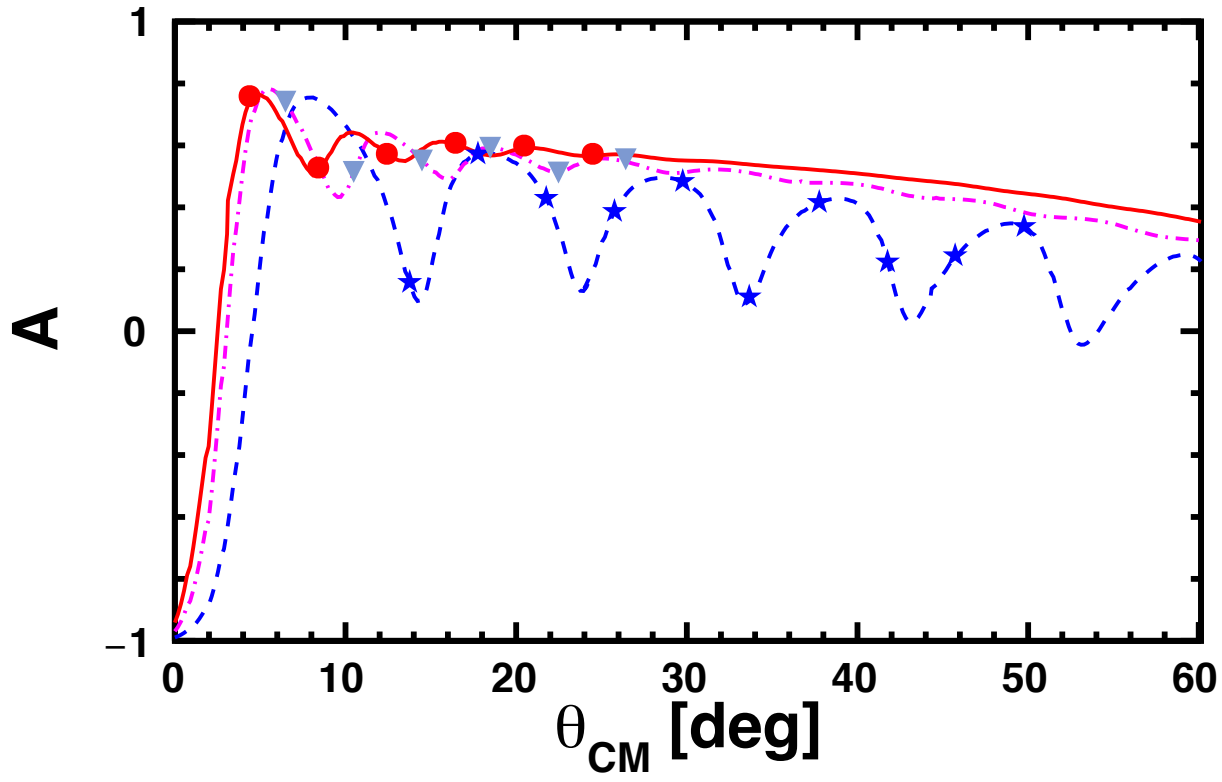

Figure B.2: Predicted alignment as a function of scattering angle for E/A = 6, 12, & 17 MeV (dashed blue line, dash-dot purple line, and solid red line, respectively) taking into account a $\pm 2^o$ resolution in the center-of-mass frame. The blue stars, purple triangles, and red circles indicate the proposed measurements.

the DWBA optical model analysis.

We will measure 6 scattering angles at each of the higher beam energies, E/A = 12 & 17 MeV, and 10 scattering angles at E/A =6 MeV. We will start our measurements at the grazing angle of the reaction and go in 2^o steps (in the laboratory frame) to larger scattering angles. For the higher energies, E/A = 12 & 17 MeV, this corresponds to measurements in the angular range $4^o < \theta_{\rm c.m.} < 26^o$, and at E/A = 6 MeV, $14^o < \theta_{\rm c.m.} < 52^o$. The data points we intend to measure are shown as the red circles, purple triangles, and blue stars in Fig. 2.

At beam energies of E/A = 12 & 17 MeV, a differential cross section of 4-370 mb/sr has been measured for the reaction ^{12}C(^{12}C,^{12}C)^{12}C*[4.4 MeV] in the angular range $8^o < \theta_{\rm c.m.} <$

30^o [126]. Our telescope/detector will subtend an area of about 0.126 cm^2 (4-mm diameter) and will be placed about 15 cm from the target position. This gives us an scattering-angle resolution of 1.5^o in the laboratory frame. For the high-energy beams, we will use a 9 mg/cm^2 thick ^{12}C target. At these high beam energies and small scattering angles, we will use beams with currents of 5 pnA, and so we expect 130,000 single excitation events per hour of beam time. Assuming a 5% photo-peak efficiency for a 4.4 MeV γ ray detected by GAMMASPHERE, we expect 6700 particle-γ coincidences ($\sim$ 400 events per laboratory angle of GAMMAPSHERE) per hour of beam time. For measurements at larger scattering angles we will increase the beam current up to 500 pnA to compensate for the decrease in cross section.

A differential cross section of 10-100 mb/sr has been measured for the reaction of interest in the angular range $18^o < \theta_{\text{c.m.}} < 44^o$ near $E/A = 6$ MeV [120]. With this low energy beam we will use a 1 mg/cm^2 ^{12}C target. Using a beam current of 200 pnA, at small angles we expect 470 particle-γ coincidences at each GAMMASPHERE angle per hour of beam time. At the larger scattering angles we will increase the beam current up to 500 pnA to compensate for the decrease in cross section, giving us $\sim$ 120 particle-γ coincidences at each GAMMASPHERE angle per hour of beam time for the largest scattering angle measurement. The changes in beam rate will be made possible by ATLAS, which can provide over 1000 pnA at beam energies up to $E/A = 20$ MeV.

With these considerations, for the high beam energies we will require $\sim$ 3 hours of beam time at each scattering angle to obtain good statistics ($\sim$ 1000 counts per GAMMASPHERE angle). At the lower beam energy, the measurements at the first 5 scattering angles will take $\sim$ 2-3 hours of beam time per scattering angle. The last 5 scattering angles will require $\sim$ 5-10 hours of beam time per scattering angle. Overall, we require at least 99 hours of beam time (36 hours for the higher beam energies and 63 hours for the lower beam energy). Including some time to debug the apparatus, we request 5 days of beam time.

Physical Constants

fermi (fm)	$1 \cdot 10^{-15}$(m)
barn (b)	100 (fm^2) = 10^{-24} (cm^2)
eV	1.6022·10^{-19} (Joules)
Planck's Constant ($\hbar$)	6.582 ·10^{-22} (MeV·s)
Speed of Light (c)	2.99792458·10^8 (m/s) $\approx$ 29.98 (cm/ns)
$\hbar c$	197.3 (MeV·fm)
Elementary Charge (e)	1.60217662·10^{-19} (Coulombs)
Coulomb's Constant (k_e)	1.44 (MeV·fm/e^2)
amu (u)	931.494 (MeV/c^2)
Neutron Mass (m_n)	939.565 (MeV/c^2) = 1.0087u
Proton Mass (m_p)	938.272 (MeV/c^2) = 1.0073u
Electron Mass (m_e)	0.5110 (MeV/c^2) = 5.486·$10^{-4}u$
Nuclear Magneton (μ_N)	$\frac{e\hbar}{2m_p}$ = 3.1524512550(15)·10^{-8} (eV·Tesla^{-1})
Proton Mangetic Moment (μ_p)	2.792847 μ_N
Neutron Magnetic Moment (μ_n)	-1.913042 μ_N

Glossary

ADC **A**nalog-to-**D**igital **C**onverter. Historically The ADCs sat in the acquisition crate but most modern systems place them closer to the front-end signal processing electronics. For example, The HINP-16c systems employ ADCs on the CBs. 73

ATLAS **A**rgonne **T**andem **L**inear **A**ccelerator **S**ysyem, a facility at Argonne national laboratory for providing up to $E/A = 20$ MeV ion beams. Although the name has Tandem in it this kind of accelerator is no longer included in the system. Confusingly, there is a detector array with the same name at CERN on the border of Switzerland and France, that is involved in Large Hadron Collider experiments. For example, the discovery of the Higgs boson was made by analyzing ATLAS detector data. v, 38, 123, 147, 149–151, 153

β-NMR NMR done on β unstable nuclei. Such experiments are done to determine g-factors for unstable nuclei by utilizing the non-parity conservation of the weak force. 16

CAMAC **C**omputer **A**ided **M**easurement **A**nd **C**ontrol units, which are used for data acquisition in nuclear and high-energy physics. 73

CB **C**hip **B**oard. CBs have two HINP-16c ASICs, i.e. 32-channels of signal processing electronics. 73

CFD **C**onstant-**F**raction **D**iscriminator. A device that takes a linear input and produces a logical timing output independent of the amplitude of the input. It accomplishes this by finding the zero-crossing point of a waveform constructed from adding delayed and attenuated versions of the original input. Operation requires both a delay and an enabling threshold for a leading-edge discriminator (LED). CFD can be implemented in analog or digital electronics. Using a LED along is a simpler, faster and less expensive way to produce a logical timing signal however the time of its output depends on the amplitude of the input signal. A (software) "walk" correction can be applied to a LED to make the time amplitude independent if the pulse-height is available and if it is tolerable to make the correction, either in firmware or software, later in real time. 73

Clebsch-Gordan coefficents These coefficients are derived from angular-momentum coupling, allowing one to change between uncoupled and coupled angular momentum bases. xiii, 109, 110, 113, 119, 125

CSA **C**harge-**S**ensitive **A**mplifier. They exist in all signal processing lines and are generally the resolution determining component. 73

direct reactions Encompossases many nuclear processes that occur in peripheral collisions, including transfer, knockout, stripping, and inelastic reactions. 20, 38, 48, 53

DOM **D**ispersive **O**ptical **M**odel, which uses dispersive corrections to consolidate nuclear structure and reactions. 24, 30, 50, 51

DWBA **D**istorted **W**ave **B**orn **A**pproximation: A method for calculating scattering transition amplitudes to describe nuclear reactions, as well as other quantum-mechanical scattering phenomena. xv, xx, 48, 52, 86, 103, 107, 150–152

FRESCO A fortran-95 program for doing coupled channels DWBA calculations developed by Ian Thompson. Can be downloaded at http://www.fresco.org.uk/. 48, 52, 86

FRIB **F**acility for **R**are **I**sotope **B**eams, which is currently under construction at Michigan State University and will be used to access nuclei far from the valley of stability. 4

***g*-factor** The ratio of the magnetic moment to the intrinsic angular momentum (spin). For a classical object of unit charge, $|g| = 1$. Relativity (for a point particle) generates a factor of 2 (Thomas precession). Radiative corrections generate tiny corrections. Large deviations from these expectations indicate he item has a complex internal structure (e.g. p or n). The classical interpretation is that the center of charge is not the same as the center of mass. 1, 2, 8, 11, 15–17, 33, 34, 101, 121, 122, 125, 126

GFMC **G**reen's **F**unction **M**onte **C**arlo: A method for performing quantum-mechanical calculations. This method has been used to predict many of the properties for $A < 12$ nuclei. 14, 30, 34

HINP-16C A signal processing ASIC for Si detectors. The employed version contains one CSA, one CFD, two-shaping amplifies, two peak trackers and one TCC for each of its 16 channels and the logical control for setting control and readout. 60, 73

LDM The **L**iquid **D**rop **M**odel, which treats nuclei as fluid of protons and neutrons. 2

MB A **M**other **B**oard with 16 slots, i.e. 512-channels of signal processing electronics. 73

Micron semiconductor A company based in the United Kingdom that sells semiconductor radiation detectors. Their catalog can be found at http://www.micronsemiconductor.co.uk/. 58, 94

NIM **N**uclear **I**nstrumentation **M**odule, which are used for creating different electronics logic for running experiments. 73

PMT **P**hoto**M**ultiplier **T**ube. The most common type of light transducer used for scintillators. Following a photocathode of low work function. A series of dynodes with

increasing positive voltage convert each cascading electron into several. The high-gain output is both linear and fast, reproducing the time characteristics of the scintillator. The other common type of light transducer is a PD with a solid-state version (SiPM) becoming popular. PMTs however remain the lowest noise and highest gain light transducer. The other transducers are both smaller and magnetic field insensitive. 91

PLF **P**rojectile-**l**ike **f**ragment: The largest fragment resulting from fragmentation reactions. 77, 78, 98–100

TDC **T**ime-to-**D**igital **C**onverter. A module for determing timing from a start and stop signal. Typically a capacitor is charged at a start time until the system receives a stop (called a time to charge converter i.e. a TCC). The charge on the capacitor can then be read out by an ADC. The time between start and stop can be determined from the amount of charge collected by the ADC. 73

telescope Stack of detector elements that allows for extraction of dE/dX and the employment of the Bethe-Bloch stopping power equation for particle identification. ix, 60, 62, 63, 67, 76, 91, 94

***T* matrix** Otherwise known as the transition amplitude, the T matrix is used to describe the the transition from initial to final scattering states. 44, 48, 54, 55, 105

TUNL **T**riangle **U**niversities **N**uclear **L**aboratory, on the campus of Duke University. This facility houses a tandem accelerator. vi, xi, 10, 81

VME **V**ersa **M**odule **E**uropa bus. Modules (e.g. XLM) with this bus structure fit into standard crates that service the bus and supply all necessary voltages. These modules/crates sit between the front-end signal and the computer acquisition. 73